Characteristics of Particulate Emissions from Low Temperature Combustion and Renewable Fuels

Aerosol Mass Spectrometry of Refractory Carbonaceous Particles

Malmborg, Vilhelm

2020

Document Version:
Publisher's PDF, also known as Version of record

Characteristics of Particulate Emissions from Low Temperature Combustion and Renewable Fuels

Aerosol Mass Spectrometry of Refractory Carbonaceous Particles

VILHELM MALMBORG
DEPARTMENT OF DESIGN SCIENCES | LTH | LUND UNIVERSITY

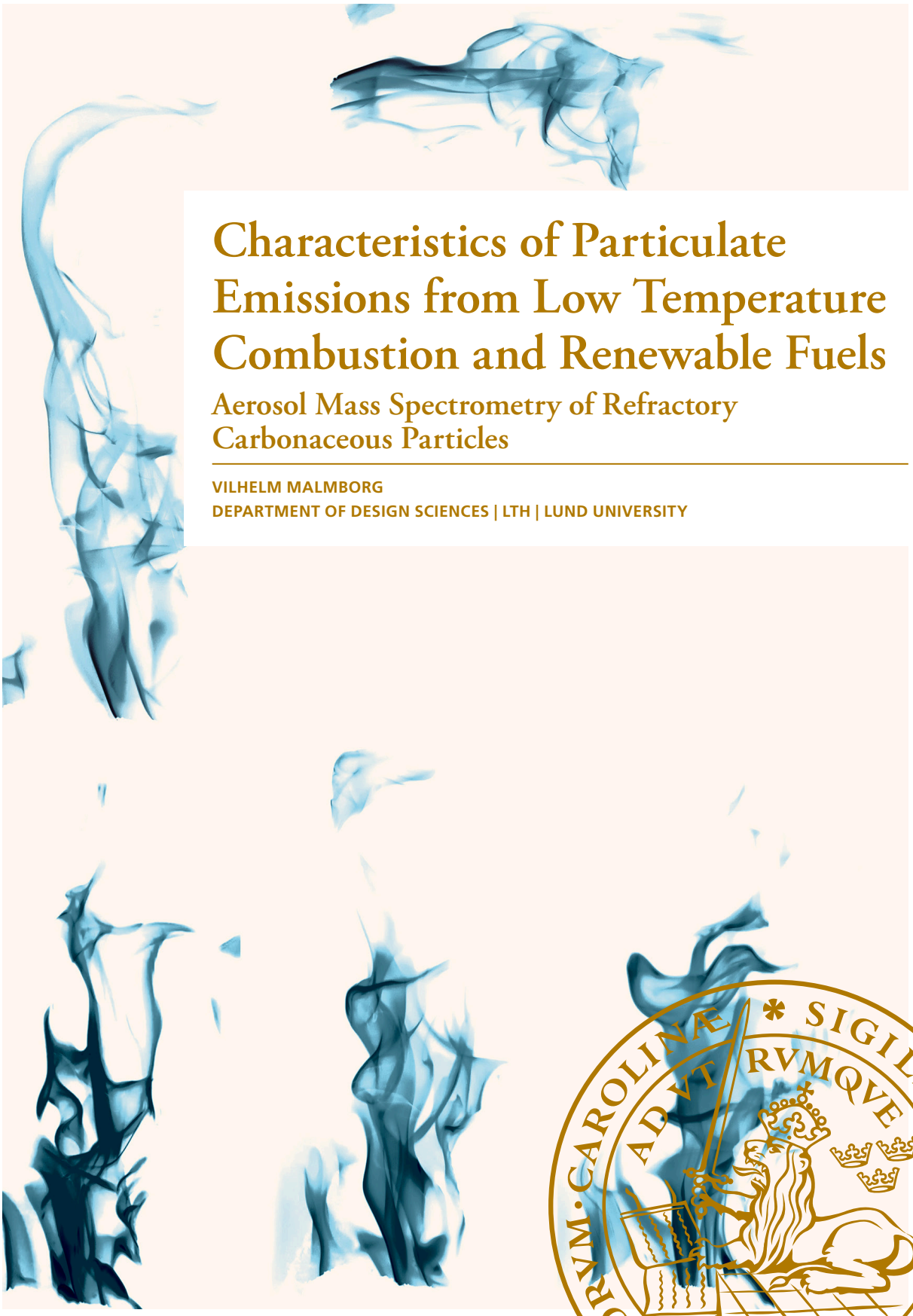

Characteristics of Particulate Emissions from Low Temperature Combustion and Renewable Fuels

Characteristics of Particulate Emissions from Low Temperature Combustion and Renewable Fuels

Aerosol Mass Spectrometry of Refractory Carbonaceous Particles

Vilhelm Malmborg

LUND
UNIVERSITY

DOCTORAL DISSERTATION

by due permission of the Faculty of Engineering, Lund University, Sweden.
To be defended at Stora Hörsalen, IKDC. Date 2020-01-17 and time 09:00.

Faculty opponent
Dr. Amanda Lea-Langton
Department of Mechanical, Aerospace & Civil Engineering,
The University of Manchester

Organization LUND UNIVERSITY	Document name Doctoral Dissertation
Department of Design Sciences Ergonomics and Aerosol Technology	Date of issue 2020-01-17
Author: Vilhelm Malmborg	Sponsoring organization

Characteristics of Particulate Emissions from Low Temperature Combustion and Renewable Fuels
Aerosol Mass Spectrometry of Refractory Carbonaceous Particles

Particulate air pollution is one of the major causes of premature death in the world, and combustion-derived soot emissions contribute strongly to the particulate pollution to which humans are exposed. Black carbon (BC) is one such emission and denotes soot with strong light absorption in the ultraviolet to infrared spectrum. Combustion can also generate brown carbon (BrC) particles, with absorption confined to shorter wavelengths than BC and absorption Ångström exponents (AAEs) significantly higher than 1. When emitted to the atmosphere, BC and BrC can accelerate global warming by absorbing incoming solar radiation. The overall aim of this thesis is to improve the understanding of relationships between combustion conditions, physicochemical soot properties, and parameters which are of relevance for adverse health effects and climate impact.

Soot emissions were studied from a miniCAST soot generator, a heavy-duty diesel engine, and from traditional and modern biomass based cook stoves. The soot particles were characterized for their optical properties, chemical composition, size, and carbon nanostructure (soot maturity). Soot formation and oxidation processes were studied by extracting particles from the cylinder of a heavy-duty diesel engine. The diesel engine was equipped with an exhaust gas recirculation system, and used either Swedish MK1 fossil diesel, a rapeseed methyl ester (RME) biodiesel, or a renewable hydrotreated vegetable oil (HVO) fuel.

Immature soot was characterized by short and amorphous nanostructures, BrC absorption, high polycyclic aromatic hydrocarbon (PAH) fractions, and refractory organic carbon that partially formed pyrolytic carbon during thermal-optical analysis. Mature soot was characterized by ordered nanostructures, BC absorption, low PAH mass fractions, and mass dominated by elemental carbon.

A novel methodology was introduced to investigate differences in soot maturity using a soot particle aerosol mass spectrometer (SP-AMS). Mature soot, characterized by long fringe lengths, generated mainly low molecular weight carbon cluster fragments (C^+_{1-5}). In addition to C^+_{1-5}, immature soot with shorter fringe lengths produced signals from midcarbon and fullerene carbon clusters ($C^+_{\geq 6}$). The new methodology and interpretation can improve methods that use aerosol mass spectrometry for the source apportionment of combustion emissions. It can also aid in the development of new emission mitigation strategies, for example, with respect to the soot oxidation reactivity of relevance for diesel particulate filters.

The results show that low temperature combustion conditions result in soot with immature characteristics, while higher temperatures result in more mature soot. The elevated AAEs and a major fraction of the BrC absorption were assigned to refractory soot components. Specifically, the analysis suggested that the progression from BrC to BC absorption as soot maturity increased was caused primarily by the growth of refractory aromatic units, which are the soot building blocks. This description of how combustion conditions may control soot properties can improve our understanding of processes related to light absorption in the atmosphere.

The renewable HVO and RME fuels reduced particulate matter and BC emissions; the RME, in addition, reduced PAH emissions compared to fossil diesel. The formation of reactive oxygen species (ROS) is an important mechanism in particle-induced toxicity. The ability of soot particles to form ROS increased with increasing combustion temperatures. It was hypothesized from the analysis of soot properties that the diesel soot potential to form ROS with increasing combustion temperature in the first step increased due to more mature soot nanostructures, and in the second step due to increased oxidation and altered surface oxygen functional groups. This hypothesis can form a basis for future evaluations of drivers of soot particle toxicity that are of relevance for global air pollution problems.

Key words: Emissions, Soot, BC, BrC, ROS, SP-AMS, MiniCAST, Diesel Engine, HVO, RME, Cook Stove

Classification system and/or index terms (if any)

Supplementary bibliographical information		Language: English
ISSN and key title: 1650-9773 Publication 64		ISBN 978-91-7895-380-6 978-91-7895-381-3
Recipient's notes	Number of pages:96	Price
	Security classification	

Signature  Date 2019-11-29

Characteristics of Particulate Emissions from Low Temperature Combustion and Renewable Fuels

Aerosol Mass Spectrometry of Refractory Carbonaceous Particles

Vilhelm Malmborg

LUND
UNIVERSITY

Cover by Vilhelm Malmborg

Faculty of Engineering
Department of Design Sciences
Lund University

ISBN 978-91-7895-380-6 (print)
ISBN 978-91-7895-381-3 (pdf)
ISSN 1650-9773 Publication 64

Printed in Sweden by Media-Tryck, Lund University
Lund 2020

Media-Tryck is an environmentally certified and ISO 14001:2015 certified provider of printed material. Read more about our environmental work at www.mediatryck.lu.se

MADE IN SWEDEN

You can't stay in your corner of the Forest waiting for others to come to you.
You have to go to them sometime.

A.A. Milne (or Winnie the Pooh)

Why do experiments?

Observational studies, such as those including long term measurements of properties of ambient air pollution, rely on random fluctuations in the controlling variables in order to draw conclusions on what could cause an observed effect. We do experiments mainly to understand and describe the mechanisms responsible for an observed effect or relation. An experimental study is therefore designed to take control of one or several parameters that are hypothesized to control a phenomenon. Experimental studies are very well suited for hypothesis testing. In some experimental studies, the controlling variables are adjusted to simply observe what the effects are. Such experimental studies are more similar to observational studies and are often hypothesis-generating. These can precede a later study in which the parameters are controlled in a manner that tests a specific hypothesis. Soot processes have been extensively studied but many aspects still remain inconclusive. The experiments conducted and presented in this thesis were often designed to simultaneously test hypotheses and to generate new ones (*Figure below*). I personally enjoyed the book, *Experiment!: Planning, Implementing and Interpreting*, by Prof. Öivind Andersson and I warmly recommend it to the reader who, like me, enjoys experiments and is interested in how we can approach them.

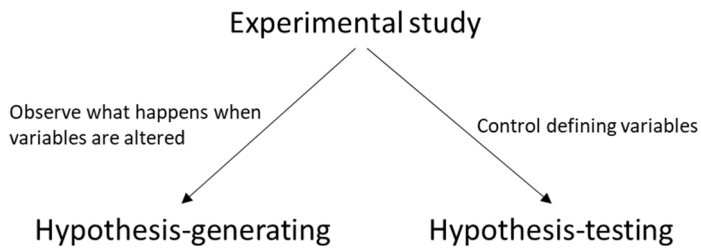

Simplified description of the two main types of study designs used during the thesis research.

Table of Contents

Abstract

Particulate air pollution is one of the major causes of premature death in the world, and combustion-derived soot emissions contribute strongly to the particulate pollution to which humans are exposed. Black carbon (BC) is one such emission and denotes soot with strong light absorption in the ultraviolet to infrared spectrum. Combustion can also generate brown carbon (BrC) particles, with absorption confined to shorter wavelengths than BC and absorption Ångström exponents (AAEs) significantly higher than 1. When emitted to the atmosphere, BC and BrC can accelerate global warming by absorbing incoming solar radiation. The overall aim of this thesis is to improve the understanding of relationships between combustion conditions, physicochemical soot properties, and parameters which are of relevance for adverse health effects and climate impact.

Soot emissions were studied from a miniCAST soot generator, a heavy-duty diesel engine, and from traditional and modern biomass based cook stoves. The soot particles were characterized for their optical properties, chemical composition, size, and carbon nanostructure (soot maturity). Soot formation and oxidation processes were studied by extracting particles from the cylinder of a heavy-duty diesel engine. The diesel engine was equipped with an exhaust gas recirculation system, and used either Swedish MK1 fossil diesel, a rapeseed methyl ester (RME) biodiesel, or a renewable hydrotreated vegetable oil (HVO) fuel.

Immature soot was characterized by short and amorphous nanostructures, BrC absorption, high polycyclic aromatic hydrocarbon (PAH) fractions, and refractory organic carbon that partially formed pyrolytic carbon during thermal-optical analysis. Mature soot was characterized by ordered nanostructures, BC absorption, low PAH mass fractions, and mass dominated by elemental carbon.

A novel methodology was introduced to investigate differences in soot maturity using a soot particle aerosol mass spectrometer (SP-AMS). Mature soot, characterized by long fringe lengths, generated mainly low molecular weight carbon cluster fragments (C_{1-5}^{+}). In addition to C_{1-5}^{+}, immature soot with shorter fringe lengths produced signals from midcarbon and fullerene carbon clusters ($C_{\geq 6}^{+}$). The new methodology and interpretation can improve methods that use aerosol mass spectrometry for the source apportionment of combustion emissions. It can also aid in the development of new emission mitigation strategies, for example, with respect to the soot oxidation reactivity of relevance for diesel particulate filters.

The results show that low temperature combustion conditions result in soot with immature characteristics, while higher temperatures result in more mature soot. The elevated AAEs and a major fraction of the BrC absorption were assigned to refractory soot components. Specifically, the analysis suggested that the progression from BrC to BC absorption as soot maturity increased was caused primarily by the growth of refractory aromatic units, which are the soot building blocks. This description of how combustion conditions may control soot properties can improve our understanding of processes related to light absorption in the atmosphere.

The renewable HVO and RME fuels reduced particulate matter and BC emissions; the RME, in addition, reduced PAH emissions compared to fossil diesel. The formation of reactive oxygen species (ROS) is an important mechanism in particle-induced toxicity. The ability of soot particles to form ROS increased with increasing combustion temperatures. It was hypothesized from the analysis of soot properties that the diesel soot potential to form ROS with increasing combustion temperature in the first step increased due to more mature soot nanostructures, and in the second step due to increased oxidation and altered surface oxygen functional groups. This hypothesis can form a basis for future evaluations of drivers of soot particle toxicity that are of relevance for global air pollution problems.

Populärvetenskaplig sammanfattning

Luftföroreningar och i synnerhet partiklar är starkt bidragande orsaker till bland annat lungsjukdomar, stroke, och hjärt-kärlsjukdomar. I Europa leder luftföroreningar till att ca 800 000 människor dör i förtid varje år. Globalt är siffran betydligt högre och totalt beräknas fler än 6 miljoner människor dö i förtid varje år. Luftföroreningar leder därmed till fler dödsfall än det sammanlagda antalet från AIDS, malaria, tuberkulos, samt alla krig och väpnade konflikter i världen. Luftföroreningar påverkar också barns hälsa i högre grad. Världshälsoorganisationen uppskattar att fler än 600 000 barn under 5 år dör, varje år, till följd av sjukdomar som orsakas eller intensifieras av luftföroreningar.

De höga temperaturerna vid förbränning leder till att små partiklar bildas. En ofullständig förbränning kan därför leda till utsläpp av partiklar. Både globalt och regionalt i Europa står utsläpp från förbränning i olika processer för en stor del av luftföroreningarna. Partiklar som bildas i flammor kallas ofta *sotpartiklar* och är vanligt förekommande i avgaser från t.ex. motorer och vedeldning. Svartkroppsstrålning gör att sotpartiklar lyser när de blir tillräckligt varma, och det är sotpartiklarna som ger flammorna i t.ex. vedspisar och stearinljus deras gulaktiga sken.

Sotpartiklar består till största delen av grundämnet kol. Ibland benämns detta material för ”*elementärt kol*” och påminner om grafit. Även andra giftiga substanser bildas och släpps ut från förbränning, t.ex. cancerframkallande *polycykliska aromatiska kolväten*. När röken kyls ned bildar dessa ämnen ofta ett lager på sotpartiklarnas ytor. Ett flertal studier har indikerat att sotpartiklar kan vara mer toxiska än många andra komponenter som finns i luftföroreningar.

Sotpartiklar har ofta en karakteristisk svart färg och kan i atmosfären absorbera solljus. När ljusabsorberande partiklar släpps ut till atmosfären fångar de upp en del av den inkommande solstrålningen som normalt skulle reflekterats tillbaka till rymden. Detsamma sker när ljusabsorberande partiklar landar på snö och is. Svarta sotpartiklar bidrar kraftigt till den globala uppvärmningen. Ibland bildas bruna sotpartiklar. Till skillnad från svarta sotpartiklar så absorberar de bruna partiklarna relativt sett mer av det blåa solljuset än det röda. De bruna partiklarna bidrar till den globala uppvärmningen men hur stor effekt de har på klimatet är idag mycket osäkert. En grundläggande orsak till osäkerheten är bristande kunskap om partiklarnas sammansättning och deras olika källor.

Denna avhandling baseras på ett antal experimentella studier av sotpartiklar från olika typer av förbränning. Syftet var att bidra till en ökad förståelse för hur olika

förbränningsprocesser påverkar sotpartiklars egenskaper och sammansättning, och hur dessa i sin tur påverkar partiklarnas ljusabsorption och hälsorelevanta egenskaper.

Kväveoxider (NO_x) som bildas vid förbränning under höga temperaturer är starkt förknippade med dieselmotorer. Utan avgasrening är temperaturen i förbränningen den avgörande faktorn för hur stora emissioner av NO_x ett dieselfordon generar. I förbränningsmotorer används tekniker för att sänka temperaturen och därmed minska utsläppen av NO_x. En vanlig sådan teknik är avgasåterföring, så kallad EGR[1]. Hur EGR påverkar utsläpp av sotpartiklar är en tekniskt viktig fråga för avgasrening och för att förstå utsläppen från moderna motorer. I en av studierna extraherades partiklar direkt från motorns cylinder. Koncentrationen av sotpartiklar kunde därmed mätas vid olika tidpunkter i förbränningen. Ökande EGR leder både till mindre sotbildning och sotoxidation inne i motorn. Den minskade oxidationen dominerar över den minskade sotbildningen, varför den sammanvägda effekten trots allt är en ökning av sotemissioner vid högre EGR.

Hur temperaturen i förbränningen påverkar sotpartiklars egenskaper studerades i en dieselmotor samt med en flamsotgenerator som modell. En viktig slutsats från studierna av dessa två mycket olika system är att sotpartiklarnas egenskaper genomgår liknande mognadsprocesser när temperaturen går från låg till hög. Resultaten i avhandlingen visar att sotet *mognar* med ökande temperatur. När sotet mognar förändras den kemiska och fysiska sammansättningen vilket leder till en ökad ljusabsorption och att sotpartiklarna går från att vara bruna till svarta. Detta resultat kan ha betydelse för att förstå vilka typer av förbränning som generar bruna sotpartiklar, vilket i förlängningen kan hjälpa till att öka våra kunskaper om dessa partiklars betydelse för den globala uppvärmningen.

Aerosol masspektrometri är en metod för att bestämma partiklars kemiska sammansättning. Metoden har hög tidsupplösning och stor tillämpningspotential i både omgivningsluft och studier av utsläpp från förbränning. I metoden förångas sotpartiklar med hjälp av en laser. När sotpartiklarna förångas bildas små molekylkluster vilka joniseras och sedan detekteras med hjälp av en *masspektrometer*[2]. Avhandlingsarbetet visar att metoden kan användas för att ge information om sotpartiklarnas mognadsgrad. Metoden kan ge bättre möjligheter att identifiera vilket bidrag olika typer av utsläppskällor har till koncentrationen av sotpartiklar i utomhusluften. Dessutom kan metoden hjälpa till att identifiera vad som kemiskt och fysiskt skiljer de bruna och svarta sotpartiklarna åt.

[1] Engelska, exhaust gas recirculation (EGR)

[2] Masspektrometern detekterar massan hos enskilda atomer eller molekylkluster.

Sotpartiklars hälsorelevanta egenskaper studerades genom att mäta hur mycket reaktiva syreföreningar som sotpartiklar av en bestämd massa bildade. Resultaten visar att de sotpartiklar från dieselmotorn som bildades vid en hög temperatur (lite EGR) genererade nästan 10 gånger mer reaktiva syreföreningar för samma massa jämfört med de sotpartiklar som emitterades vid en låg temperatur (mycket EGR). Utsläppen av sotpartiklar minskade något när fossil diesel byttes mot förnyelsebara HVO och RME bränslen, samtidigt som de uppmätta skillnaderna i sotpartiklarnas egenskaper var små mellan bränslena. Partikelrelaterade klimat- och hälsopåverkande effekter kan därmed vara något lägre för de förnyelsebara bränslena jämfört med diesel.

Papers included in this thesis

Paper 1

Malmborg, V. B.; Eriksson, A. C.; Shen, M.; Nilsson, P.; Gallo, Y.; Waldheim, B.; Martinsson, J.; Andersson, O.; Pagels, J., Evolution of in-cylinder diesel engine soot and emission characteristics investigated with on-line aerosol mass spectrometry. *Environmental Science & Technology* 2017, *51*, 1876-1885. DOI: 10.1021/acs.est.6b03391

Paper 2

Török, S.; Malmborg, V. B.; Simonsson, J.; Eriksson, A.; Martinsson, J.; Mannazhi, M.; Pagels, J.; Bengtsson, P.-E., Investigation of the absorption Ångström exponent and its relation to physicochemical properties for mini-CAST soot. *Aerosol Science and Technology* 2018, *52* (7), 757-767. DOI: 10.1080/02786826.2018.1457767.

Paper 3

Malmborg, V. B.; Eriksson, A. C.; Török, S.; Zhang, Y.; Kling, K.; Martinsson, J.; Fortner, E. C.; Gren, L.; Kook, S.; Onasch, T. B.; Bengtsson, P.-E.; Pagels, J., Relating aerosol mass spectra to composition and nanostructure of soot particles. *Carbon* 2019, *142*, 535-546. DOI: 10.1016/j.carbon.2018.10.072.

Paper 4

Malmborg, V. B.; Eriksson, A. C.; Gren, L.; Török, S.; Shamun S.; Novakovic M.; Zhang, Y.; Kook, S.; Tunér M.; Bengtsson, P.-E.; Pagels, J., Correlation of optical properties with soot nanostructures for variations in combustion temperature. *Manuscript to be submitted.*

Paper 5

Gren, L.; Malmborg, V. B.; Jakobsen N. R.; Shukla P.C.; Shamun S.; Eriksson A. C.; Essig Y.; Krais A. M. K.; Loeschner K.; Strandberg B.; Vogel U.; Tunér M.; Pagels J., Effect of renewable fuels and inlet O_2 concentration on diesel engine emission characteristics and reactive oxygen species (ROS) formation. *Manuscript to be submitted.*

Author's contributions to the papers included in this thesis

Paper 1. I participated in the planning and set-up of the experiment. I carried out a majority of the measurements related to characterizing soot and particle emissions. I was mainly responsible for analyzing the SP-AMS, SMPS, and aethalometer data, and I made major contributions to the interpretation of the data. I also made major contributions to the writing and peer-review process.

Paper 2. I shared the responsibility for carrying out the experiments with the first author. I was mainly responsible for operating the aerosol instruments and analyzing the data from the results. I contributed to the interpretation of results and their presentation in the article. I wrote sections of the article and contributed to the overall writing and peer-review process.

Paper 3. I contributed to the experimental planning. I participated in all experiments, operated most of the aerosol instruments and performed a majority of the data analysis. I evaluated the SP-AMS data in relation to the HRTEM analysis. I made important contributions to the interpretation of results and conclusions. I had a major role in writing and finalizing the article.

Paper 4. I took the initiative to assemble the data from different experiments. I formulated the hypothesis and suggested the choice of methodology to test it. I was responsible for most of the SP-AMS and aethalometer measurements, and performed the data analysis. I made major contributions to the interpretation of the results and formulation of the conclusions. I wrote the majority of the manuscript.

Paper 5. I contributed to the experimental planning. I was responsible for operating the SP-AMS and shared the responsibility of operating several other on-line aerosol instruments with the first author. I processed much of the aerosol and engine time series data, and contributed to the analysis. I assisted in interpreting the results, wrote parts of the manuscript, and contributed with figures.

Peer-reviewed publications not included in this thesis

Martinsson, J.; Eriksson, A. C.; Nielsen, I. E.; Malmborg, V. B.; Ahlberg, E.; Andersen, C.; Lindgren, R.; Nyström, R.; Nordin, E. Z.; Brune, W. H.; Svenningsson, B.; Swietlicki, E.; Boman, C.; Pagels, J. H., Impacts of Combustion Conditions and Photochemical Processing on the Light Absorption of Biomass Combustion Aerosol. *Environmental Science & Technology*, 2015, 49 (24), 14663-14671.

Shen, M.; Malmborg, V.; Gallo, Y.; Waldheim, B. B. O.; Nilsson, P.; Eriksson, A.; Pagels, J.; Andersson, O.; Johansson, B., Analysis of Soot Particles in the Cylinder of a Heavy Duty Diesel Engine with High EGR. *SAE Technical Paper*, 2015. DOI: 10.4271/2015-24-2448

Gallo, Y.; Malmborg, V. B.; Simonsson, J.; Svensson, E.; Shen, M.; Bengtsson, P.-E.; Pagels, J.; Tunér, M.; Garcia, A.; Andersson, Ö., Investigation of late-cycle soot oxidation using laser extinction and in-cylinder gas sampling at varying inlet oxygen concentrations in diesel engines. *Fuel*, 2017. 193, 308-314. DOI:10.1016/j.fuel. 2016.12.013.

Shamun, S.; Novakovic, M.; B. Malmborg, V.; Preger, C.; Shen, M.; E. Messing, M.; Pagels, J.; Tunér, M.; Tunestål, P., Detailed Characterization of Particulate Matter in Alcohol Exhaust Emissions. *The proceedings of the international symposium on diagnostics and modeling of combustion in internal combustion engines, 2017.9, The Japan Society of Mechanical Engineers*, 2017. B304. DOI: 10.1299/jmsesdm.2017.9.B304

Shukla, P. C.; Shamun, S.; Gren, L.; Malmborg, V.; Pagels, J.; Tuner, M., Investigation of Particle Number Emission Characteristics in a Heavy-Duty Compression Ignition Engine Fueled with Hydrotreated Vegetable Oil (HVO). *SAE International Journal of Fuels and Lubricants*, 2018. Vol. 11, pp 495-505. DOI: 10.4271/2018-01-0909

List of abbreviations and acronyms

AAE	absorption Ångström exponent
AMS	aerosol mass spectrometer
ATDC	after top dead center
b_{abs}	absorption coefficient
BC	black carbon
BrC	brown carbon
C_{1-5}^{+}	lowcarbon clusters
$C_{\geq 6}^{+}$	large carbon clusters
C_{3x}^{+}	$C_3^+ / (C_{1-60}^+ - C_3^+)$
CAD	crank angle degrees
EC	elemental carbon
EGR	exhaust gas recirculation
HACA	hydrogen-abstraction-C_2H_2-addition
HRTEM	high-resolution transmission electron microscopy
HULIS	humic-like substances
IMEPg	gross indicated specific mean effective pressure
IR	infrared
MAC	mass absorption coefficient
NO_x	nitrogen oxides
OA	organic aerosol
OC	organic carbon
PAHs	polycyclic aromatic hydrocarbons
PC	pyrolytic carbon
PM2.5	particulate matter with an aerodynamic diameter less than 2.5 µm
ROS	reactive oxygen species
RSR	resonance-stabilized radical
RF	radiative Forcing
SMPS	scanning mobility particle sizer
SP-AMS	soot particle aerosol mass spectrometer
UV	ultraviolet
VOCs	volatile organic compounds
XPS	X-ray photoelectron spectroscopy

1 Introduction

1.1 Air pollution and combustion emissions

Ambient air pollution is detrimental to human health. Epidemiological studies have been essential in establishing relationships between particulate air pollution and health effects. In 1993, a cross-sectional study of six U.S. cities, and on a cohort of more than 8000 adults, showed that the mass concentration of fine particulate matter in ambient air pollution was associated with increased mortality rates, cardiovascular diseases and lung cancer [1]. The most recent global estimates link outdoor and indoor air pollution to more than 6 million premature deaths each year [2, 3], and close to 800 000 in Europe alone [4]. In perspective, air pollution accounts for two thirds of all deaths attributable to pollution in air, water, and soil together, and this is of similar proportion to the number of deaths related to tobacco smoking [3].

Combustion is a primary source of the gaseous and particulate air pollution to which humans are exposed [5, 6]. The complex chemistry and high temperatures involved in common combustion processes result in the generation of toxic gases and particulate matter. Fine particulate matter (PM2.5) is defined as the particulate matter with an aerodynamic diameter less than 2.5 μm. The International Agency for Research on Cancer (IARC) has concluded that there is sufficient epidemiological and toxicological evidence for the classification of outdoor air pollution and its PM2.5 component as carcinogenic to humans [7]. Figure 1 presents estimates of the energy-related anthropogenic contribution to global emissions of primary air pollutants.

Combustion in engines, biomass based heating and cooking, as well as wildfires and prescribed burns account for a majority of the primary fine particulate air pollution to which humans are exposed [3, 5, 6]. Combustion also accounts for nearly all anthropogenic emissions of sulfur dioxide (SO_2) and nitrogen oxides (NO_x), and a majority of the emissions of volatile organic compounds (VOCs) [5]. NO_x is a major component in the generation of tropospheric ozone and in the presence of ammonia, it contributes to the formation of ammonium nitrate particles. Atmospheric processing of SO_2 and VOCs generates sulfuric acid and low-volatility organic compounds that

additionally contribute to PM2.5 through secondary aerosol formation and gas to particle conversion [8].

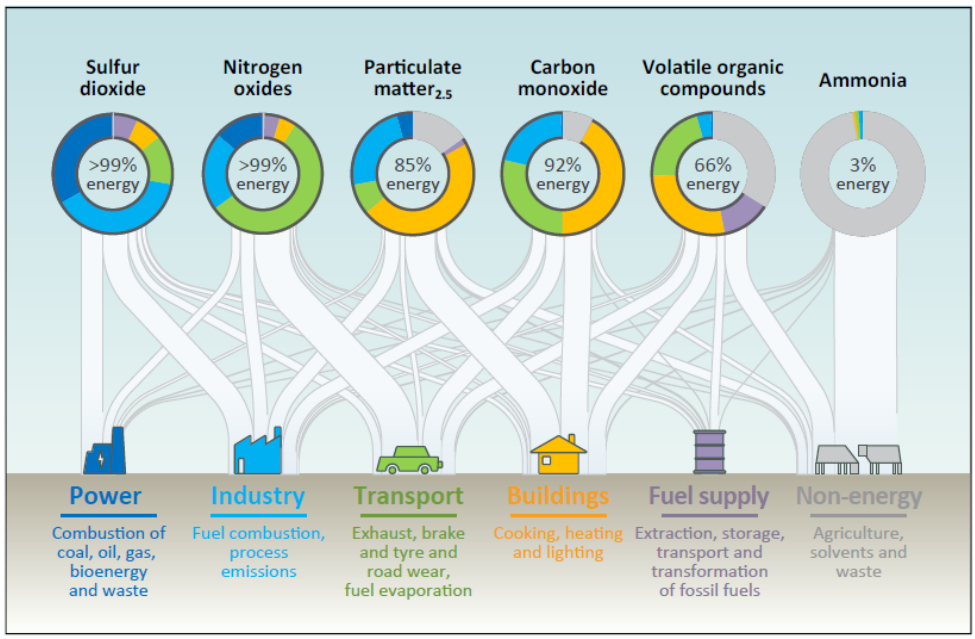

Figure 1. Source: IEA (2016) World Energy Outlook Special Report [5]. All rights reserved. Estimated energy-related contribution to global emissions of primary air pollutants by human-related activities. The global emissions are skewed towards low-income countries. Economical factors and technological advancements result in large regional differences in the sources contributing to primary air pollution. Despite the technological advancements, combustion and energy-related activities remain as major sources to the primary air pollution in the European Union [9].

Soot is the common term denoting the black particulate matter directly emitted from combustion [10]. Soot consists of refractory carbonaceous material formed by pyrolysis gases in hot and fuel-rich regions of flames. In the flame, the refractory material forms small (~10-50 nm) primary particles. Collisions between primary particles rapidly result in the formation of larger soot aggregates (Figure 2).

Refractory carbonaceous soot material has a sublimation temperature of approximately 4000K and is operationally defined as elemental carbon (EC) in thermal-optical carbon analysis. However, the refractory material additionally contains smaller amounts of hydrogen and oxygen [10]. The composition and nanostructure of this refractory carbonaceous material can vary between combustion environments and different fuels. The relationships between combustion conditions and these particle properties are not fully understood, although temperature and premixing can be important parameters [11, 12].

Soot particles typically also contain varying amounts of condensable organic and inorganic material, and ash [13]. Low- and semi-volatile compounds generated in combustion form externally mixed new particles, or condense on to existing surfaces of the refractory carbonaceous material and then form internally mixed particles upon cooling of the exhaust or flue gas. The origin and composition of the inorganic and organic soot components depend on the source and fuel composition. For example the organic aerosol can be both non-refractory and refractory (i.e., a low thermal volatility), and the organic and inorganic (e.g., Zn, Ca, S, P) components can originate from the lubricating oil in engines or potassium from biomass.

The biological response to particulate matter is highly complex, and the mechanisms responsible for the epidemiological observations that associate air pollution with health effects are far from established. The biological response pathways upon inhalation of particulate matter that are established include inflammation, the formation of reactive oxygen species (ROS), and direct DNA damage [14]. Particle properties add to the complexity; additional factors that can influence particle toxicity are size and the shape, solubility, and surface characteristics.

In-vivo studies on the toxicity of combustion emissions have linked both the soluble organic (e.g., PAHs) and insoluble refractory carbonaceous materials to health effects in animal models. These studies have provided detailed descriptions of plausible mechanisms, including ROS formation, involved in the toxicity of particles [15, 16]. However, pathways for ROS formation (e.g., PAHs, metals, refractory soot core) remain unclear, and there is a need for more research towards the identification of specific particle properties and components that contribute to ROS formation.

Combustion emissions stand out in some epidemiological studies that have assessed the toxicity of individual PM2.5 component classes. These show that the relative risk associated with an interquartile range increase of EC is similar to the interquartile range increase of PM2.5. However, if the relative risk is associated with an increase of 1 $\mu g/m^3$, evaluations show that the negative health effects of EC can be almost ten times greater than the effects of other PM2.5 components [17, 18]. Although these studies certainly indicate that EC from combustion can have large negative effects on human health, many co-emitted particle components from combustion are linearly correlated to each other. This may severely obstruct the analysis of effects from a single and independent variable, and large uncertainties still remain with respect to which particle components contribute to health effects.

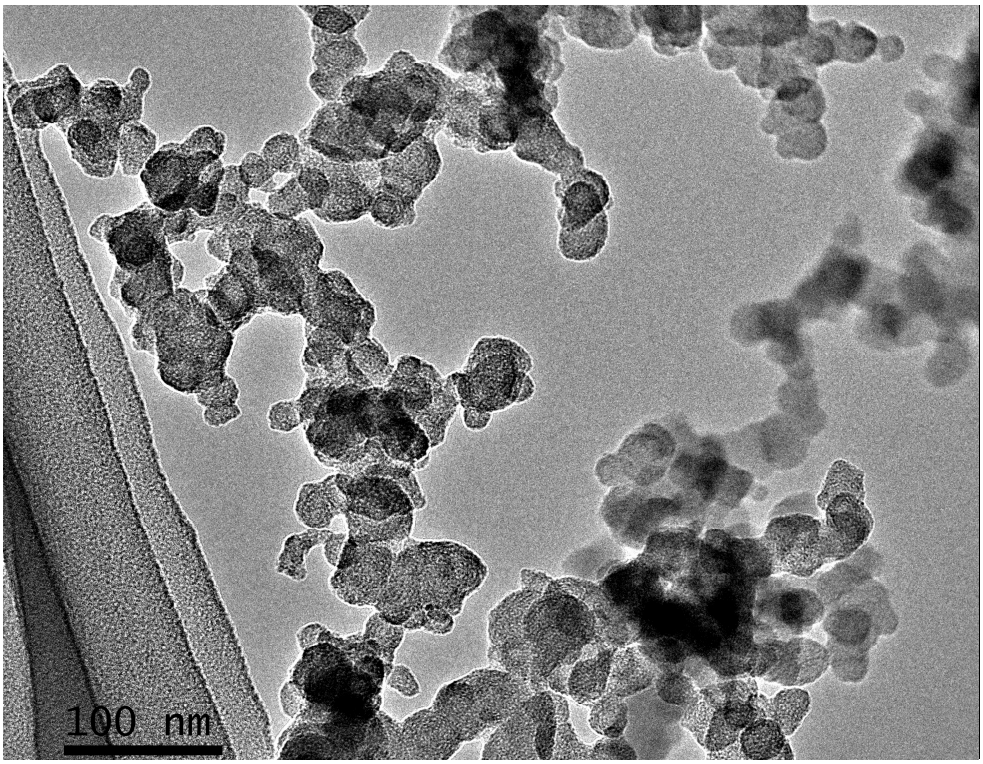

Figure 2. High resolution transmission electron microscopy (HRTEM) image of several large soot aggregates from the miniCAST soot generator. Image courtesy of Louise Gren.

The combustion of fossil-fuels is the main source of anthropogenic CO_2 emissions, and is closely linked to climate change. Renewable fuels can reduce the net-increase of CO_2 in the atmosphere. Hydrotreated vegetable oil (HVO) and rapeseed methyl esters (RME) are two renewable and alternative diesel fuels of relevance for the thesis research.

Figure 3 presents the current estimates of compound-specific radiative forcing, defined as the net energy imbalance between incoming short-wave solar radiation and outgoing long-wave radiation. The radiative forcing due to anthropogenic CO_2 is estimated to be 1.68 [1.33-2.03] W/m^2. Atmospheric aerosol particles directly influence the climate by the direct absorption and scattering of incoming solar radiation, and indirectly by acting as seeds for cloud droplet formation and ice nucleation. Because particulate matter has a comparably short atmospheric lifetime of ~1 week, aerosol particles contribute to short-lived climate forcing [19]. In addition, light-absorbing particles deposited on snow or ice have a warming effect on the climate [19].

Scattering by transparent or weakly absorbing sulfate and organic aerosols is related to a large negative radiative forcing [19]. "Black carbon" (BC) is often used synonymously with "soot" to denote the graphitic-like, carbonaceous material formed in and emitted from flames [20]. BC strongly absorbs radiation in the ultraviolet (UV) to infrared (IR) spectrum [20, 21], and adds to radiative forcing by increasing the (positive) energy imbalance between incoming short-wave radiation and outgoing long-wave radiation [21]. The refractory carbonaceous materials associated with BC have similar absorption properties, with a mean mass absorption coefficient (MAC) value of 7.5 (±1.2) m^2/g at a 550 nm wavelength [20, 21]. Absorption enhancement by "lensing" from the non-absorbing aerosols that coat the refractory BC materials can result in significantly higher (more than a factor of 2) BC absorption and retrieved MAC values [22, 23]. However, such strong lensing enhancement requires very thick coatings, and lensing enhancement may be negligible for ratios of non-BC coating materials to BC lower than 1 [23]. The aerosol particles characterized in the thesis research rarely exceeded a ratio of 1 between the non-refractory coating materials and BC.

In addition to BC, brown carbon (BrC) contributes to the direct radiative forcing. BrC refers to light-absorbing carbonaceous aerosol particles with substantial absorption in the UV to visible spectrum but with limited absorption at longer wavelengths in the near-IR to IR spectrum. BrC can be of either primary or secondary origin. Primary BrC has predominantly been associated with biomass combustion emissions, polycyclic aromatic hydrocarbons (PAHs), and "tar balls". Secondary BrC has been associated with atmospheric gas-phase and particulate-phase processing, and the formation of humic-like substances (HULIS) and nitroaromatics [10, 24, 25]. While BC absorption is connected to highly refractory EC material, BrC absorption is commonly assigned to the organic aerosol. However, BrC may feature both non-refractory and refractory characteristics depending on its source [24, 26, 27]. The MAC value of BrC is less constrained due to the large variability in the chemical components contributing to BrC absorption. Refractory tar balls from biomass burning can have very high MAC values of 3.6-4.1 m^2/g at 550 nm [27]. Secondary BrC materials generally have lower MAC values between 0.02-2 m^2/g at wavelengths in the 300-700 nm interval [24, 28].

Atmospheric BC is associated with a radiative forcing of 0.64 [0.25-1.09] W/m^2 [19]. Yet, the net radiative forcing from scattering and absorption by all aerosol particles is negative (-0.27 [-0.77 to 0.23]). If one takes into account the light absorption from BrC, this results in a significant increase in the overall direct radiative forcing of aerosols [29]. Recent estimates of the radiative forcing of ambient BrC aerosols suggest an additional radiative forcing of ~0.1 W/m^2 [30]. The large confidence interval indicates that the direct radiative forcing due to BC and BrC is not well constrained. The estimates are associated with substantial uncertainties [19, 21], partly due to

uncertainties in assigning BC and BrC MAC values, the absorption wavelength dependence, the atmospheric aging processes and lensing enhancement, along with emission factors (the global BC emission factor in 2000 was estimated to be 7530 [2020-28800] Gg/year [21]).

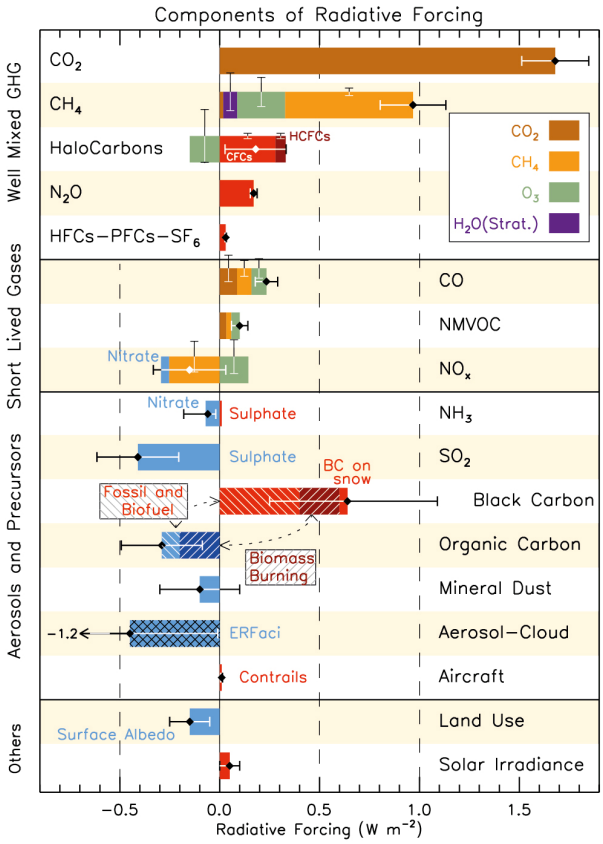

Figure 3. From [19]. Estimated contribution by individual components to the Radiative Forcing (RF). Reprinted with permission from [19].

Original figure text: RF bar chart for the period 1750–2011 based on emitted compounds (gases, aerosols or aerosol precursors) or other changes. Numerical values and their uncertainties are shown in Supplementary Material Tables 8.SM.6 and 8.SM.7. Note that a certain part of CH4 attribution is not straightforward and discussed further in Section 8.3.3. Red (positive RF) and blue (negative forcing) are used for emitted components which affect few forcing agents, whereas for emitted components affecting many compounds several colours are used as indicated in the inset at the upper part the figure. The vertical bars indicate the relative uncertainty of the RF induced by each component. Their length is proportional to the thickness of the bar, that is, the full length is equal to the bar thickness for a ±50% uncertainty. The net impact of the individual contributions is shown by a diamond symbol and its uncertainty (5 to 95% confidence range) is given by the horizontal error bar. ERFaci is ERF due to aerosol–cloud interaction. BC and OC are co-emitted, especially for biomass burning emissions (given as Biomass Burning in the figure) and to a large extent also for fossil and biofuel emissions (given as Fossil and Biofuel in the figure where biofuel refers to solid biomass fuels). SOA have not been included because the formation depends on a variety of factors not currently sufficiently quantified.

1.2 Aims and objectives

The overall aims of this thesis were to: 1) identify relationships between combustion conditions and aerosol emission characteristics, and 2) to link the emission characteristics with optically and toxicologically relevant particle properties that may accelerate atmospheric warming and have a negative impact on human health.

The physicochemical characteristics of the soot were investigated in relation to high and low temperature combustion, renewable and conventional diesel fuels, and fundamentally different combustion sources (diesel engine, biomass cook stoves, flame soot generator).

The specific aims of this thesis were to investigate knowledge gaps in relation to:

I. How diesel engine combustion temperatures, controlled by exhaust gas recirculation, influence the in-cylinder soot formation and soot oxidation processes, and the resulting physicochemical characteristics of diesel soot emissions. (Papers 1 & 5)

II. The relative importance of refractory and non-refractory soot components on the light absorption of BrC particles. (Papers 2 & 4)

III. The interpretation and analysis of refractory carbon cluster fragments in a soot particle aerosol mass spectrometer (SP-AMS). (Papers 3 & 4)

IV. The qualitative effect of combustion temperatures on carbon nanostructures and soot maturity, and the corresponding relationships between the particle light absorption wavelength dependence and soot maturity determined by direct measurements (HRTEM), or by inference from SP-AMS refractory carbon cluster distributions. (Papers 3 & 4)

V. How oxygen-containing and renewable fuels influence soot emission levels and characteristics from diesel engines, and how diesel engine combustion temperatures and soot maturity influence the generation of reactive oxygen species (ROS) of relevance for soot toxicity. (Paper 5)

2 Soot processes

2.1 Soot maturity and the evolution of soot in flames

The carbonaceous soot particles form from gas-phase reactions in hot and fuel-rich environments. Polycyclic aromatic hydrocarbons (PAHs) are known soot precursors and their formation in flames is closely related to soot formation. Fuel pyrolysis results in the breakdown of fuel molecules and the formation of new products. The hydrogen-abstraction-C_2H_2-addition (HACA) mechanism is a well-established theory to describe the build-up of large aromatic structures in flames [31]. Since soot formation occurs in flames using different fuels at various temperatures, there may be many reactions and precursor molecules responsible for the formation of the first aromatic structures in flames. Often, acetylene (C_2H_2) and propargyl (C_3H_3) are assumed to play a key role [32]. Acetylene and propargyl react to form cyclopentadienyl (C_5H_5) which rapidly reacts to form benzene. Hydrogen abstraction from benzene forms a phenyl radical (C_6H_5), and the subsequent acetylene addition in two steps followed by hydrogen abstraction and rearrangement lead to the formation of naphthalene ($C_{10}H_8$) [33], the smallest PAH which consist of two aromatic rings.

The first carbonaceous particles that form inside hot and fuel-rich environments of a flame are termed *incipient soot particles*. These particles are merely molecular clusters of a few nanometers in size. The incipient soot particles were recently proposed by Johansson et al. [34] to be formed by the clustering of hydrocarbons through radical-chain reactions involving five-membered resonance-stabilized radical (RSR) species. Starting with cyclopentadienyl, the addition of acetylene or vinyl (C_2H_3) and hydrogen abstraction generates a pool of larger RSR species. The RSR species cluster from chain-like reactions with other available hydrocarbons, keeping their radical character, and forming large covalently bonded clusters [34].

Soot particles are often characterized by core-shell structures, with a disordered inner core and an ordered outer shell. The inner core is related to the lower formation temperatures and properties associated with the formation of the incipient soot particle. The outer shell is hypothesized to result from the surface rearrangement of polycyclic aromatic units [35], and a preferential growth by gas-phase addition of acetylene

through the HACA mechanism leading to a more ordered growth at higher temperatures [36]. Johansson et al. proposed a similar mechanism in which the growth from incipient particles to larger soot particles was suggested to proceed from the chemisorption of smaller hydrocarbons to RSR moieties existing on the particle [34]. Figure 4 shows the schematic overview of the soot formation pathway suggested by Johansson et al. [34].

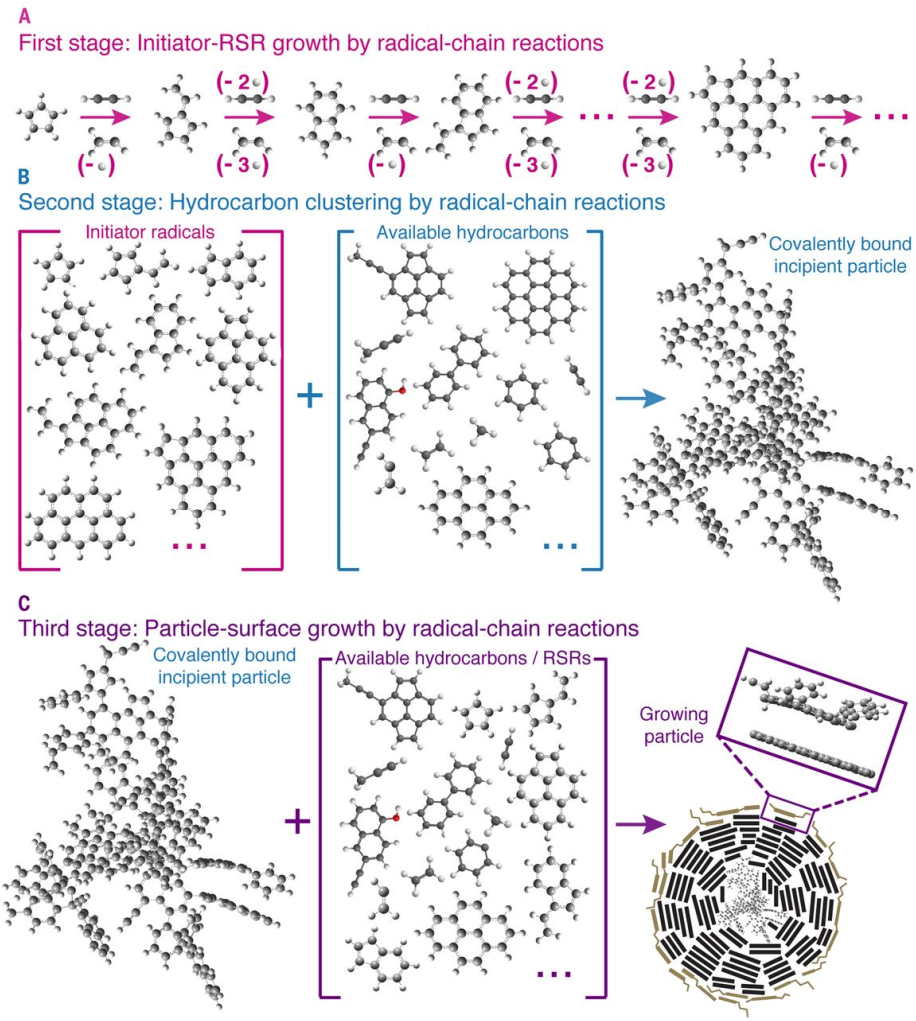

Figure 4. From [34]. Schematic overview of the clustering of hydrocarbons by radical-chain reactions (CHRCR) mechanism. (A) The CHRCR mechanism is initiated and propagated by resonantly stabilized radicals sequentially generated through radical-chain reactions involving acetylene or vinyl. (B) To form an incipient particle, these RSRs can cluster a wide range of hydrocarbons, including radicals, stable PAHs, and unsaturated aliphatic species, through radical-chain reactions fueled by loss and gain of extended conjugation. (C) Cyclopentadienyl-type moieties on cluster surfaces are posited to further propagate growth via the CHRCR mechanism. Reprinted with permission from AAAS.

The evolution of soot with time in flames is closely connected to an increasing sp^2/sp^3 bonding ratio and the stacking of aromatic units into graphitic structures [37, 38]. High-resolution transmission electron microscopy (HRTEM) and subsequent fringe analysis have been widely applied as the main technique to characterize the size, curvature, stacking, and orientation of these refractory building blocks: the polycyclic aromatic units (Figure 5). The soot nanostructure is closely related to both soot oxidation rates [12, 39-41] and the optical properties of the soot [37, 42]. Optical properties are closely related to the soot climate impact, and soot oxidation rates have important implications for the development of emission mitigation techniques (e.g., diesel particulate filters).

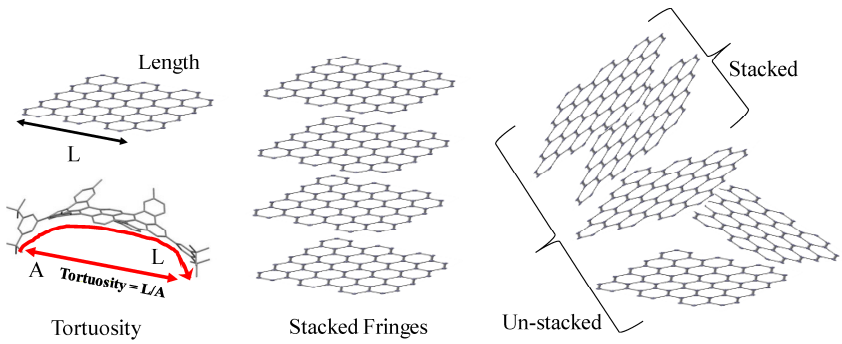

Figure 5. From [43]. Fringe parameters characterizing the carbon nanostructure.

Soot maturity describes the soot evolution in flames. The term "immature soot" is used to describe the soot found shortly after the first particles have formed in a flame. The immature soot and incipient particles are characterized by high hydrogen to carbon (H/C) ratios and disordered structures composed of small and often curved polycyclic aromatic units [11, 35, 37]. The disordered structures likely reflect the random growth of clusters at low temperatures [36], while curvature reflects the formation of five-membered (C5-containing) in addition to six-membered ring PAHs [11, 44]. Subsequent growth of immature soot particles is characterized by an increasing degree of graphitization (stacking and growth of polycyclic aromatic units in the soot primary particles), less curvature, lower H/C ratios, and increased resistance to oxidation. In sharp contrast to immature soot, mature soot is characterized by larger polycyclic aromatic units, a high degree of structural order with longer and less curved aromatic units, low H/C ratios, and BC absorption properties.

The maturity of soot particles depends on the temperature-time history of the particle. Therefore, longer residence times or/and high temperatures favor carbonization and graphitization processes that result in soot emission of a mature character [35].

2.2 Combustion emissions and soot maturity

Diesel combustion is normally characterized by high temperatures and high pressures. In a diesel engine, the liquid diesel fuel is injected at very high pressures into the cylinder. The fuel jet brakes up into small fuel droplets. As the spray moves, it entrains hot air which evaporates the fuel droplets and creates a premixed fuel-air mixture. Not all fuel is evaporated, and the latter part of the combustion is controlled by evaporation of fuel droplets and mixing of air into the combustion zone. The energy release in the diesel combustion therefore has two main parts: (1) the combustion of the premixed fuel-air mixture, and (2) the mixing (diffusion) controlled combustion of burning fuel droplets [45]. Figure 6 shows a conceptual description of a burning diesel fuel spray [46]. Soot and NO_x formation processes are mainly related to the diffusion-controlled combustion, although air entrainment prior to the fuel-rich premixed flame is a parameter that controls the amount of soot formed. In diesel combustion, soot formation occurs in the fuel-rich regions while soot oxidation and NO_x formation occur preferentially in the high temperature fuel-lean zone of the diffusion flame [45].

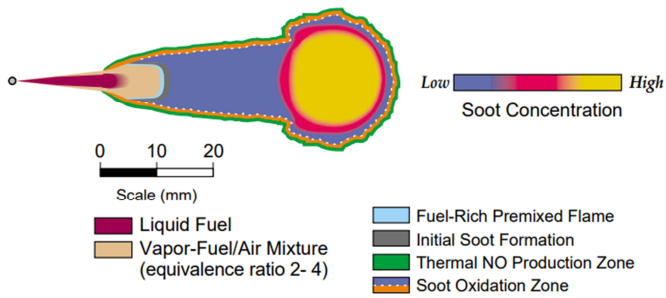

Figure 6. Conceptual model of NO_x and soot formation regions, and soot oxidation regions in combustion of a diesel engine spray. From [46]. Reprinted with permission from SAE International.

Soot maturity has so far primarily been associated with soot processes in controlled laboratory flames; however, the ordering of soot nanostructures with increasing soot maturity is not limited to these model systems. The HRTEM analysis of diesel particles extracted from an engine cylinder at different timings after ignition revealed that the soot maturation process and related graphitization are generalizable to real combustion systems such as diesel engines [47]. In this thesis, the term “soot maturity” is used as a qualitative description of soot, featuring different nanostructures and optical properties. Experiments were conducted to investigate relationships that are not well understood between soot maturity and optically and toxicologically relevant particle properties of combustion emissions.

The carbon nanostructures of soot in emissions are related to combustion temperatures [36, 48]. There is also a long-established connection between low temperature combustion processes and the elevated light absorption wavelength dependence of soot emissions [10, 49]. The temperatures associated with biomass combustion are highly variable, and soot emissions are typically characterized by a low degree of order in HRTEM analyses [48]. The soot evolution in high temperature combustion that is associated with conventional diesel engine combustion results in soot emissions of a mature character. The diesel soot particles are characterized by larger sized polycyclic aromatic units [48] and typical BC absorption properties [50]. However, modern diesel engine concepts, in which engines operate at lowered combustion temperatures to reduce the NO_x formation, influence the maturity of emitted soot particles. Soot emissions from diesel engines operating at reduced combustion temperatures have been shown to become more immature, characterized by shorter, curved, and more disordered nanostructures [12, 44, 51]. Additionally, the nanostructure of diesel soot is sensitive to the blending or complete substitution of diesel with oxygenated fuels [52]. This is of particular relevance when renewable but oxygen-containing fatty acid methyl ester (FAME) fuels are used as the substitution.

The type of combustion device, the fuel, and the operating conditions are important with respect to the emission characteristics of low and semi-volatile compounds that may condense to the particle phase when the exhaust gases cool. High temperatures and efficient combustion in diesel engines result in a low formation of fuel derived organic particle components. The organic and inorganic components found on diesel soot have instead been shown to originate mainly from the oil used to lubricate the piston and cylinder walls [53].

Due to the inhomogeneous conditions found in many biomass combustion systems, fuel pyrolysis temperatures are highly variable. The non-refractory organic contribution to the total particulate mass emitted from biomass combustion is therefore fuel derived and generally much higher than for diesel engines. Cellulose, hemicellulose, and lignin are the main combustible components in biomass. Hemicellulose decomposes at the lowest temperatures, at 470-530 K, while cellulose decomposes at slightly higher temperatures. Lignin is the thermally most stable component and decomposition starts at temperatures between 550-770 K [54]. The pyrolysis of these components has been extensively studied, and a detailed description is outside the scope of this thesis. The spatial variations in the temperature of many biomass combustion devices mean that the characteristics of the emissions will also differ due to the differences in pyrolysis temperatures. In short, the low temperature “tar” pyrolysis products found in the emitted particles are characterized by low molecular weight oxygenated hydrocarbons (e.g., levoglucosan from cellulose and large methoxy phenols from lignin). Higher

temperatures first result in phenolic and smaller aromatic compounds, and eventually more complex aromatic compounds and larger PAHs are formed [54].

2.3 Absorption and optical properties

The refractive index of a material can be used to describe the scattering and absorption of electromagnetic waves by particles. The imaginary refractive index (*k*) describes the attenuation of light and therefore strongly relates to absorption. BC materials have a nearly constant *k* with wavelength (λ). For BrC, *k* decreases with increasing wavelength. For practical purposes, the absorption Ångström exponent (AAE) is commonly applied to differentiate BrC from BC. AAE is an empirical measure of the absorption wavelength dependence of absorption. AAE is related to the mass absorption coefficient (i.e., MAC value) assuming a power-law dependence, shown in Eq. 1 [10]. *K* in Eq. 1 is a constant.

$$\mathrm{MAC}(\lambda) = K \times \lambda^{-\mathrm{AAE}} \quad \text{Eq. 1}$$

BC is defined by an AAE of ~1 [20]. BrC is associated with significantly higher AAEs that range from 1.5 (e.g., tar balls [55]) to ~11 for BrC associated with some secondary organic aerosols [24].

All soot is not BC. This has long been recognized for soot in flames. The soot evolution in flames (described in section 2.1 as a maturation process) is accompanied by a simultaneous evolution of optical properties. The incipient soot is characterized by high AAEs [56], and the evolution in optical properties is manifested by increasing MAC and decreasing AAE with time in the flame [37, 56, 57]. This occurs as a direct result of the increasing soot maturity and graphitization. Minutolo et al. [42] interpreted the evolution of optical properties in terms of band-gap energies. The band gap is directly related to the size of sp^2-bonded carbon clusters [58]. This enabled a physical explanation for the observed evolution of optical properties [42]. More recent studies have directly evaluated the relation between the optical band gap and the size of aromatic clusters [59-61], which has been corroborated by modeling of band gaps for PAHs of various shapes and sizes [61, 62].

The AAE is closely related to the optical band gap. The band gap describes the energy required for an electronic transition between the highest occupied molecular orbital (HOMO) and the lowest unoccupied molecular orbital (LUMO), which is known as the HOMO-LUMO gap. The band-gap energy (E_g) is proportional to the absorption

coefficient (b_{abs}) through Eq. 2 [61]. The absorption coefficient (in units of m^{-1}) is related to the $MAC(\lambda) = b_{abs}(\lambda)/m_p$, where m_p is the suspended particle mass (g/m^3).

$$hv * b_{abs} \propto (hv - E_g)^r \quad \text{Eq. 2}$$

In Eq. 2, *hv* denotes the photon energy and *r* is a constant describing the type of transition. The constant *r* is often assigned a value of 2 indicating an *indirect allowed* transition. The work presented in this thesis follows the procedures of recent literature [59, 60] that assign $r = ½$, under the assumption that polycyclic aromatic hydrocarbons have *direct allowed* optical band gaps. Band-gap energies of semi-conducting materials can be obtained from optical absorption measurements at wavelengths with energies slightly above the band gap [63]. The determination of band-gap energy is described in the methods section. It is important to note that different assumptions regarding the type of transition and *r* will result in different optical band-gap energies, which can obstruct a direct comparison to the literature.

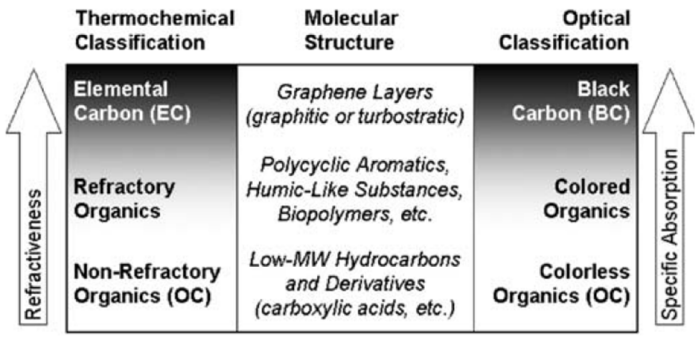

Figure 7. Classification and molecular structure of carbonaceous aerosol components. From [64]. Reprinted with permissions from Springer Nature.

The transition from BrC to BC materials, the increase in light absorption, and the decrease in wavelength dependence are associated with increasing molecular size and decreasing material volatility [64]. This is shown qualitatively in Figure 7. Section 4.3 presents results and a continued discussion on the absorption properties of soot.

2.4 Soot toxicity

Exposure and inhalation of particulate matter have been shown to induce oxidative stress, inflammation, fibrosis, and cytotoxicity. Among these toxicological effects, oxidative stress has been identified as a main route for particle-induced health effects [14]. Oxidative stress is defined as an imbalance between the production of reactive oxygen species (ROS) and their removal by antioxidants. The toxicological pathways related to oxidative stress are illustrated in Figure 8. ROS causes oxidative stress [14] which can lead to DNA damage, mutations and result in various respiratory diseases, including cancer [15].

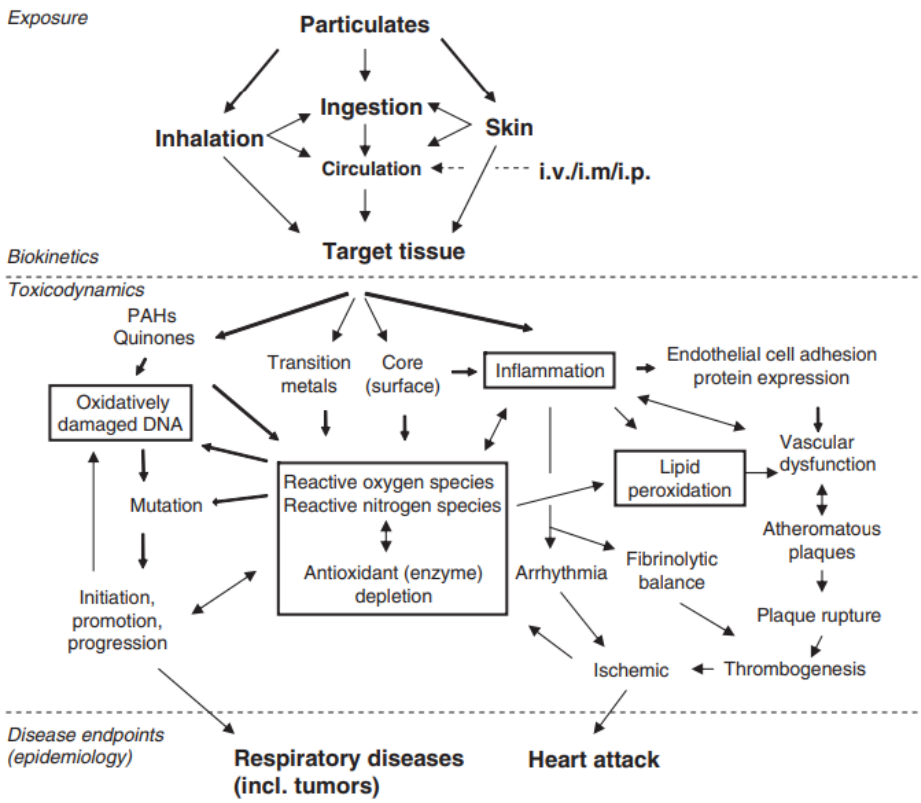

Figure 8. Hypothetical pathways for particle-induced oxidative stress and death or hospitalization for cancer and cardiovascular diseases. Re-printed from [15] with permission (Free Radical Research, Taylor & Francis).

The generation of ROS can follow a direct path by reactions with particle components and on particle surfaces [14]. This occurs, for example, for soluble PAHs and surfaces of insoluble soot or carbon black particle. Particles deposited in the lungs can cause

inflammation. The biological response to inflammation in the lung generates ROS. Inflammation therefore provides an indirect path for generating ROS that can lead to oxidative damage from similar mechanisms to the direct particle-induced ROS. The particle-induced inflammation can also induce plaque formation, granuloma, and fibrosis, which can ultimately lead to a number of diseases that have been linked to air pollution, including cardiovascular diseases and stroke [3, 14, 15]. Thus, particle-induced oxidative stress and inflammation provide plausible toxicological mechanisms for the epidemiological evidence that attribute various diseases and deaths to the exposure to particulate matter [3].

Toxicity and oxidative stress induced by combustion particles have been mainly associated with: (1) soluble organic compounds such as PAHs and quinones, (2) transition metals such as Fe, Cu, and Zn, and (3) non-soluble refractory carbonaceous soot [65]. As previously described, these different compound classes are in combustion emissions often found in internal mixtures (i.e., as condensed or adsorbed organic and inorganic material to the refractory carbonaceous soot surfaces).

Differentiating the toxicity of the non-soluble refractory soot, which is often directly related to BC, from PAHs and transition metals is a major issue to overcome in our understanding of what contributes to the toxicity of combustion emissions. Nonetheless, several mechanisms have been identified through in-vivo studies and animal models, in-vitro cell studies, and cell-free studies. The in-vitro inflammatory response of human macrophage cells exposed to organic material on soot surfaces and refractory carbonaceous soot particles stripped from organic material has been shown to result in the release of different inflammatory mediators [66]. PAHs and quinones induce ROS formation mainly from their redox-cycling ability, and transition metals such as Fe through catalysis and Fenton reactions [14]. Carbon black represents engineered refractory carbonaceous particles that are very similar in composition to the refractory carbonaceous soot particles (without condensed organics) emitted from combustion [15]. Both diesel soot (with condensed organics) and carbon black particles (without condensed organics) can have strong ROS generating abilities [16, 67]. These results show the importance of considering the carbonaceous particle itself, as well as soluble organic material, when assessing the toxicity of combustion emissions.

There is an established link (Figure 9) between the particle surface area, the ROS-forming potential, and the induced inflammation [16, 67-69]. This relation is important as it: (1) provides a link to a quantifiable particle property, and (2) suggests that surface properties will be an additional factor governing particle toxicity.

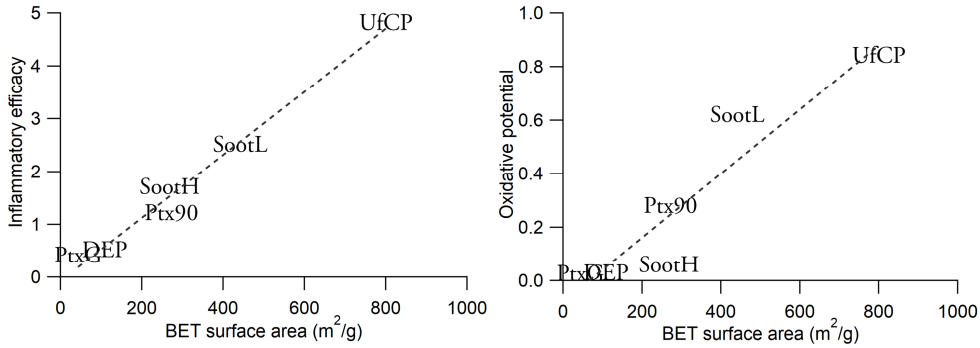

Figure 9. Inflammatory efficacy (left) and oxidative potential (right) versus BET surface area for a number of different soot and carbon black particles. The data originates from Table 1 in Stoeger et al. (2009) [16]. Inflammatory efficacy refers to the in-vivo relative increase (compared to a control) of pulmonary nutreophils per instilled particle mass. Oxidative potential refers to the consumption of ascorbate per particle mass (nmol/µg). Abreviations as follows: Spark discharge ultrafine carbon particles (UfCP) from graphite electrodes, PrintexG (PtxG) and Printex90 (Ptx90) are two commercially available carbon blacks, Cast burner flame soot with high (SootH) and low (SootL) organic carbon content, and reference diesel soot (DEP) from the National Institute of Standards and Technology (NIST).

By exposing soot and benzo[e]pyrene-coated soot to O_3, an increased ROS-generating ability of the soot was linked to the formation of quinones and oxidation of PAHs or PAH-like soot structures [70]. It is not far-fetched to hypothesize that the oxygen functionalization on soot surfaces (i.e., on refractory constituents) is directly related to the ROS-forming ability of the soot. Soot nanostructures are closely related to soot oxidation rates. Less ordered, more defect nanostructures have lower oxidation onset temperatures and higher soot oxidation rates [41, 71], and a less ordered nanostructure has been hypothesized to increase soot toxicity [65]. However, if all biologically relevant particle interactions occur with particle surfaces, the in-flame oxidation on soot surfaces may play a key role in soot toxicity. Surface defects in the soot nanostructure first decrease as soot matures during soot formation. However, defects again increase when soot surfaces are later oxidized. The oxidation on soot surfaces results in the breakage of aromatic bonds, leading to defect surfaces with exposed reactive edge sites and surface oxygen functionalization [72]. Thus, mature soot emissions which have undergone significant in-flame or post-flame oxidation may possibly induce the highest toxicological response. At the same time, in-flame oxidation can reduce the primary particle sizes of soot, thus increasing the soot surface area which additionally can increase the particle toxicity. Paper 5 of this thesis describes experiments with the aim to evaluate the relation between the ROS forming potential, surface area, and composition of diesel exhaust particles from combustion with fossil and renewable fuels, and at reduced combustion temperatures to simultaneously mitigate the diesel engine NO_x emissions.

3 Methodology

Experiments were conducted so that one or several variables that influenced the combustion temperatures were altered systematically. Changes in the physical and chemical characteristics of the combustion emissions were investigated primarily using an on-line soot particle aerosol mass spectrometer (SP-AMS) and an aethalometer. In several of the studies, soot samples were additionally collected for off-line thermal-optical carbon analysis and high resolution transmission electron microscopy (HRTEM).

In Paper 1, the evolution of soot properties was studied as a function of time inside the combustion cylinder of a heavy-duty diesel engine and as a function of exhaust gas recirculation (EGR) to reduce combustion temperatures.

In Papers 2 and 3, a flame soot generator that used N_2 to dilute the fuel and reduce combustion temperatures was utilized to produce emissions that varied with respect to the soot maturity and the optical properties.

In Paper 4, the soot composition, nanostructures, and optical properties were characterized for soot produced at different combustion temperatures in the flame soot generator and a diesel engine that used EGR and was fueled with either fossil diesel or renewable fuels.

In Paper 5, heavy-duty diesel engine emissions were characterized for combustion with one conventional (fossil) and two renewable diesel fuels, and for altered combustion temperatures (by varying EGR). The particulate emissions were investigated in relation to their potential to form reactive oxygen species (ROS).

In addition, the thesis research includes an experimental study on combustion emissions from a number of African cook stoves, described in section 3.1.3.

3.1 Combustion sources

3.1.1 Flame soot generator

In the Papers 2 and 3 studies, a miniCAST soot generator (Model 5201C, Jing Ltd., Switzerland) was employed to study how physical, chemical and optical soot characteristics changed with respect to soot maturity. The principles of operation are illustrated in Figure 10. The miniCAST consists of a co-flow diffusion flame where propane fuel is supplied in the center of the burner, and the air (oxidizer) is supplied on the perimeters. The flame is quenched (using N_2) at a set specific height above the fuel outlet. The miniCAST combustion conditions were altered by changing the flow rate of the oxidation air and by mixing the fuel gas with a flow of inert N_2 gas. The addition of N_2 effectively lowers combustion temperatures and simultaneously increases the cold gas flow, simulating a lowered effective quenching height of the flame. A reduced oxidation air flow has a similar effect by increasing the cold gas flow velocity relative to the oxidation air flow.

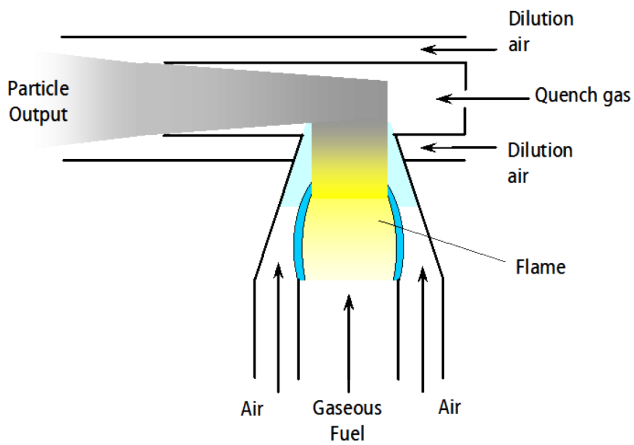

Figure 10. The MiniCAST operating principle. Propane gas is supplied in the middle (Gaseous Fuel). The fuel gas can additionally be mixed with an adjustable inert N_2 (not shown) prior to entering the combustion chamber. Oxidation air (Air) is supplied on the perimeters and the flow rate can be adjusted. A constant flow of N_2 (Quench gas) is used to quench the flame at a set height above the fuel outlet. The exhaust can be further diluted by air (Dilution Air). The dilution is adjustable between ~0-3 times dilution. Reprinted with permission from Jing Ltd.

The miniCAST operating settings used are detailed in Table 1. In the results and discussion section, soot properties have been plotted versus the miniCAST N_2 gas flow. However, as shown in Table 1, a change in the N_2 flow was always accompanied by a reduction of the oxidation air flow. The internal dilution air was adjusted between 0-20 liters per minute (up to about 1:2 dilution) depending on the experimental set-up.

Table 1.
MiniCAST operating conditions.

MiniCAST Operating point	Propane (C_3H_8)	N_2 mixing gas for fuel	Oxidation air	Quench gas N_2	Internal dilution air
	[ml/min]	[ml/min]	[l/min]	[l/min]	[l/min]
1	60	0	1.55	7.0	0-20
2	60	50	1.54	7.0	0-20
3	60	100	1.52	7.0	0-20
4	60	150	1.50	7.0	0-20
5	60	200	1.47	7.0	0-20
6	60	250	1.42	7.0	0-20
7	60	300	1.36	7.0	0-20
8	60	330	1.32	7.0	0-20

3.1.2 Heavy-duty diesel engine

The diesel engine experiments were performed on an experimental heavy-duty Scania D13 engine. The engine was modified to only operate one out of the six cylinders. An exhaust gas recirculation (EGR) system was fitted to the engine. The EGR system recirculates cooled exhaust gases back to the intake manifold where it mixes with air. This results in a reduced intake air O_2 concentration when a part of the O_2 in air is substituted by (mainly) CO_2 from the exhaust. A representative drawing of the engine and sampling set-up is shown in Figure 11.

Only minor adjustments were made to the engine's operating parameters between the different experiments. In short, the engine was operated with fuel injection pressures of 2000 bar (Paper 1) or 1200 bar (Papers 4 & 5), a speed of 1200 rpm, a low load of 5-6 bar (gross indicated mean effective pressure, IMEPg), an intake air pressure of 1.5-2 bar, and intake air temperatures between 30-100°C.

The engine was operated with Swedish MK1 petroleum-based diesel fuel with no blending of renewable fuels (B0). In Papers 4 and 5, the engine was additionally fueled with renewable hydrotreated vegetable oil (HVO) and rapeseed methyl esters (RME). Readers with a particular interest in emissions from renewable fuels may wish to consider additional results from experiments that were conducted outside the scope of this thesis, but with a similar engine set-up and combustion with methanol and ethanol [73].

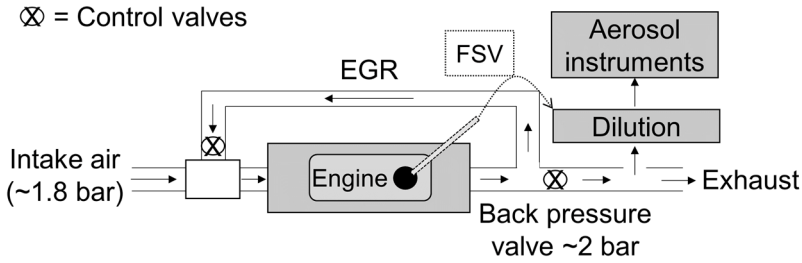

Figure 11. Simplified illustration of the experimental engine set-up. More precise descriptions of the experiments can be found in the appended papers.

In the Paper 1 study, a fast gas sampling valve (FSV) was used to extract particles from the cylinder. The FSV was mounted in one of the exhaust ports. The tip of the sampling probe was adjusted to a few millimeters inside the combustion chamber. Due to this sampling position, the extracted sample can therefore be considered as representative of the local conditions close to the probe. However, high speed imaging in a similar engine showed that due to swirl and turbulence, the mixture became relatively homogeneous shortly after the start of combustion [74].

The valve opening was triggered so that a small gas volume was extracted from a specific time interval of each combustion stroke. Figure 12 shows the measured heat release rate (HRR) and NO_x concentration in the extracted in-cylinder gases. The steep increase in the measured NO_x concentration indicates that the sampling duration was very short, 4-6 crank angle degrees (CAD) or less, at the high in-cylinder pressures close to 0 CAD. The opening duration was controlled so that the gas flow out of the FSV was constant at 1 l/min (600 extractions per minute). The gas extracted from the cylinder was therefore rapidly averaged over many combustion cycles, which is important for a representative sample of the average in-cylinder conditions.

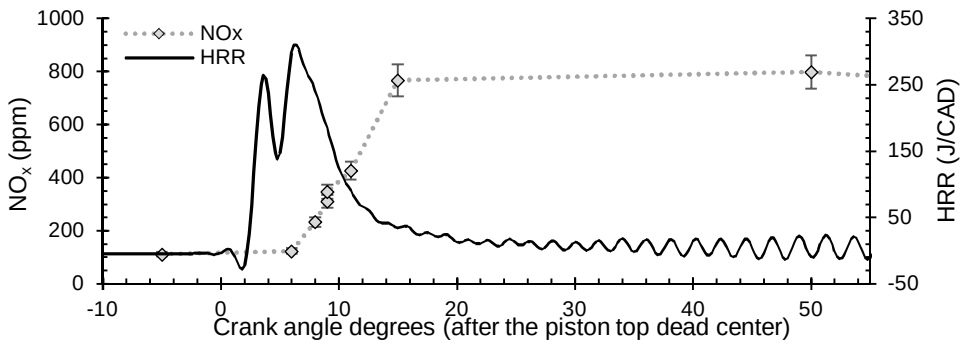

Figure 12. In-cylinder heat release rate (HRR) and NO_x concentration in the extracted gas.

3.1.3 Biomass cook stoves

This research was part of the SUSTAINE study that was carried out at Umeå University (Sweden) in 2016. The aim of the study was to characterize health and climate relevant emissions from cook stoves used in Sub-Saharan African. The cook stoves, fuels and measurement techniques are described briefly below, and more detailed information can be found in Korhonen et al. [75].

Emissions were studied from a 3-stone fire, a rocket stove, a natural draft (ND) gasifier pellet stove, and a forced draft (FD) gasifier pellet stove. A pot filled with water was placed on top of the stoves. The 3-stone fire stove, rocket stove, and natural draft gasifier are shown in Figure 13. The forced draft gasifier stove (not shown) was the technologically most advanced stove. The 3-stone fire stove consists of burning wood sticks that are surrounded by three stones on which the pot with water was placed. The rocket stove is technologically more advanced than the 3-stone cook stove and consists of a simple metal cylinder with an opening from one side at the bottom. Wood sticks are inserted into the rocket stove at the bottom and the natural draft air causes a hot burning flame in the vertical section.

In the natural and forced draft gasifier stoves, a bed of wood pellets is centered near the bottom of the cylinder-shaped stoves. The stoves were lit with ethanol from the top, and the heat volatilizes combustible gases from the fuel bed in a pyrolysis process. Primary air is supplied from the bottom. Secondary air is supplied near the top of the stoves, closer to the pot. When the volatile gases that are released in the pyrolysis of the fuel mixes with the secondary air it produces a hot burning flame. The forced draft stove uses an electrical fan to control primary and secondary air flow rates, while the natural draft use no electricity. The 3-stone fire and the rocket stoves were fueled with wood sticks of casuarina, a common fuel in Sub-Saharan Africa. The fuel was collected in Kenya. The two gasifier stoves used standard Nordic softwood pellets consisting of a 50:50 % mixture of pine and spruce.

The test procedure consisted of a 45 minute water boiling test. The exhaust from the combustion process were sampled with an extraction hood (1:20-1:50 times dilution). The emissions were further diluted and continuously injected into a stainless steel chamber over the full test period. The averaged emissions properties, over the full water boiling test, were in this way investigated based on the aerosol properties in the stainless steel chamber when the test had ended.

In addition to the average emission properties, transient combustion emissions were analyzed for the rocket stove and natural draft gasifier stove. In this case an ejector dilution system 1:100 was used in addition to the primary dilution in the extraction hood. The transient rocket stove emissions corresponded to two combustion phases

that were repeated, a fuel addition phase and a flame phase. The fuel addition phase corresponds to the short time period (<2 minutes) after the wood sticks had been pushed further into the fire. The flame phase corresponds to emissions averaged starting from a few minutes after the fuel addition phase had ended and a stable period over 1-2 minutes. For the natural draft gasifier stove, the transient data also includes emissions not included from the water boiling test (i.e., prior to injecting the emissions into the chamber), the emissions include: the initial low temperature pyrolysis phase (~0-30 seconds after the stove was lit); the start of the flame phase (~2-4 minutes after the stove was lit); the early flame phase (~8-21 minutes after the stove was lit); the late flame phase (~32-42 minutes after the stove was lit); the burn out phase ~53-58 minutes after the stove was lit).

Figure 13. The 3-stone fire (left), the rocket stove (middle), and the natural draft gasifier (right). For all three stoves, the flames can be seen to impact on the bottom of the black pot that was filled with water.

3.2 Aerosol characterization

3.2.1 Soot particle aerosol mass spectrometer (SP-AMS)

The soot particle aerosol mass spectrometer (SP-AMS, Aerodyne Research Inc., U.S.A.) is an instrument that enables characterization of the chemical composition of refractory light absorbing aerosol particles [76]. Particles enter the SP-AMS through an aerodynamic lens that focuses particles (~40-1000 nm) into a narrow beam. The air/gas is simultaneously removed by several turbopumps down to high vacuum (10^{-7} mbar) in the extraction and detection regions of the instrument. The narrow particle beam is focused onto an extraction region where particles are vaporized. After the vaporization, the gas molecules are ionized by electron impact ionization (70 eV) and accelerated and detected in a high-resolution time of flight (HR-TOF) mass spectrometer to determine their mass to charge ratio (m/z), with a resolving power m/Δm of approximately 2000

at m/z 28 (m being the nominal m/z and Δm referring to full width at half maximum). A schematic is shown in Figure 14.

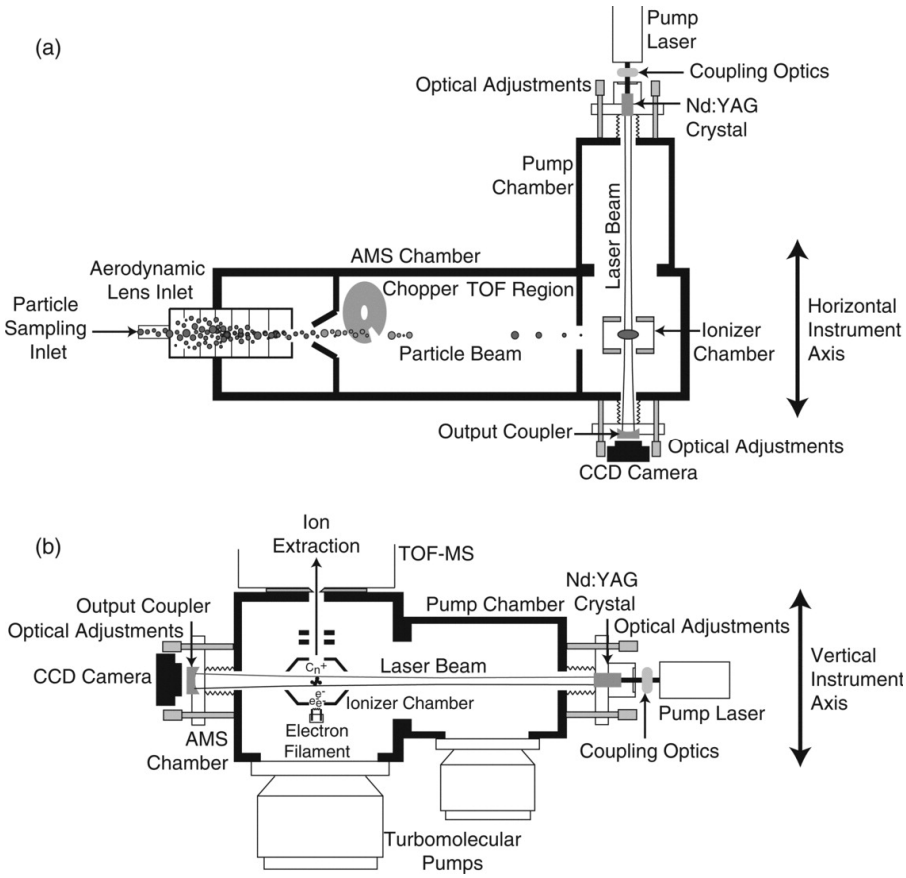

Figure 14. From [76]. Schematic drawing of the SP-AMS. Reprinted with permission from *Aerosol Science and Technology* © American Association for Aerosol Research.

Particle vaporization is a delicate matter in which the particle material is volatilized to allow detection in the gas phase. The SP-AMS utilized in this thesis research had dual vaporizers: a conventional thermal-desorption tungsten vaporizer (at 600°C) and a laser vaporizer (Nd:YAG, 1064 nm). When particles impact on the tungsten vaporizer, semi-volatile material will flash vaporize. This allows detection of what is operationally defined as non-refractory aerosol components. This vaporization method may also be referred to as the standard or conventional AMS mode [77-80]. When refractory carbonaceous particles, which absorb infrared (IR) radiation at 1064 nm, pass through the laser beam, they heat up and reach temperatures high enough (~4000K) to vaporize

graphitic material. This allows the detection of refractory material that can absorb light at 1064 nm.

When a soot particle coated with semi-volatile material begins to heat up, the semi-volatile material will first evaporate from the refractory particle surfaces. Thus, the laser vaporization also enables detection of semi-volatile material if this is condensed or adsorbed on surfaces of refractory material. Because molecular fragmentation is sensitive to temperature, the resulting fragments and mass spectra of the non-refractory aerosol can differ slightly between conventional flash vaporization and laser vaporization [76]. The laser module can be switched off, and for the majority of the experiments conducted, the non-refractory aerosol components were defined by mass spectra from the conventional AMS mode, using vaporization at the tungsten surface heated to 600°C only. The majority of aliphatic organic species fragment to clusters with masses below 120 Da. The organic aerosol was defined by the peak fitting of high-resolution (non-refractory) aerosol mass spectra and fragments of the form $C_{x\geq1}H_{y\geq1}O_{z\geq0}^{+}$ between 10-120 Da. PAHs are relatively stable to fragmentation, and a significant fraction of the signal intensity can be found at the parent peak corresponding to the molecular weight of the PAH isomer [81]. The non-refractory PAH concentrations were determined by scaling the parent peak signal of 7-10 unsubstituted PAHs with molecular masses between 202-300 Da ($C_{16}H_{12}$-$C_{24}H_{12}$) to an approximate average of the parent peak signal fraction (~0.25) previously determined from reference measurements using lab standards of different PAH isomers [81]. The PAH quantification does not allow the determination of which PAH isomer is present in the organic aerosol component.

The laser vaporization procedure is illustrated in Figure 15 [76]. When the sublimation temperatures of the refractory carbonaceous soot material is reached, molecular carbon clusters are generated (i.e., C_x fragments in the gas phase). Mature soot particles with a graphitized carbon nanostructure, for example BC particles, generate almost exclusively low molecular weight carbon clusters (C_{1-5}^{+}). The rBC concentration was therefore defined by the signal from C_{1-5}^{+} clusters, with the exception of the Paper 1 study in which rBC was calibrated from the total carbon cluster signal (C_{1-58}^{+}) and optically derived BC concentrations. Less mature soot particles or other materials (e.g., some types of carbon black particles) [76, 82] may generate higher molecular weight carbon clusters ($C_{\geq6}^{+}$) in addition to C_{1-5}^{+}. Soot particle aerosol mass spectra may also have additional signals from oxygen-containing carbon clusters ($C_xO_y^{+}$) related to the refractory material.

Mass calibration of non-refractory components in the AMS mode were performed with 300 nm (electrical mobility diameter) ammonium nitrate (NH_4NO_3) particles. The

reference mass was calculated by counting the particles in a condensation particle counter (CPC). In the AMS, the mass concentration of a species (C_s, μg/m^3) is calculated by Eq. 3 where: $\sum_f I_{sf}^{corr}$ is the total ion current of all fragments of a given species; mIE_{NO3} is the mass specific ionization efficiency of nitrate in ions per picogram; Q is the flow rate of air into the AMS in cm^3/s; RIE_s is the relative ionization efficiency for a given species with respect to nitrate; and CE_s is the collection efficiency of that species [77, 80].

$$C_s = \frac{\sum_f I_{sf}^{corr}}{mIE_{NO3} * Q * RIE_s * CE_s} \quad \text{Eq. 3}$$

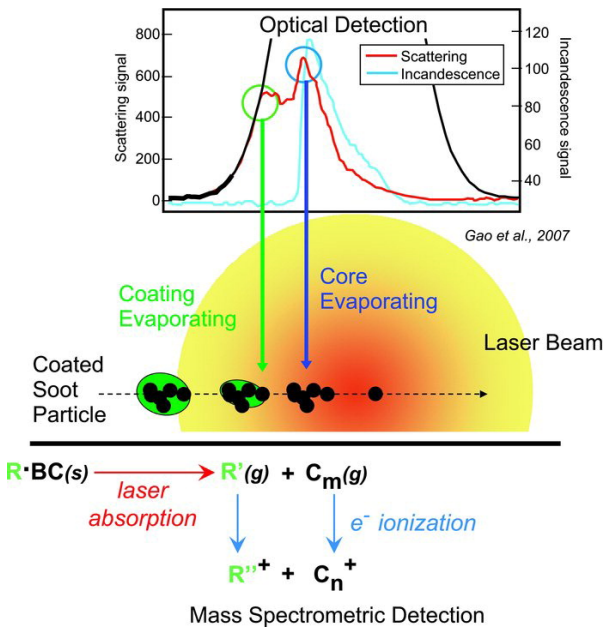

Figure 15. From [76]. Illustration of the SP-AMS laser heating and vaporization process. When a soot particle encounters the laser beam, the refractory carbonaceous material illustrated by the black particles absorb the radiation and heats up. Semi-volatile coating material will first evaporate as the refractory material begins to heat up. When the refractory material reaches the sublimation temperature it vaporizes. The gas phase molecules are ionized by electron impact ionization, and the ion clusters are detected in the mass spectrometer (bottom). The "optical detection" on the top of the illustration refers to laser scattering and incandence signals in a single particle soot photometer (SP2) instrument from which the SP-AMS laser module was adapted. Reprinted with permission from *Aerosol Science and Technology* © American Association for Aerosol Research.

The electron impact ionization cross section scales linearly with the number of electrons in a molecule [80]. However, the response (i.e., the slope) depends on the chemical composition, and is adjusted for using by including RIEs in the denominator. The

collection efficiency (i.e., the fraction of particles that were successfully focused into a narrow beam onto the vaporizer and fully evaporated) depends on the particle shape. Compared to a spherical particle, a non-spherical particle is less focused in the aerodynamic lens and therefore may have a lower collection efficiency. An accurate determination of the collection efficiency is often difficult, which is why the apparent RIE in this case will include effects related to CE. The collection efficiency is reduced for aerosols with irregular particle shapes (e.g., soot agglomerates) and size distributions extending outside the range in which the aerodynamic lens has a nearly constant transmission efficiency (below ~100 nm and above 500 nm) [83]. This can have a negative effect on the accurate determination of particle mass. In relation to this research, this may potentially induce errors when the combustion conditions changed and both particle shapes and size distributions were altered.

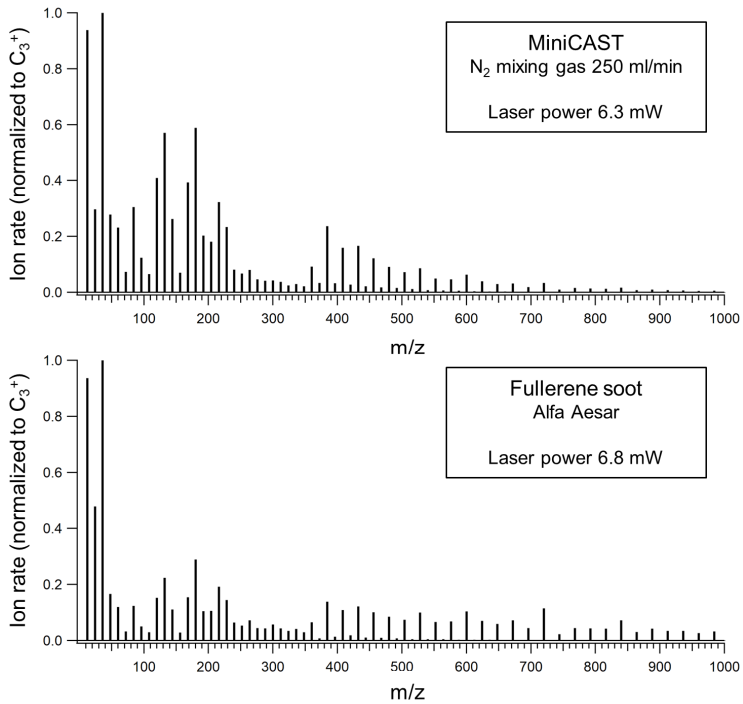

Figure 16. SP-AMS refractory carbon cluster distributions. **Top:** immature (OP6) MiniCAST soot. **Bottom:** fullerene soot (Alfa Aesar, Thermo Fisher Scientific, Germany). The laser power was measured from the output coupler mirror with an Ophir power monitor. The laser power was similar for both aerosol mass spectra.

Typically, for 1 pg NO_3 500-700 ion counts were obtained. The organic aerosol was assigned a relative ionization efficiency of 1.4 (relative to NO_3) [77]. The SP-AMS mass calibration of refractory BC (rBC) particles involves the aerosolization and size selection

(electrical mobility of 300 nm) of carbon black nanoparticles (Regal Black; Cabot Inc., USA). The typical response for 1 pg of Regal Black was ~150-300 ion counts. The relative ionization efficiencies of Regal Black to NO_3 were determined to ~0.2-0.4 in the different experiments.

The formation of different carbon clusters is of particular interest for the research in this thesis. The $C_{\geq 6}^{+}$ signals have previously been shown to be more sensitive to variations in the laser power compared to the signal from C_{1-5}^{+} clusters. Of further concern, signals from fullerene carbon clusters ($C_{\geq 30}^{+}$), were in a previous study, found at high laser power with the electron ionization turned off. This background signal increased with increasing size of the carbon clusters. This suggests that the signal intensity of fullerene carbon clusters may partially originate from a secondary (thermal) ionization mechanism [82]. The laser power dependence of carbon cluster distributions was investigated on immature miniCAST soot in the Paper 3 study. The results indicated that the response to laser power was similar for the sum of lowcarbons (C_{1-5}^{+}) and the sum of the smaller midcarbon and fullerene carbon clusters with masses less than or equal to 720 Da (C_{6-60}^{+}).

It was also found that the instrument tuning had a profound effect on the refractory carbon cluster distribution. At an ion extractor voltage tuning of -90 V, $C_{\geq 6}^{+}$ clusters were dominated by an envelope of very large fullerene carbon clusters (~C_{60-200}^{+}). Moreover, no signal from the intermediate midcarbon clusters (C_{6-29}^{+}) were detected with this voltage tuning. Tuning the ion extractor to a positive voltage (+20 V) had only a minor effect on the signals from the C_{1-5}^{+} clusters. However, this tuning produced mass spectra with the main signal from large carbons at C_{6-60}^{+}, for which the laser power was shown to have a low impact. The cause of the differences in refractory carbon cluster distribution between the two ion extractor tunings is not fully understood. If $C_{\geq 6}^{+}$ clusters from the laser vaporization process (secondary ionization mechanism) form earlier than clusters formed from electron impact ionization, it can be hypothesized that a positive ion extractor voltage that repel the positively charged clusters may be more selective towards clusters formed after electron impact ionization in the near vicinity of the ion extractor.

The Regal Black calibration particles produce almost exclusively C_{1-5}^{+} clusters. A calibration of $C_{\geq 6}^{+}$ signals is therefore not possible with Regal Black. Several different carbon black nanoparticles and combustion sources were investigated during the thesis work. Based on the similarity in carbon cluster distribution between fullerene soot (example presented in Figure 16 for Alfa Aesar, Thermo Fisher Scientific, Germany) and immature (OP6) miniCAST emissions, future studies that involve the SP-AMS analysis of $C_{\geq 6}^{+}$ signals may consider to validate the instrument tuning (laser power,

voltages, etc.) using this carbon black or a similar carbon black material. A well-defined calibration soot is also instrumental for a mass calibration of $C_{\geq 6}^{+}$ signals.

In Figure 8 of Paper 3 we relate the SP-AMS large carbon to lowcarbon ratio to the geometric mean fringe lengths derived from the HRTEM analysis. In Paper 4 we argue that the fragmentation of large carbons to C_1^+, which depends on laser intensity, could bias the analysis. A new parameter C_{3X}^{+} was therefore defined (Eq. 4) in Paper 4 to better represent changes in refractory carbon cluster distributions.

$$C_{3X}^{+} = \frac{C_3^+}{C_{1-60}^{+} - C_3^+} \quad \text{Eq. 4}$$

The dependence of $C_{\geq 6}^{+}$ clusters on laser power and instrument tuning raised concerns about the repeatability of measurements over time. Figure 17 shows the C_{3X}^{+} parameter for measurements on miniCAST soot conducted in 2015 and 2017. Overall a good repeatability was observed between experiments. The observed variability may be due to variations in the SP-AMS laser power and tuning as well as related to the miniCAST soot generator.

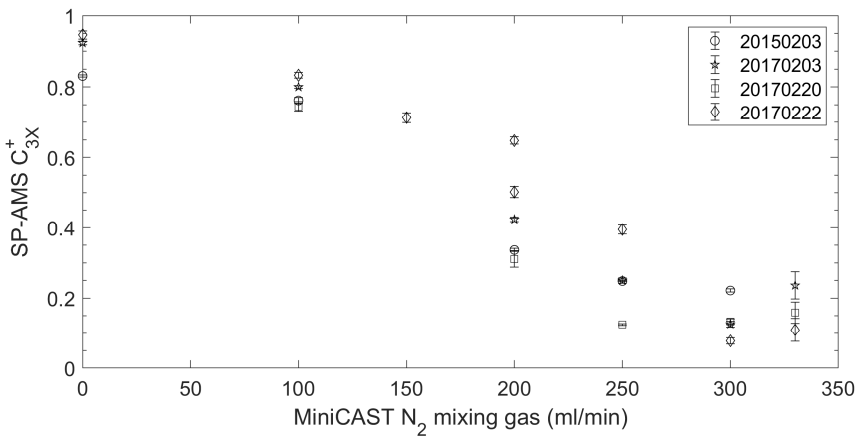

Figure 17. SP-AMS C_{3X}^{+} (defined in Eq. 4) for miniCAST soot studied on different dates in 2015 and 2017.

3.2.2 Light absorption measurements

Light absorption measurements were performed with an aethalometer (Model AE33, Magee Sci., U.S.A.) [84] at seven predefined wavelengths: 370, 470, 520, 590, 660, 880, and 950 nm. The aethalometer samples the aerosol through a filter on which particles are deposited. The attenuation of light through the filter is measured continuously, and the increase in attenuation is used to derive the absorption. Absorption is derived by correcting the attenuation of light by the multiple scattering parameter (*C*) which depends on the filter properties [85]. In a final step, the absorption is converted to a black carbon (BC), or an equivalent BC [20], mass concentration from a pre-determined calibration. New filter materials were distributed by the manufacturer between different experiments conducted in the course of the thesis work. Thus, different values for *C* have been used as instructed by the manufacturer.

BC was derived using the absorption measured at 880 nm or from the average absorption at 880 nm and 950 nm. Absorption is inversely proportional to the incident wavelength raised to the power of the absorption Ångström exponent (AAE). The AAE for two wavelengths can easily be derived by calculating the slope in the log-transformed absorption at two different log-transformed wavelengths (Eq. 5) [86]. In Eq. 5, $b_{abs}(\lambda)$ (m^{-1}) refers to the measured absorption coefficient for a given wavelength. Estimations of the AAE in this thesis research were derived by including all seven wavelengths ($AAE_{370\text{-}950nm}$) or the three longest wavelengths ($AAE_{660\text{-}950nm}$) and by linear fitting to the log-transformed absorption (y-axis) and wavelengths (x-axis).

$$AAE = (-1) * \frac{\log\left(b_{abs}(\lambda_{short})\right)}{\log\left(b_{abs}(\lambda_{long})\right)} / \frac{\log(\lambda_{short})}{\log(\lambda_{long})} \quad \text{Eq. 5}$$

Light scattering by the particles and the filter material can induce measurement artifacts. The AE33 includes techniques to compensate for these potential artefacts [84]. In the Paper 2 study, in-situ laser extinction measurements at four wavelengths (405, 650, 850, and 1064 nm) in a similar interval to the AE33 were carried out simultaneously with the aethalometer measurements. AAEs were derived for both instruments and a comparison is shown in Figure 18. The correlation between the two instruments was very good (r^2=0.94). The divergence was strongest for AAEs close to 1, and may have been the result of high aerosol concentrations (>100 µg/m^3) and filter loading effects. In the later studies a higher dilution ratio was therefore used.

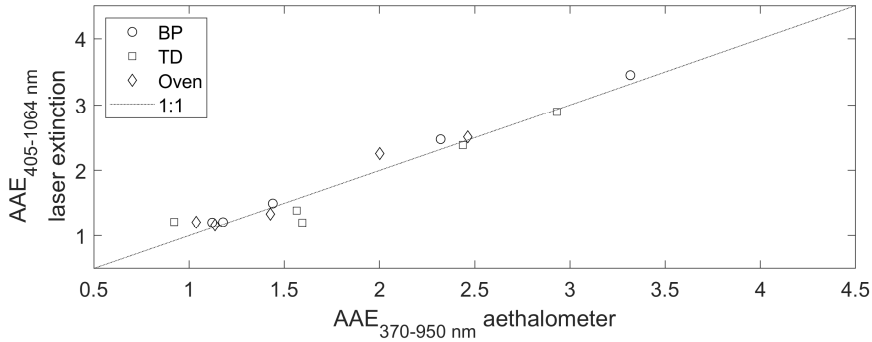

Figure 18. Absorption Ångström exponents (AAE) derived from laser extinction and aethalometer data of miniCAST soot (OP1, OP3, OP5, OP6, and OP7) that were eposed to either "no heating" (BP), "heating to 250°C" (TD), and "heating to 500°C" (Oven).

In the Paper 4 study, optical band gap energies were derived using a Tauc/Davis-Mott [63, 87] analysis from normalized $b_{abs}(\lambda)$ that were predicted using the AAE. Following Botero et al. [60], optical band gaps were derived for a direct allowed transition (r = ½), and evaluated in the 440-540 nm wavelength interval. In the analysis, the value of the optical band gap energy (E_g) was determined by plotting $(b_{abs} * hv)^{1/r}$ on the y-axis and hv (the photon energy) on the x-axis. E_g was then determined from extrapolating the linear fit to where it intersects with the y-axis. This energy corresponds to the optical band gap. A graphical example of the analysis is shown in Figure 19.

To reduce contribution to b_{abs} from non-refractory components, the normalized absorption curves that were used to derive optical band gaps were calculated from the AAEs evaluated at the three longest aethalometer wavelengths (660, 880, and 950 nm).

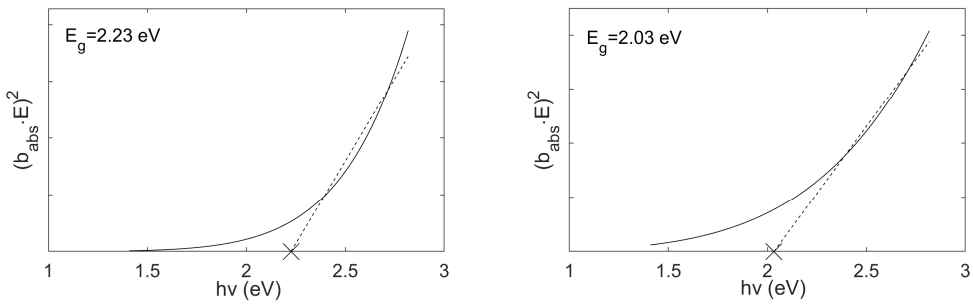

Figure 19. Optical band gap analysis for soot with two different AAEs. *hv*=E denote the photon energy and b_{abs} is the absorption coefficient. E_g is the optical band gap energy.

3.2.3 Thermal-optical carbon analysis

Thermal-optical carbon analysis, often referred to as OC/EC analysis, is a reference technique for determining the mass of refractory carbonaceous material. In the thermal-optical carbon analysis, carbon mass is divided into sub-classes based on their thermal volatility and oxidation reactivity with O_2. Organic carbon (OC) is defined by the carbon mass evaporated from the aerosol sample during temperature ramping in an inert Helium atmosphere. Elemental carbon (EC) is defined by the necessity to remove the material in an oxidizing atmosphere at high temperatures. Table 2 shows the EUSAAR2 analysis procedure [88] that was used in the analysis of all samples related to this thesis.

Table 2.
EUSAAR_2 protocol for the thermal-optical carbon analysis [88].

	OC Inert He gas				**EC He gas mixed with 2% O_2**			
	OC1	OC2	OC3	OC4	EC1	EC2	EC3	EC4
Temperature (°C)	200	300	450	650	500	550	700	850
Time (s)	120	150	180	180	120	120	70	80

3.2.4 Soot nanostructure characterization using high-resolution transmission electron microscopy (HRTEM)

Soot nanostructures were analyzed by HRTEM and images with sub-Ångström resolution of the soot nanostructure were acquired (Papers 3 & 4). A semi-automated image analysis was applied to characterize the size and curvature (the tortuosity) of carbon fringes. The analysis procedure and results are documented in [89-93], and a description of the procedure can additionally be found in the supplementary document of Paper 3. Similar methodologies are also described by others in the literature [93, 94].

3.2.5 Reactive oxygen species (ROS)

The diesel soot samples were collected on filters by a high volume sampler. The particles collected on the filters were extracted by sonication in methanol (Paper 5). The gravimetric mass extraction efficiency was larger than 85% for all samples. The ROS forming potential of the extracted diesel engine soot was assessed using the cell-free 2', 7' dichlorodihydrofluorescein diacetate ($DCFH_2$-DA) assay. The method has been described in detail in Jacobsen et al. [95] and Høgsberg et al. [96] and is especially sensitive to hydroxyl radicals, peroxyl, peroxynitrite, and nitric oxide [97]. It is considered to be one of the least specific ROS assay [98].

4 Results & Discussion

This chapter is divided into four sections: 4.1 Properties of immature and mature soot produced with the miniCAST flame soot generator; 4.2 Combustion conditions and soot properties for all studied sources; 4.3 Climate-relevant black or brown carbon soot particle characteristics; 4.4 ROS forming potential of diesel engine soot and implications for particle induced toxicity.

4.1 Immature and mature soot

Soot maturity is a description that originates from studies on how soot properties evolve in flames. Immature soot consists of the newly formed soot particles encountered shortly after soot inception in flames. Immature soot is characterized by amorphous structures and high H:C ratios. As a soot particle passes through the hot flame, it is subject to continuous surface growth reactions, a carbonization process, and a simultaneous ordering of the carbon nanostructure. It is also subject to oxidation, mainly by O, O_2, and OH. This evolution is described as a soot maturation process. Mature soot is found some time after the formation of incipient soot particles and is characterized by ordered (graphitic-like) nanostructures with typical BC absorption characteristics.

4.1.1 Characteristics of the miniCAST soot emissions

Increasing the miniCAST N_2 mixing gas flow resulted in a transition from mature to immature soot characteristics. This was manifested in the soot nanostructure by less structural order, increased tortuosity, and significantly shorter fringe lengths (Paper 3). Figure 20 shows representative high-resolution transmission electron microscopy (HRTEM) images and the geometric mean fringe length and tortuosity derived from the HRTEM analysis. At the same time, while the mature soot was mainly composed of elemental carbon (EC) and smaller amounts of organic carbon (OC), the immature soot was characterized by decreasing elemental carbon (EC) particle fractions and increasing fractions of organic carbon (OC) (Paper 2). A substantial fraction of the OC

for the less mature soot particles (OP 5-7) was associated with low volatility OC (mainly OC4 evaporated at a temperature of 650°C in an inert He atmosphere) and carbonaceous material defined as pyrolytic carbon (PC) by the thermal-optical carbon analysis.

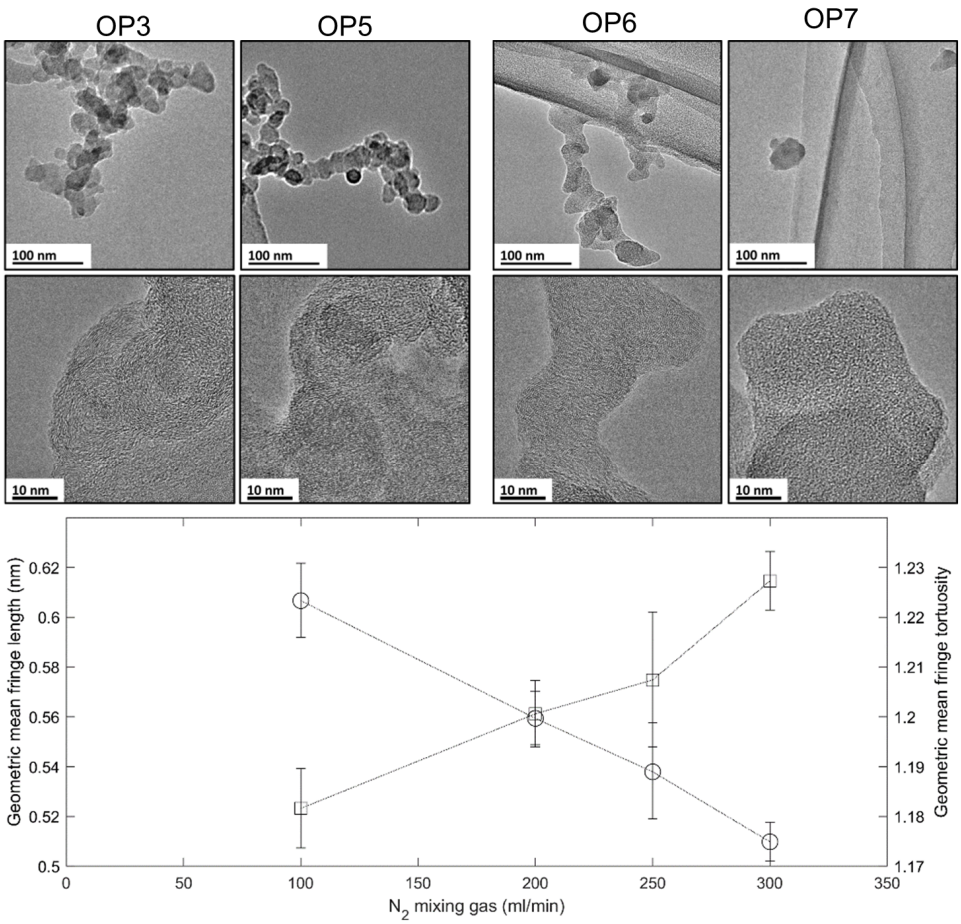

Figure 20. Top: high-resolution transmission electron microscopy (HRTEM) images of MiniCAST soot. **Bottom**: geometric mean fringe lengths (**circles**) and fringe tortuosity (**squares**) derived from the HRTEM analysis of MiniCAST soot. OP3, OP5, OP6, and OP7 correspond to 100, 200, 250, and 300 ml/min of N_2 mixing gas respectively. The errorbars show 95% confidence intervals of the estimated geometric means.

Immature soot was also related to elevated absorption Ångström exponents (AAE) and brown carbon (BrC) absorption (Paper 2). AAEs decreased but remained elevated, much higher than 1, upon conditioning of the aerosol (in the aerosol phase) at 250°C and 500°C for 5-10 seconds (Figure 21, top graph). In Paper 2 a connection was identified between the BrC light absorption characteristics and refractory organics that

did not evaporate in a ceramic tube furnace at 500°C. The bottom graph of Figure 21 shows that refractory OC (defined as OC4+PC) in relation to EC increased with miniCAST N_2 mixing gas. The major fraction of refractory OC was present also after treating the aerosol in the ceramic tube furnace at 500°C. Figure 21 demonstrates a very similar behavior of the refractory OC fraction and AAE with increased N_2 mixing gas and with thermal conditioning.

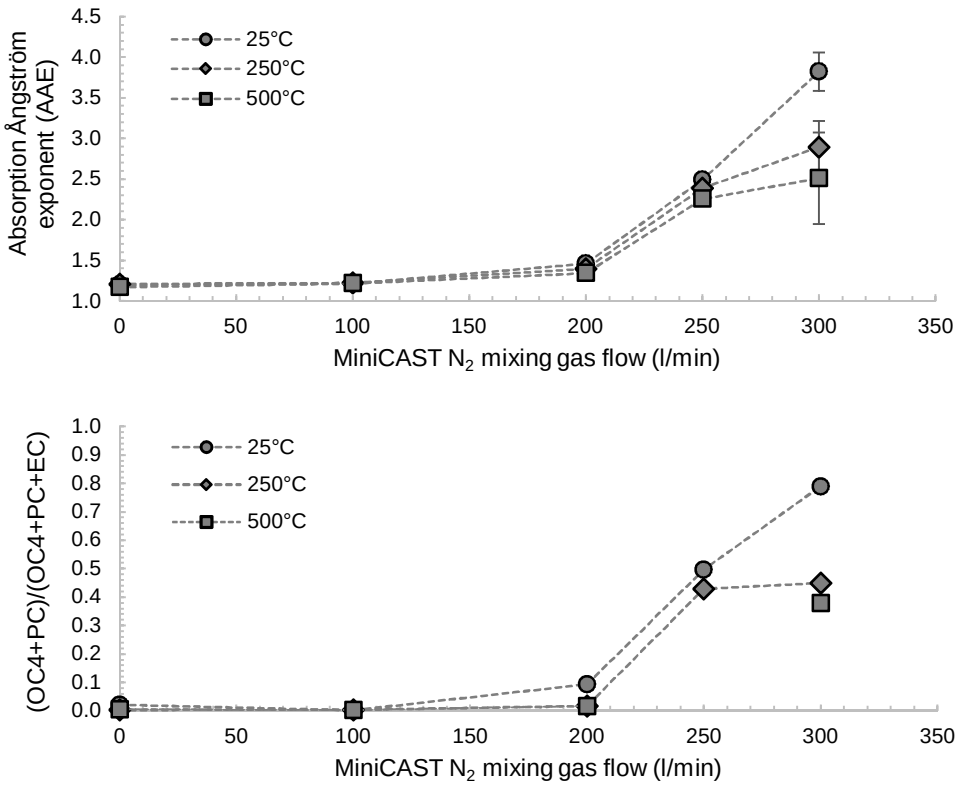

Figure 21. Top: MiniCAST N_2 mixing gas flow versus absorption Ångström exponents derived from in-situ laser extinction measurements at wavelengths from 405, 650, 850, and 1064 nm (paper 2). **Bottom**: MiniCAST N_2 mixing gas flow versus versus the EC fraction of refractory OC and EC. Refractory OC was defined as the sum of OC4 and PC.

4.1.2 SP-AMS analysis of immature and mature miniCAST soot

The thermal-optical carbon analysis indicated a substantial difference in the composition of immature and mature soot. This difference was also clearly demonstrated in the aerosol mass spectra. The representative non-refractory aerosol mass spectra of mature (OP3) and immature (OP7) soot are shown in Figure 22. The

non-refractory organic aerosol of the mature soot was mainly composed of low mass fragment species (<120 Da) typical for organic material dominated by aliphatic compounds. The immature soot was more aromatic in its character, with a substantial signal from low mass fragments with low (≤1) H:C ratios and larger (200-400 Da) semi-volatile polycyclic aromatic hydrocarbons (PAHs).

The refractory soot material is mainly composed of carbon. This material is detected in the SP-AMS as signals from positively charged carbon clusters (C_x^+). Some contribution to the C_x^+ signal is also observed in the non-refractory organic mass spectra shown in Figure 22. This signal originates from the fragmentation of organic molecules to C_1^+ and is not related to refractory material. For the exhaust studies included in this thesis, the non-refractory organic contribution to C_1^+ was negligible in comparison to the contribution from refractory material.

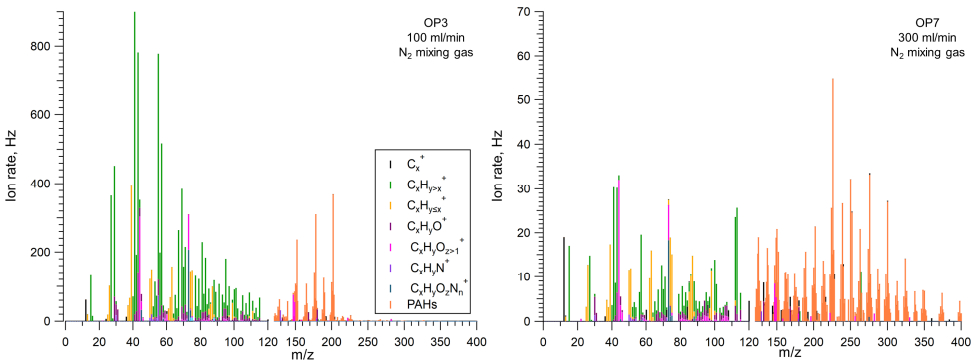

Figure 22. Non-refractory (no laser vaporizer) organic aerosol mass spectra. **Left:** mature soot (OP3). **Right:** immature soot (OP7). The mature soot shows organic fragments typically assigned to aliphatic components. The immature soot shows a strong contribution from polycyclic aromatic hydrocarbons (PAHs) and low mass fragments with more carbon atoms than hydrogen atoms that are typically assigned to aromatic or cyclic aliphatic compounds. These mass spectra resemble those obtained for soot extracted from the diesel cylinder in Paper 1. The mature OP3 soot mass spectra is similar to the mass spectra for soot extracted late in the combustion cycle, while the immature OP7 is more reminicent of that observed for soot extracted early in the cycle. For singly charged clusters the mass-to-charge ratio (m/z) is identical to the molecular mass (Da).

The chemical bonding environment of refractory carbonaceous materials influences the carbon cluster distributions observed in the SP-AMS mass spectra [76, 82]. Mature soot with typical (refractory) BC properties almost exclusively produces signals from C_{1-5}^+ clusters. These are referred to as “lowcarbon clusters”. The common method to estimate refractory BC (rBC) involves calibration of the lowcarbon signal intensity to a known reference material and particle mass. Larger carbon clusters ($C_{>6}^+$) in aerosol mass spectra have been associated by others with fullerene-containing engineered nanoparticles, amorphous carbon, biomass burning, and certain laboratory flames [76, 82, 99]. Variations in the carbon cluster distribution have previously been hypothesized

to correspond to different bonding environments of the refractory carbonaceous material [76, 82, 99], and the large carbons have been hypothesized to originate from soot that is not fully mature or is incompletely graphitized [82]. Other laser-based aerosol mass spectrometry techniques have also detected fullerene-like carbon clusters in the analysis of immature soot particles extracted from a premixed ethylene/air flame [100], and of soot particles from a miniCAST flame soot generator that was operated similarly to the OP6 settings presented in Table 1 [101]. In Papers 2 and 3, we showed the presence of large carbons in SP-AMS mass spectra for immature soot, and their almost complete absence for the mature soot produced by the miniCAST. The SP-AMS refractory carbon cluster distributions of mature (OP3) and immature (OP7) miniCAST soot are shown in Figure 23.

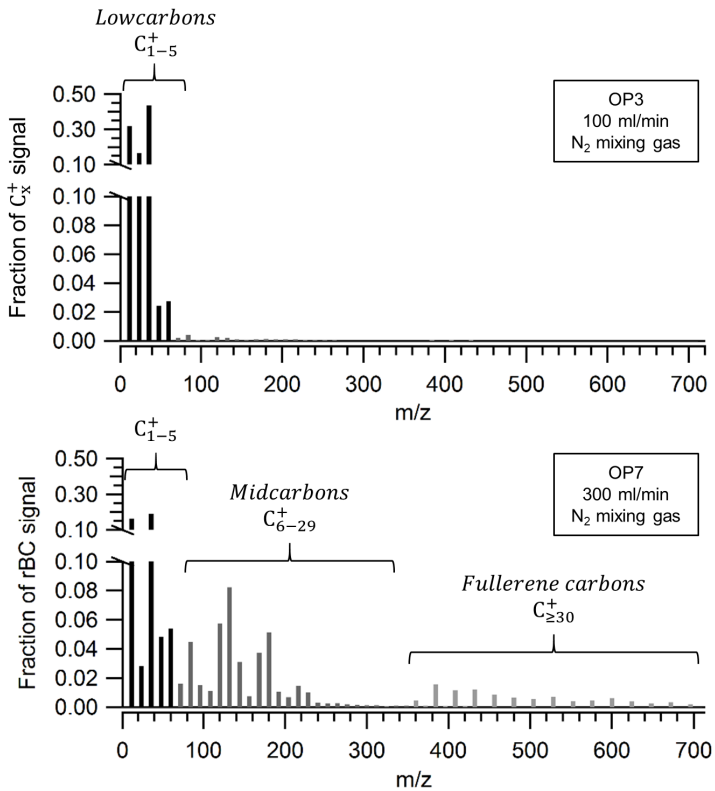

Figure 23. SP-AMS refractory carbon cluster distributions for mature soot (OP3, **top**) and immature soot (OP7, **bottom**) from the miniCAST soot generator. Lowcarbons C^+_{1-5} dominate the mature OP3 sample. The immature OP7 soot has strong signals from midcarbons (C^+_{6-29}) and fullerene carbons ($C^+_{\geq 30}$).

Paper 1 shows that large carbons decreased with combustion time inside the cylinder of a heavy-duty diesel engine and it was hypothesized that the large carbon clusters were

related to curved (high tortuosity) C5-containing nanostructures. In Paper 3 we tested the hypothesis presented in Paper 1 and used the HRTEM analysis of fringe length and tortuosity (curvature) as the benchmark for evaluation against the SP-AMS refractory carbon cluster distributions. The evaluation showed that the ratio of large carbons to lowcarbons ($C^+_{\geq 6}/C^+_{1-5}$) was linearly correlated to both the geometric mean fringe length and tortuosity. However, only the correlation to fringe length was statistically significant. This suggested that refractory large carbons may not necessarily be directly related to the inclusion of five-membered aromatic rings, as was hypothesized in Paper 1, but to the size of aromatic clusters.

To parameterize changes in the SP-AMS refractory carbon cluster distribution, the C^+_{3X} parameter was introduced in Paper 4 (and in Eq. 4 of this thesis). A comparison of the C^+_{3X} parameter and fringe lengths (HRTEM) for miniCAST soot is presented in Figure 24. The miniCAST data shows that C^+_{3X} was correlated to the geometric mean fringe length (r=0.94). Similar to the results in Paper 3, the C^+_{3X} parameter was also correlated to tortuosity (r=0.88). Aerosol mass spectra were generally obtained with 10 to 20 seconds time-resolution. The analysis of SP-AMS refractory carbon cluster distributions could therefore enable highly time-resolved studies of changes in soot nanostructures, and be significantly less laborious to the off-line HRTEM analysis.

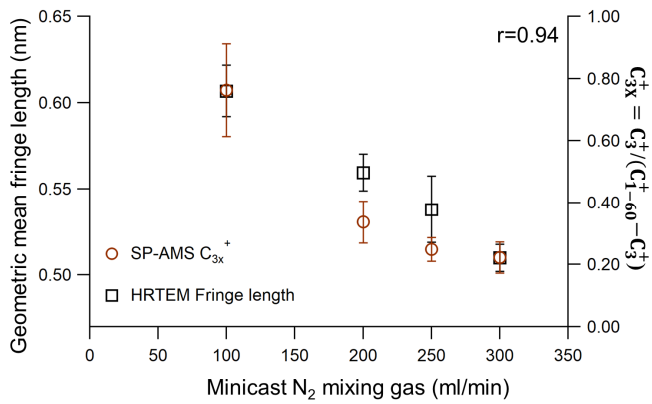

Figure 24. The geometric mean fringe lengths and SP-AMS C^+_{3X} (defined for C^+_{1-60}) for miniCAST soot. The Pearson correlation was r=0.94 for the miniCAST soot. Errorbars show 95% confidence interval for the geometric mean fringe lengths, and standard error of the mean for the SP-AMS C^+_{3X}.

4.2 Combustion conditions and soot properties

The previous section (4.1) showed how soot composition, carbon nanostructures, aerosol mass spectra, and light absorption properties were distinctively different for immature and mature soot from the miniCAST soot generator. This section describes in-cylinder diesel engine soot properties and soot emissions from: a diesel engine, the miniCAST, and four biomass based cook stoves. Diesel engine combustion temperatures were lowered by adding exhaust gas recirculation (EGR), and the fossil diesel fuel was replaced by a renewable rapeseed methyl ester (RME) biodiesel and a renewable hydrotreated vegetable oil (HVO) fuel. The miniCAST combustion conditions were altered by premixing the propane gas with N_2 and reducing the oxidation air flow. The four biomass based cook stoves represent different designs and combustion conditions.

4.2.1 Soot processes and emissions from a heavy-duty diesel engine

Soot processes were studied inside the combustion cylinder of a heavy-duty diesel engine and presented in Paper 1. The soot processes were studied as a function of time in the combustion cycle and for three levels of exhaust gas recirculation (EGR). The EGR dilutes the engine intake air with (mainly) CO_2, which results in a lowering of the O_2 concentration and increased heat capacity of the gas mixture. EGR is therefore an effective technique to reduce combustion temperatures and the in-cylinder NO_x formation. The reduction in combustion temperatures is indirectly demonstrated in Figure 25 (bottom graph) as a strong decrease in NO_x emissions with increasing EGR (reduced intake O_2 concentration).

Figure 25 shows an overview of the diesel engine soot processes studied in Papers 1 and 5. In-cylinder soot formation occurred shortly after the start of combustion, reached a maximum, and decreased in the late combustion cycle (Figure 25, top graph). The initial phase, the soot formation phase, is the part of the combustion cycle in which soot concentrations increased. Conversely, the soot oxidation phase was defined as the part in which soot concentrations decreased after the in-cylinder peak soot concentration was reached. The in-cylinder peak soot concentration was found to be a strong function of EGR, and was heavily suppressed for reduced combustion temperatures and O_2 (increased EGR). However, the soot oxidation in the late combustion cycle was suppressed at a faster rate than the reduction in the soot formation. This resulted in increased BC emissions for reduced combustion temperatures at lower O_2 concentrations and low to medium amounts of EGR (shown in the lower graph of Figure 25). This effect has previously been shown in experiments

using optical engines (e.g., [74]). Increasing the EGR even further (intake O_2 <11%) reduced combustion temperatures and led to a sharp decay in BC emissions as a result of slow soot formation. BC emissions nearly vanished at the highest levels of EGR, close to stoichiometric diesel combustion (~8-9% intake O_2 concentration). This resulted in a characteristic "soot bump" shown in Figure 25, and a trade-off between BC and NOx emissions was found for all EGR levels except at low temperature combustion conditions. The intake O_2 intervals for which BC emissions were governed by soot formation or soot oxidation are qualitatively indicated in Figure 25.

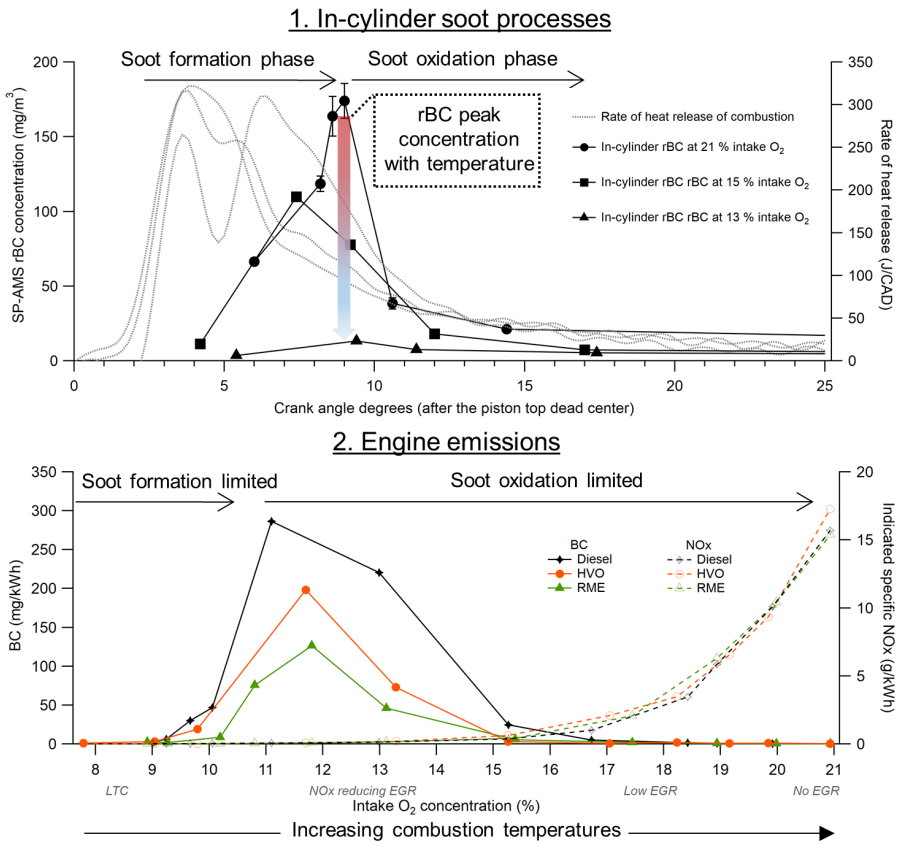

Figure 25. Top: Diesel engine in-cylinder soot processes and emissions. In-cylinder soot concentrations (rBC) and heat release rates. CA50, the crank angle at which 50% of the heat from combustion is released, was constant at ~7 CAD. The heat release curves can be identified by: two well defined peaks (21% O_2), two poorly defined peaks (15% O_2), and one peak (13% O_2). **Bottom:** Soot and NO_x emissions versus the intake O_2 concentration and for combustion with Swedish MK1 fossil diesel, a rapeseed methyl ester (RME) biodiesel, and a renewable hydrotreated vegetable oil (HVO) fuel. The different in-cylinder soot curves represent different intake O_2 concentrations for which the emissions can be compared in the bottom graph. The effect of reduced combustion temperatures on the in-cylinder peak soot concentration is indicated by the vertical arrow in the top figure. Fuel injection started a few milliseconds before the piston top dead center and combustion started shortly after the top dead center, at 0 crank angle degrees. The 50% of the total heat released from combustion occurred at ~5 crank angle degrees. Nearly all of the heat was released (i.e., combustion) prior to 20 crank angle degrees. Note that the exhaust gas recirculation (EGR) increases for decreasing intake O_2 concentration. Low temperature combustion (LTC) was defined at intake O_2 concentrations below ~10 %.

The highest levels of EGR represent low temperature combustion conditions. Low temperature combustion concepts include engine concepts to simultaneously achieve extremely low emissions of NO_x and particulate matter. Such engine concepts have great potential to reduce the need for expensive exhaust after treatment technologies. In the experiments conducted for this thesis, low temperature combustion conditions were primarily sought in order to study changes in soot properties. However, the results indicate that novel fuels which facilitate low temperature combustion conditions and have with low potential to form soot in the engine may be required for future combustion concepts that simultaneously aim to reduce the formation of particulate and gaseous emissions.

4.2.2 Fossil diesel versus renewable HVO and RME

In addition to combustion temperature, effects on particle emissions were studied for the substitution of conventional (fossil) diesel by renewable hydrotreated vegetable oil (HVO) and rapeseed methyl ester (RME) fuels (paper 5). The effect on BC emissions is indicated by the three curves shown in the bottom graph of Figure 25. Effects on the BC emissions induced by the renewable fuels were observed mainly for low-medium levels of EGR (at 9-15% intake O_2 concentration). The HVO fuel reduced the BC emissions, while the RME fuel reduced both BC and PAH emissions in comparison to combustion with the fossil diesel fuel. The reduction in PAHs for combustion with RME has been shown previously [102], and was in this study (Paper 5) demonstrated in both the AMS analysis and the off-line analysis with gas chromatography-mass spectrometry (GC-MS). The low effects observed for high intake O_2 concentrations may result from soot oxidation being the main mechanism controlling BC emissions at high combustion temperatures. It is plausible that effects related to the fuel propensity to form soot are more important at lower O_2 levels where soot emissions to a higher degree are governed by soot formation (and not by oxidation).

4.2.3 Soot characteristics for altered combustion temperatures in the miniCAST and the diesel engine

It was shown in Paper 1 how the soot inside the diesel engine combustion cylinder appeared immature shortly after ignition, and "matured" as combustion progressed. This increase in soot maturity was manifested by an increasing SP-AMS C_{3X}^{+}, a decreasing PAH particle fraction, and a decrease in the AAE.

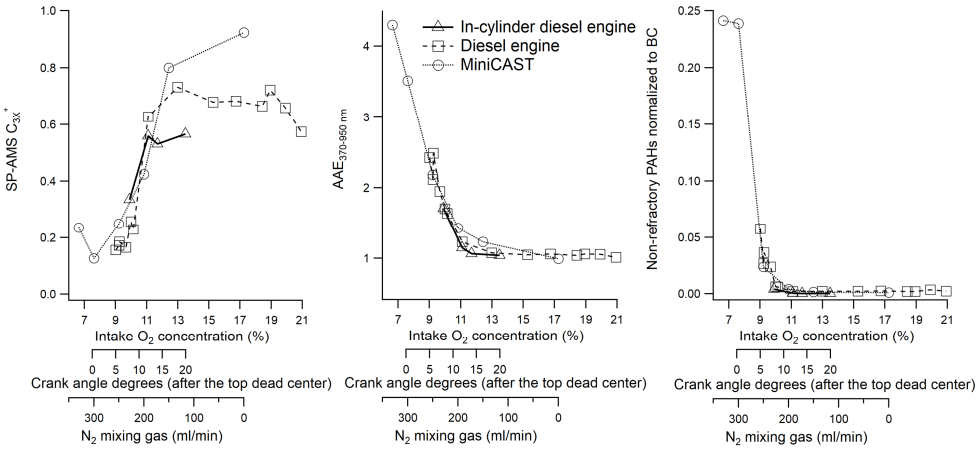

Figure 26. Soot properties in the in-cylinder diesel engine (fossil diesel), the diesel exhaust (fossil diesel), and MiniCAST (propane), and the change in SP-AMS C_{3X}^+ (**left**), $AAE_{370\text{-}950nm}$ (**middle**), and non-refractory PAHs normalized to BC (**right**) with increasing time in the cylinder or combustion temperature. The x-axes are identical for all three figures but have been scaled to qualitatively match the trend in $AAE_{370\text{-}950nm}$ for the three different processes.

Figure 26 shows a qualitative overview of the change in SP-AMS C_{3X}^+, $AAE_{370\text{-}950nm}$, and non-refractory PAHs normalized to BC for increasing time in the cylinder, decreasing N_2 dilution in the miniCAST, and increasing intake O_2 in the diesel engine. The change in soot properties with increasing combustion temperatures (i.e., increased intake O_2 concentration in the diesel engine or lowered addition of N_2 in the miniCAST) was strikingly similar to the observed in-cylinder soot evolution. Higher combustion temperatures resulted in a reduced fraction of non-refractory PAHs, a reduced large carbon signal in the SP-AMS (lower C_{3X}^+ values), and a reduced AAE. In addition, higher combustion temperatures were associated with refractory carbonaceous soot material that had longer fringe lengths (nanostructures) and were to a higher degree composed of elemental carbon. The results therefore also suggest that the maturity of soot emissions increased when combustion temperatures were higher.

A more detailed overview of the PAH to BC ratio and refractory C_{3X}^+ parameter for the miniCAST and diesel engine emissions is shown in Figure 27, where these particle characteristics have been plotted versus the respective combustion parameters. In addition, effects on soot properties from the three different diesel-like fuels can be evaluated from the data presented in Figure 27. These results indicate that the effect on soot maturity (C_{3X}^+) from replacing the fossil diesel fuel with renewable RME or HVO was low. However, the RME fuel clearly demonstrates reduced PAH to BC ratios at combustion conditions corresponding to both the low and high intake O_2 concentrations.

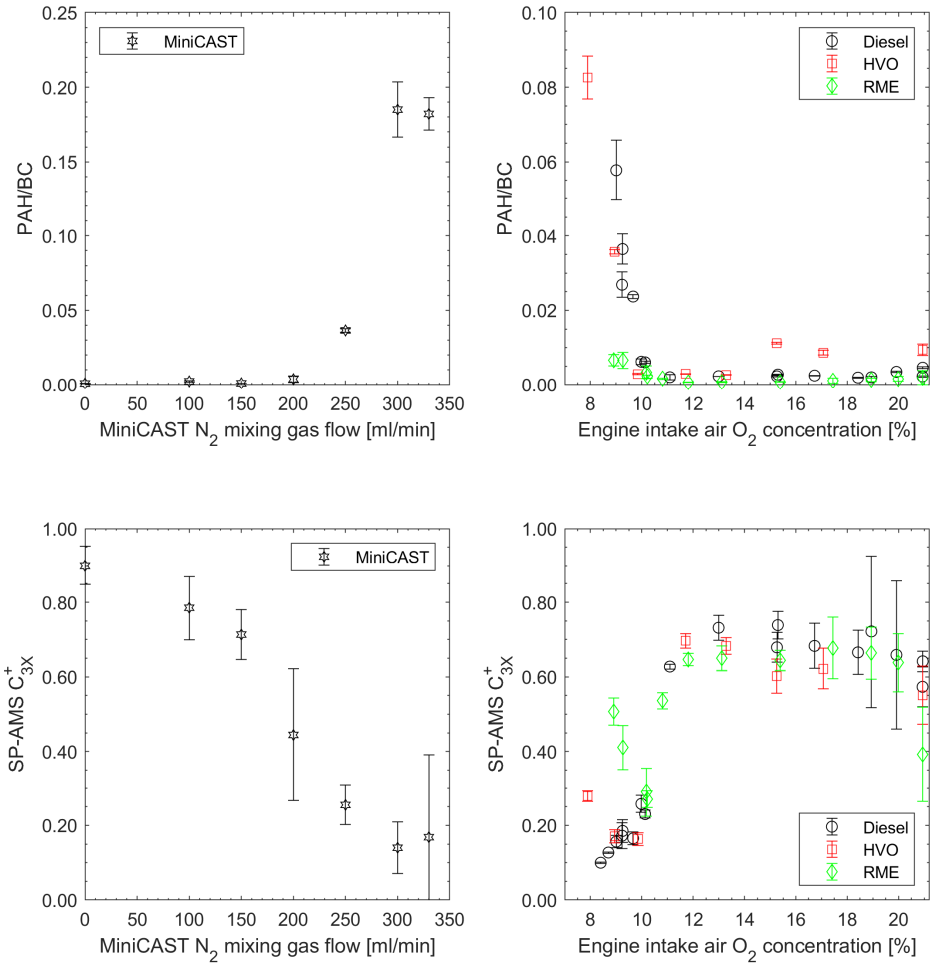

Figure 27. PAH concentrations normalized to black carbon (BC) and refractory C_{3X}^{+} for miniCAST soot (**left**) and diesel engine emissions (**right**). The diesel engine in-cylinder combustion temperatures decrease with decreasing engine intake air O_2 concentrations (higher EGR). Increasing miniCAST N_2 mixing gas reduces the combustion temperatures and results in immature soot characteristics. The miniCAST settings 0, 100, 150, 200, 250, 300, 330 N_2 (ml/min) correspond to operation points OP1, OP3, OP4, OP5, OP6, OP7, OP8 respectively. The miniCAST data was sampled in 2015 and 2017, and the displayed values represent mean values and pooled standard errors of the mean of 1 measurement conducted in 2015 and three measurements conducted in 2017. The spread in miniCAST data thus reflects variations in the burner, the instrument variability, and the different experimental set-ups and the aerosol dilution conditions.

4.2.4 HRTEM fringe lengths and SP-AMS C_{3X}^{+}

Figure 28 shows the SP-AMS C_{3X}^{+} parameter versus the geometric mean fringe lengths (HRTEM) derived for both the miniCAST and the diesel soot. This evaluation suggests a linear relation between refractory C_{3X}^{+} and fringe lengths in the evaluated interval also with respect to different measurement series. It should be noted that the linear

correlations between C_{3X}^{+} and fringe lengths were much stronger when assessing the experiments individually (miniCAST: R^2=0.88; diesel: R^2=0.98). This suggests that instrument tuning can have influenced the relative values of the C_{3X}^{+} parameter. Nonetheless, this supports the previous conclusion in section 4.1 that refractory carbon cluster distributions which can be obtained with aerosol mass spectrometry relate directly to the chemical bonding environment and size of refractory aromatic structures in soot. For future studies, it can be instrumental to calibrate the C_{3X}^{+} response using one or several reference particles.

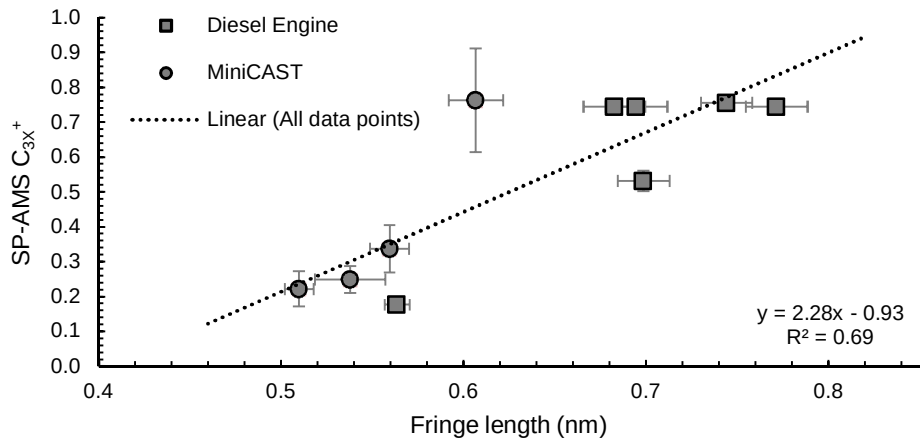

Figure 28. Evaluation of the relation between refractory C_{3X}^{+} (SP-AMS) and fringe length (HRTEM) for miniCAST soot (100, 200, 250, and 300 ml/min N_2 mixing gas) and diesel soot (Diesel 9.6% O_2, 13% O_2, 17% O_2, and HVO and RME at 13% O_2). Data represent mean C_{3X}^{+} and geometric mean fringe lengths derived from the distribution of evaluated fringes. Errorbars represent standard error of the mean (C_{3X}^{+}) and 95% confidence interval for the geometric mean (fringe lengths).

4.2.5 Soot characteristics of biomass based cook stove emissions

Results were also obtained of emissions from four biomass based cook stoves originating from Sub-Saharan Africa. Three of the cook stoves are shown in Figure 29. These cook stoves represent traditional and modern technologies and exhibit very different soot emission characteristics. Soot emissions from the 3-stone fire and rocket stove, the technologically least advanced cook stoves, had the highest PAH to BC ratios and lowest SP-AMS C_{3X}^{+} values when combustion emissions were averaged to a full (modified) water boiling test (Figure 29, top). The average emissions from the natural draft (ND) gasifier stove had slightly higher PAH to BC ratios compared to the forced draft (FD) gasifier stove, but had a C_{3X}^{+} value comparable to both the 3-stone fire and rocket stove (<0.6). Therefore when comparing emissions that were averaged over the

full combustion cycle, the 3-stone fire, rocket stove, and ND gasifier stove produced less mature particles and higher PAH to BC ratios compared to the FD gasifier stove.

The initial low temperature pyrolysis of the ND gasifier stove (Figure 29, middle) had particle emissions characterized by very high PAH concentrations relative to BC. The low SP-AMS C_{3X}^{+} values for this combustion phase indicates that the emissions were additionally characterized by immature refractory soot components. The PAH concentration relative to BC decreased, and C_{3X}^{+} increased from the early flame phase to the late flame phase and burn out. This was interpreted as an increase in soot maturity from the start of combustion to the flaming phase and burn out. A similar observation was made for the transient emissions from the rocket stove when comparing fuel addition (i.e., addition of new wood sticks) versus the flaming phase (Figure 29, bottom). The rocket stove fuel addition was associated with emissions with high PAH to BC ratios (~0.2-0.3) and low C_{3X}^{+} values (~0.3). In comparison, the flaming phase had very low PAH to BC ratios (~0.04) and much higher C_{3X}^{+} values (~0.6). The results indicate that combustion can be improved and PAH emissions (normalized to BC) can be reduced in the low temperature pyrolysis phase by the addition of a fan in the FS gasifier stove.

The combustion in small biomass appliances such as cook stoves is unpredictable, and combustion conditions are much less defined in comparison to the miniCAST and the diesel engine. It is therefore difficult to directly relate emission properties to combustion temperatures. However, the qualitative agreement between these biomass combustion emissions and the miniCAST and diesel engine are clear. The emission characteristics described for the vastly different combustion sources in this chapter (miniCAST, diesel engine, cook stoves) thus suggest a strong relationship between the combustion temperature and properties of soot emission. Low temperature combustion conditions result in immature soot, while higher temperatures result in more mature soot characteristics. This generalized description is important for our understanding of how particle properties and combustion conditions connect to climate-relevant optical effects and the toxicity of combustion emissions. The two following sections (4.3 and 4.4) are devoted to these questions.

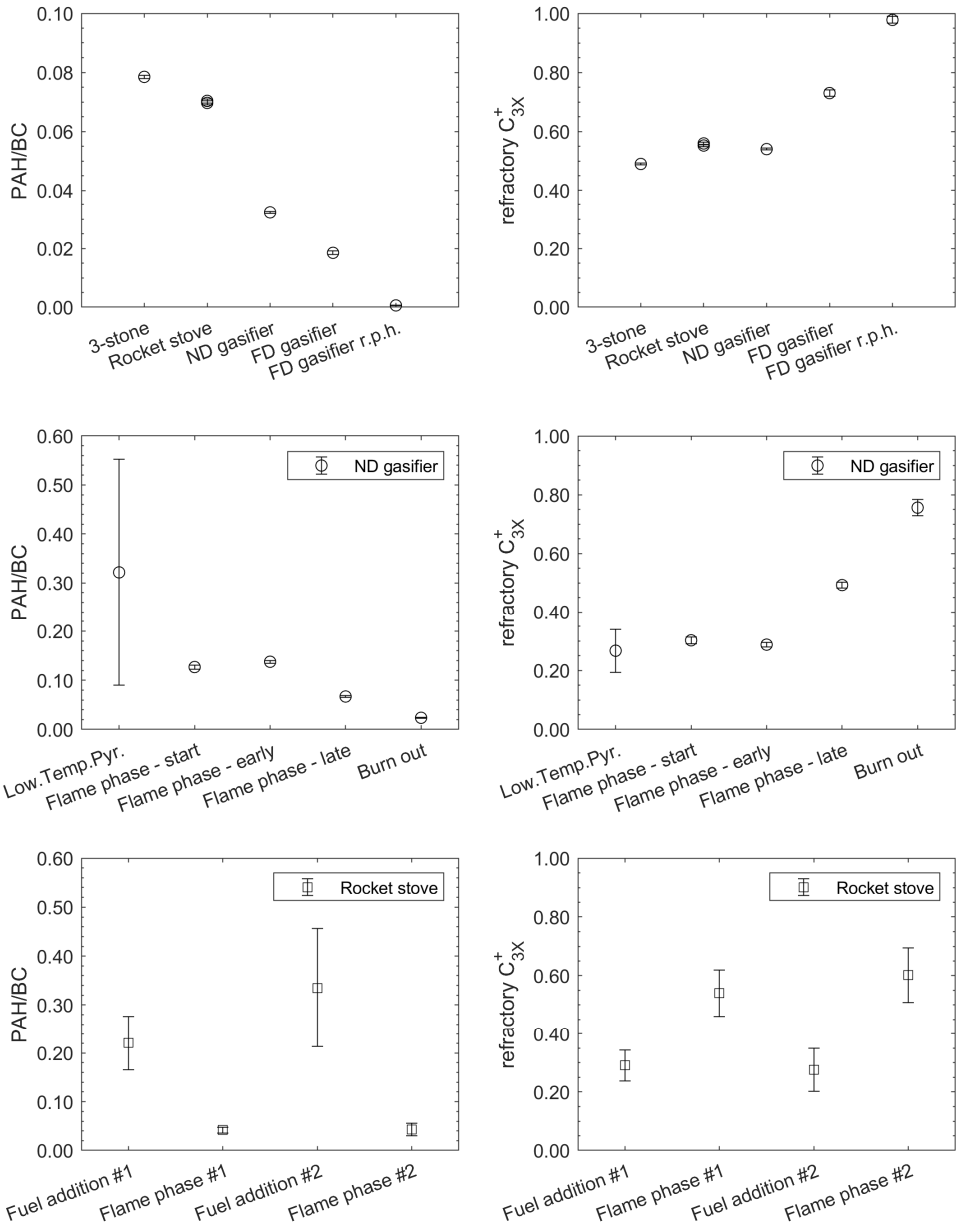

Figure 29. Top graphs: Cook stove emission PAH concentrations normalized to BC and refractory C_{3X}^{+} for 45-minute water boiling experiments and different cook stoves. The cook stoves used were a traditional 3-stone fire stove (wood sticks), a rocket stove (wood sticks), a natural draft wood pellets gasifier stove (ND gasifier), and a forced draft wood pellets gasifier stove (FD gasifier) at normal and reduced pot height (r.p.h). M**iddle graphs:** Averaged emission properties from short sequences during defined parts of the transient combustion cycle for the natural draft gasifier stove. **Bottom graphs: F**uel addition and flaming phases for the rocket stove.

4.3 Climate-relevant optical properties: from BrC to BC

The aromatic moieties in refractory soot components result in strong light absorption [24, 50]. This section discusses the absorption wavelength dependence and the BC or BrC nature of soot in relation to soot nanostructures and size of aromatic clusters (medium-range order), non-refractory PAHs, and refractory OC previously discussed in relation to combustion conditions (sections 4.1 & 4.2).

The absorption Ångström exponents (AAEs) were used to describe the wavelength dependence of light absorption. The AAEs that were observed for the miniCAST soot were similar to observations of the AAE as a function of height in a premixed ethylene/air flame (Paper 2 and [56]). The similarities in the AAEs for the flame and miniCAST are illustrated in Figure 30. In the flame presented by Simonsson et al. [56], the first visible soot appeared at approximately 4 mm height above the burner. The AAE was high (~4) for the immature soot particles shortly after soot inception, and decreased towards ~1 with increasing height above the burner. The miniCAST soot evolution of AAE with decreasing N_2 mixing gas was very similar and for which the AAEs ranged from ~4 to ~1.

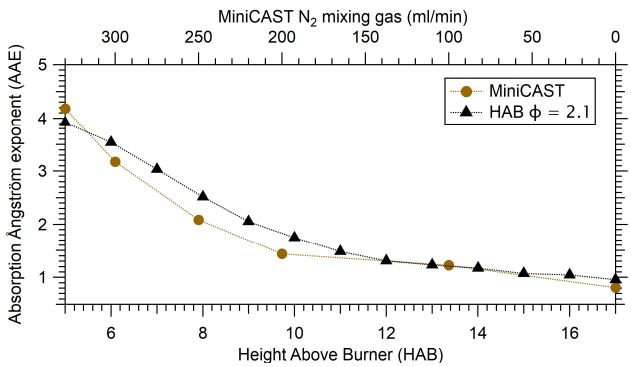

Figure 30. Absorption Ångström exponents (AAEs) for miniCAST soot emissions as a function of N_2 mixing gas and a rich premixed ethylene/air flame (Φ =2.1) as a function of height above the burner (HAB) [56]. The Ångström exponents for the miniCAST were evaluated in the 370-950 nm wavelength interval of the aethalometer, and in the 685-1064 nm interval for light extinction measurements in the HAB experiment.

4.3.1 The influence on AAE from reduced combustion temperatures and the removal of non-refractory soot components

There is a major knowledge gap concerning the assignment of BrC absorption characteristics to either refractory or non-refractory components. The previous sections (4.1 & 4.2) showed how combustion conditions can alter the size of refractory aromatic

structures and thus the medium-range order in emitted soot particles. The optical properties of soot particles also change when combustion temperatures vary. This was demonstrated in Papers 1, 2, and 4 in which it was shown how AAEs were consistently high (i.e., the particles had BrC characteristics) for the combustion conditions associated with immature soot.

Non-refractory PAHs with 4-7 aromatic rings have optical band gap energies corresponding to wavelengths between approximately 340-360 nm [62], and can contribute to absorption at shorter wavelengths. Papers 2 and 4 show that the thermal conditioning at 250°C and the removal of non-refractory OA and PAHs resulted in reduced AAEs (Figure 31). However, this reduction was minor even for the soot particles with strong BrC characteristics (AAE>2.5) from the miniCAST and diesel engine that was fueled with a non-aromatic HVO fuel (Figure 31).

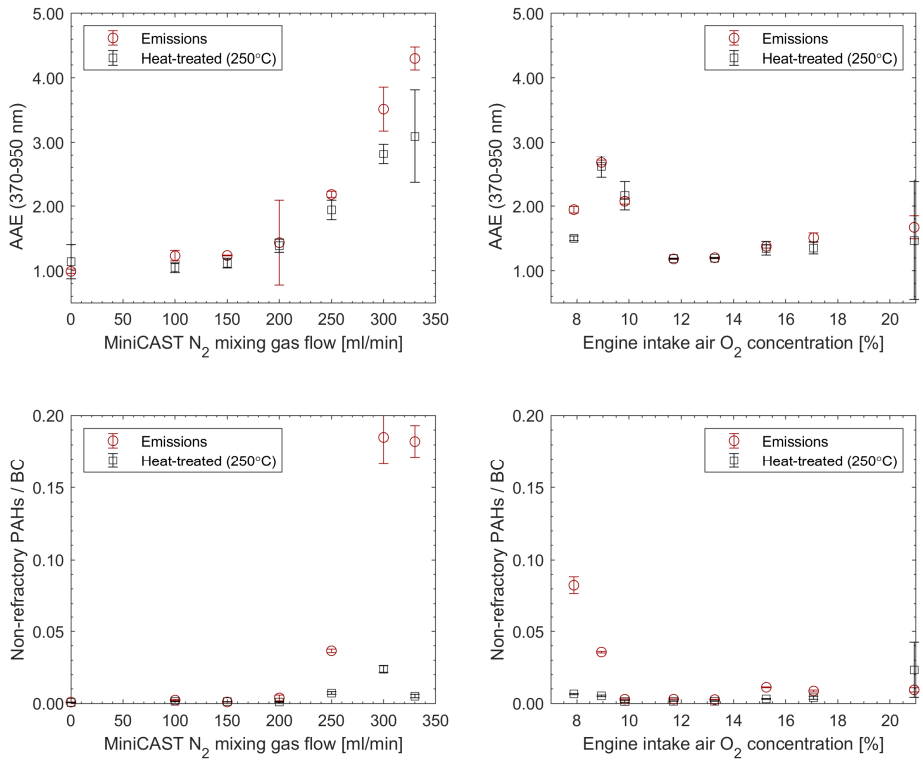

Figure 31. Top: Absorption Ångström exponents. **Bottom:** ratios of non-refractory PAHs to BC prior to and after heat-treating the aerosol in a thermodenuder at 250°C. **Left panels:** miniCAST emissions. **Right panels:** diesel engine soot emissions from combustion with HVO.

Non-refractory PAHs were removed by thermal conditioning of the aerosol at 250°C or 500°C for 5-10 seconds. The thermal-optical carbon (OC-EC) analysis showed that only minor pyrolytic carbon (increased light attenuation) was formed at temperatures as low as 250°C. The reduction in AAEs after thermal conditioning is therefore not likely explained by annealing and restructuring of the carbon nanostructures, but from evaporation of non-refractory organic soot components.

4.3.2 Relationships between AAE, particle composition, and soot nanostructures

The gradual ordering of the soot nanostructure associated with increasing combustion temperatures was accompanied by an evolution from BrC to BC absorption properties. This relation is displayed in Figure 32 (left) and suggests a power law dependence between fringe lengths and AAEs. The AAE versus the ratio of refractory EC to the sum of refractory organic carbon (OC4+PC) and EC is also shown in Figure 32 (right). The AAE decreased with increasing EC fraction. The data thus indicates that AAEs can also be related to the ratio of refractory OC to EC components of the soot, as was previously indicated in Figure 21. These Ångström exponents were evaluated in the 660-950 nm interval ($AAE_{660\text{-}950nm}$) in order to minimize absorption contribution from non-refractory light-absorbing PAHs (202-300 Da) that were observed in aerosol mass spectra.

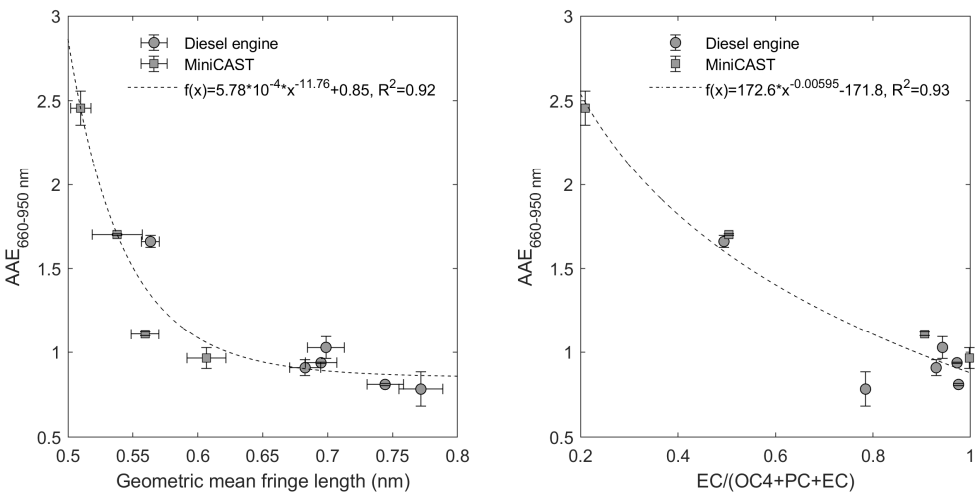

Figure 32. **Left:** The absorption Ångström exponent defined in the 660-950 nm interval ($AAE_{660\text{-}950nm}$) versus the geometric mean fringe length (HRTEM). **Right:** $AAE_{660\text{-}950nm}$ versus the elemental carbon (EC) fraction of refractory soot components (OC4+PC+EC) in the thermal-optical carbon analysis.

Using benzene or toluene as aromatic model fuels Saleh et al. [103] isolated BrC components by controlling the temperature of combustion in an oven, and found an exponential relationship between the imaginary refractive part of the refractive indices (*k*) and wavelength dependence. An increasing wavelength dependence (i.e., increased AAE) was associated with increasing particle volatility and a decreasing molecular mass of clusters in laser desorption/ionization mass spectrometry. The BrC components were found on the same continuum (exponential decay fit) with BC as the end point. From this Saleh et al. proposed a brown-black continuum in which BrC components are precursors to BC which do not complete their transformation to BC during the combustion process [103]. From similar experiments, Cheng et al. [104] showed that the fuel, the temperature, and air-to-fuel equivalence ratio are combustion variables that control the AAE and MAC of soot emissions. When increasing the equivalence ratio for a given fuel and temperature, the AAE of the emitted particles progressively increased from ~1 (BC) to more than 8. The increase in AAE were shifted to higher equivalence ratios when the temperature was increased by 100°C. The AAE was closely correlated to the ratio of EC and OC determined with thermal-optical carbon analysis. While ratios of EC and OC are excellent for evaluating data, the ability to identify the causal explanation of the BrC or BC nature of soot from these is limited.

As a result of the seemingly linear relationship between fringe lengths and SP-AMS refractory carbon cluster distributions (C_{3X}^{+}) shown in Figure 28, it was reasonable to suspect that the SP-AMS C_{3X}^{+} parameter would also be correlated to the AAE.

Figure 33 presents the SP-AMS C_{3X}^{+} parameter and AAEs from 125 measurements conducted in 2015-2017 on emissions from the miniCAST, from the diesel engine operating with different fuels, and from the cook stoves (the AAEs and C_{3X}^{+} of these sources are displayed separately in Figure 27 and Figure 29). Figure 33 shows that a lower C_{3X}^{+} was associated with higher AAEs across a range of soot sources and measurement campaigns. C_{3X}^{+} values lower than ≈ 0.15 were associated with AAEs higher than 2. A C_{3X}^{+} value larger than 0.5 indicated an AAE close to 1. The steep increase in the AAE implies that the predictive power of the SP-AMS C_{3X}^{+} parameter in relation to AAEs higher than 2 is low due to measurement uncertainties.

The relation between AAEs and C_{3X}^{+} is in qualitative agreement with the relation derived for geometric mean fringe lengths. The strong correlations between $AAE_{660\text{-}950nm}$ and both fringe lengths (Figure 32) and C_{3X}^{+} (Figure 33) may therefore reflect the causal relationship predicted by band gap theory between refractory soot components and elevated AAEs (BrC characteristics).

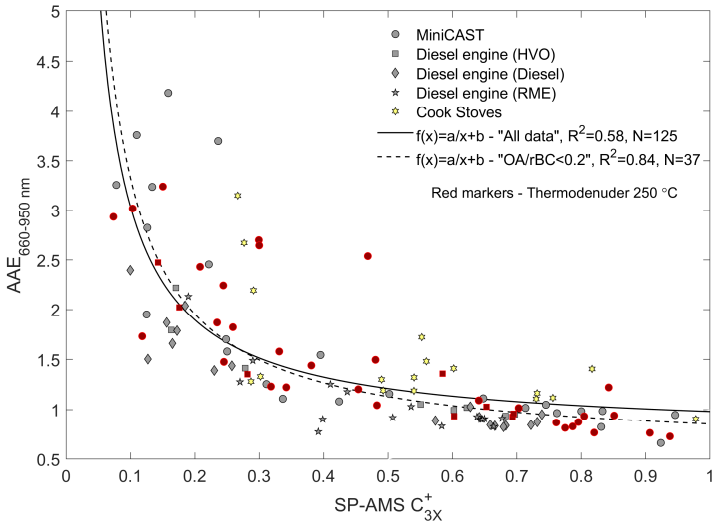

Figure 33. Absorption Ångström exponents (aethalometer) versus C_{3X}^{+} from the SP-AMS refractory carbon cluster distributions. The displayed data represent the same experiments (MiniCAST, Diesel engine, Cook stoves) previously described in **Figure 27** and **Figure 29**. Red markers display measurements performed after thermal conditioning in a thermodenuder (~250°C for 5-10 seconds). Fits of the form f(x)=a/x+b are shown for all data (solid line) and for measurements with OA to BC ratios lower than 0.2.

The fit was improved when only the data points with OA to BC ratios less than 0.2 were included (Figure 33). This suggests that for high AAEs, non-refractory organic components contributed to absorption at 660 nm. This is not well captured because C_{3X}^{+} does not include an expression for non-refractory aerosol components. The C_{3X}^{+} analysis is also limited by the SP-AMS' sensitivity to refractory carbon clusters. The refractory carbon cluster distribution depends on instrument tuning (e.g., laser power, section 3.2.1) and can show variation between measurement campaigns based simply on the instrument variability. Much of the variability shown in Figure 33 is lost when confining the analysis to a single series of measurements. This motivates the development of a (SP-AMS) calibration scheme and identification of a well-defined soot source to which C_{3X}^{+} may be normalized.

4.3.3 Optical band gaps and the relationship to soot maturity

Fringe lengths (Figure 32) are directly related to the size and molecular weight of the refractory aromatic units in the soot. The electronic band gap decreases for an increasing number of sp^2-bonded aromatic clusters [58, 62], and absorption and the AAEs are fundamentally related to the electronic band gap of these semi-conducting materials. Of importance for this research, optical band gap theory predicts that the

wavelength dependence decreases, and absorption efficiency increases with the size and number of sp^2-bonded aromatic rings [10, 24, 50, 58].

Optical band-gap energies were derived for the AAEs presented in Figure 33. Following Botero et al. [60], optical band gaps were derived by assuming a direct allowed transition (r=½), and were evaluated in the 440-540 nm interval. The band gap energies determined from AAEs (Figure 34, left) were between 1.73-2.3 eV. These energies are within the range that Botero et al. [60] found for immature to mature soot in a premixed flame.

Robertson and O'Reilly [58], and later Ferrari and Robertson [105], showed from theoretical considerations that the optical band gap of disordered amorphous carbon materials depends inversely on the number of aromatic rings and the size of sp^2-bonded clusters. Miller et al. [60, 61] derived a relation between the band gap energy and the number of aromatic rings (M) and conjugation length (L_a) in sp^2-bonded aromatic clusters (Eq. 6). This relationship was used as an independent evaluation of the hypothesis that the SP-AMS C_{3X}^{+} parameter was related to the internal soot nanostructure and the size of refractory aromatic units.

$$E_g^{opt} \approx \frac{5.8076}{M^{1/2}} + 0.5413 \approx \frac{1.4787}{L_a} + 0.5413 \quad \text{Eq. 6}$$

In Figure 34 (right), the SP-AMS C_{3X}^{+} was evaluated against the conjugation length of aromatic clusters estimated from the optical band gap energies and Eq. 6. The SP-AMS C_{3X}^{+} parameter shows a nearly linear correlation (R^2=0.71) to the sp^2-bonded cluster size. This comparison corroborates the previous comparison against the HRTEM analysis, and suggests that C_{3X}^{+} was related to the size of sp^2-bonded aromatic units of the refractory carbonaceous soot material. Therefore, the analysis of refractory carbon cluster distributions in aerosol mass spectra can be employed to study changes in the soot nanostructure, and the decrease or growth of refractory aromatic units.

These results have important implications for the interpretation of the BrC or BC absorption characteristics of immature and mature soot, respectively. The results presented in Figure 32 to Figure 34 show that an increase in the mean size of refractory aromatic units (sp^2-bonded cluster size) was correlated to a decrease in the optical band gap and AAE. This suggests that the AAEs of these combustion emissions were directly related to the size of sp^2-bonded aromatic clusters in the refractory soot material.

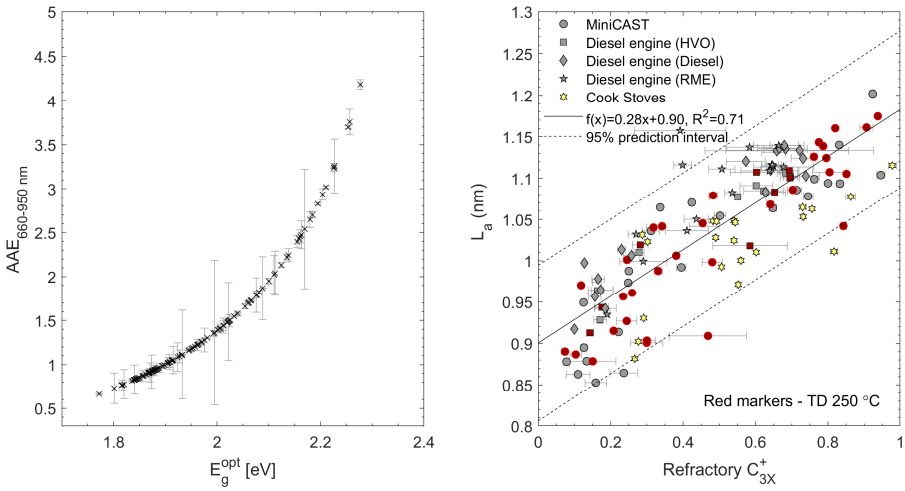

Figure 34. Left: optical band gap energies for absorption Ångström exponents (AAE) determined in the 660-950 nm interval ($AAE_{660\text{-}950nm}$). The relationship between optical band gap energy and AAE was best described by an exponential dependence (AAE = 0.002573*exp(3.135x) + 5.721e-14*exp(13.36x), R^2=1.00). **Right:** SP-AMS C_{3X}^+ values versus the conjugation length of sp^2-bonded aromatic clusters estimated from the optical band gap analysis and Eq. 6 [61].

Bond [26] applied the optical band gap framework to explain the variability in AAEs observed for light-absorbing carbonaceous particles emitted during the combustion of coal. Bond hypothesized that the MAC and AAE were controlled by the size of polycyclic aromatic clusters constituting the soot. This was supported by experiments showing an excellent correlation between measured absorption coefficients and absorption coefficients predicted from optical band-gap energies derived from knowledge of the absorption wavelength dependence [26]. The framework connecting absorption properties of soot particles to the size of polycyclic aromatic units may also apply to combustion related "tar balls" [106]. Tar balls that are characterized as BrC particles are emitted with combustion emissions, but likely follow a different formation route to the high-temperature soot formation.

A wealth of experimental evidence points toward a causal relationship between the optical properties of light-absorbing carbonaceous particles (soot) and combustion conditions [26, 42, 59-61, 103]. In-line with this literature, the results presented here suggest that light absorption by soot particles may follow a continuum predicted by the average band gap, and be determined by the size distribution of sp^2-bonded aromatic cluster. BC absorption is characterized by materials at the endpoint of this continuum, and composed of larger sp^2-bonded aromatic clusters in comparison to the immature soot. Theoretical predictions show that band gap energies decreases slower for larger cluster sizes [62], which may explain why mature soot with large cluster sizes (M>20) display similar BC light absorbing characteristics.

4.4 ROS forming potential of diesel engine soot and implications for particle induced toxicity

Diesel exhaust is classified as carcinogenic to humans [107] and induces inflammatory responses upon inhalation [108] or instillation [16, 67]. The oxidative stress induced by inflammation and the direct formation of reactive oxygen species (ROS) is important for the genotoxicity of diesel exhaust and particulate matter [15]. As such, both the direct ability of a particle to form ROS and the particle-induced inflammation are related to an increased risk of DNA damage. A fundamental question to be answered is what particle properties drive the ROS forming potential.

The literature strongly suggests that the acute pulmonary toxicity of ultrafine particles is proportional to the particulate surface area [16, 68]. Similarly, the direct ability of soot particles to form ROS has been connected to the surface area via the rate at which different particles consume ascorbate acid [16]. In addition to surface area, the surface chemistry modifies the induced in vivo inflammatory response [68]. This adds a second dimension related to the surface functionalization and inherent material properties.

This section is focused on the relationships found in Paper 5 between the diesel soot ROS forming potential, soot properties, combustion temperatures (increased EGR and reduced intake O_2 concentration), and renewable fuels.

4.4.1 ROS forming potential and specific surface area

The ROS forming potentials of five diesel exhaust samples and one carbon black sample (Printex 90) were evaluated in relation to the specific surface area of the soot particles (Figure 35). Printex 90 had a higher specific surface area in comparison to all the diesel particles and 2-15 times higher ROS forming potential per particle unit mass.

From the literature on the ROS forming potential of soot and carbon black particles, it was initially hypothesized that the diesel soot, when adjusted for the specific surface area, would have similar ROS forming potentials to Printex 90. In this case, the diesel soot would be distributed on the dashed line connecting Printex 90 and the origin in Figure 35. The diesel samples in this study do not display any clear trend with the estimated surface area.

Stoeger et al. [16] found that the oxidative potential determined from the depletion of ascorbate was comparatively low for diesel exhaust particles and flame soot with a high OC content. However, the thermal-optical carbon analysis data presented in Paper 5 shows clearly that both the diesel 10% O_2 and the 17% O_2 soot (the lowest and highest

ROS forming potentials) were characterized by a high OC content. Thus, inhibition by OC of the soot surface ROS forming potential was not a strong candidate for explaining the observed variation.

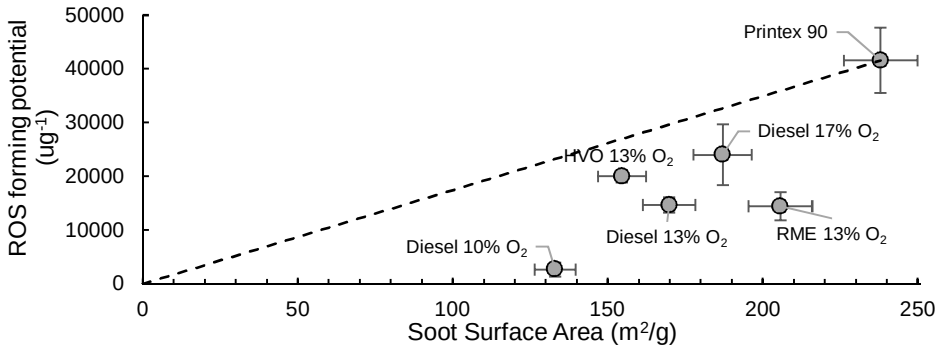

Figure 35. Reactive oxygen species (ROS) formation versus the estimated soot surface areas. The ROS forming potential was measured with the oxidation of 2',7'-dichlorofluorescin (DCFH) assay [15]. ROS errorbars represent standard errors of the mean. Surface area errorbars represent 95% confidence intervals approximated from the distribution of primary particle sizes. The surface area of Diesel 10% O_2 is highly uncertain due to poorly defined primary soot particles.

4.4.2 The ROS forming potential with respect to intake O_2 concentration, soot maturity, and oxygen-containing clusters in the SP-AMS

In addition to the specific surface area, the soot corresponds to samples collected at different EGR levels and intake O_2 concentrations, and represents soot with varying internal nanostructures (Figure 28).

The top graph of Figure 36 shows that the ROS forming potential was closely correlated (R^2=0.89) to the engine intake O_2 concentration. The immature soot (10% O_2) collected from the diesel engine had a significantly lower ROS forming potential than the more mature soot collected at a higher intake O_2 concentration. The ROS forming potential of the immature diesel soot at 10% intake O_2 concentration was only ~1/5 of the diesel soot at 13% intake O_2 concentration, and ~1/10 of that for the diesel soot at 17% intake O_2 concentration. The bottom graph of Figure 36 shows that the ROS formation per unit mass was correlated with increasing soot maturity, measured by the analysis of SP-AMS refractory carbon cluster distributions, and indicated by the linear regression (R^2=0.81). These results led to the hypothesis that soot surfaces in the first step generate more ROS as the soot matures. In the second step, the ROS forming potential increases as the soot surfaces become altered by surface oxidation.

X-ray photoelectron spectroscopy (XPS) is a surface-sensitive technique based on the photoelectric effect. Different molecular configurations give rise to different chemical

shifts in the energy levels of an atom, and the XPS method relies on the ability to detect these small variations in energy levels of core electrons (e.g., C1s). Müller et al. [38] used XPS and identified C-OH groups as major contributors to the surface oxygen content in diesel exhaust particles. In addition to these, surface oxygen for a number of different carbonaceous particle materials (including the diesel soot) was mainly attributed to functional groups of C=O and C-O-C.

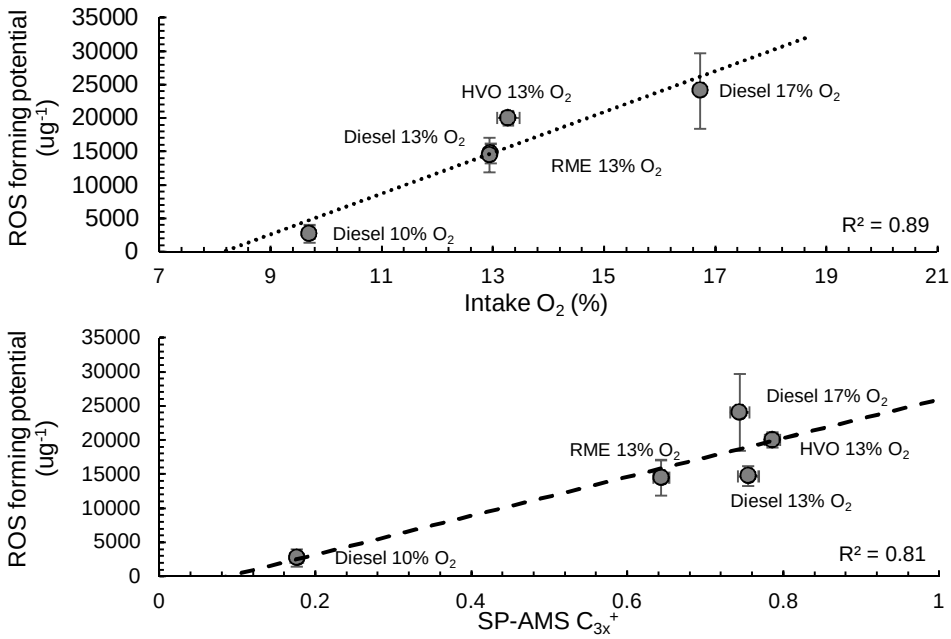

Figure 36. Top: ROS forming potential versus the engine intake O_2 concentration. Note that the Diesel and RME 13% O_2 samples lie on top of each other. **Bottom**: ROS forming potential versus soot maturity (SP-AMS C_{3x}^+).

4.4.3 Oxygen containing clusters in aerosol mass spectra

The SP-AMS mass spectra of soot particles frequently contain signals from oxygen-containing ion clusters. Refractory CO^+ and CO_2^+ are the most common oxygenated ions associated with refractory carbonaceous particles. Corbin et al. argued that the plausible origin of the CO_x^+ clusters was from oxygenated functional groups incorporated into the refractory structure of the carbonaceous particle material [99], thus occupying the reactive edge-site carbons. CO^+ and CO_2^+ may be observed in standard AMS mass spectra using only the thermal desorption at 600°C on a resistively heated tungsten vaporizer. These ions may therefore have contributions from non-refractory organic components as well as thermally less stable surface oxides. The literature on temperature-programmed desorption of activated carbons and

decomposition of oxygenated groups to CO and CO_2 [109] illustrates that carboxylic groups decompose mainly to CO_2 at relatively low temperatures (<450°C). At higher temperatures (>700°C), phenol, carbonyl, and quinone groups decompose mainly to CO.

An accurate SP-AMS analysis of CO^+ is prevented by the dominating air signal from N_2 at m/z 28. CO^+ was therefore not considered in this analysis. Figure 37 shows the ratio of refractory (laser vaporizer) CO_2^+/C_3^+ versus the specific surface area. There was a strong and linear correlation for the diesel engine samples with an intake O_2 concentration above 13% (R^2=0.99). The Diesel 10% O_2 sample does not show a similar dependence. The determination of the specific surface area for this sample was particularly challenging due to the fact that very few spherical primary particles could be observed. The divergence of this sample, that is representative of emissions from low temperature combustion, motivates further studies. A similar correlation to surface area (for samples collected at >13% O_2) was found for non-refractory (laser off) $CO_2^+ / \sum C_xH_yO_z^+$, indicating that the CO_2^+ clusters were likely related to thermally less stable surface functional groups. The correlation between CO_2^+/C_3^+ and surface area suggests that their related oxygen functional groups did not contribute to the observed variations in ROS forming potential.

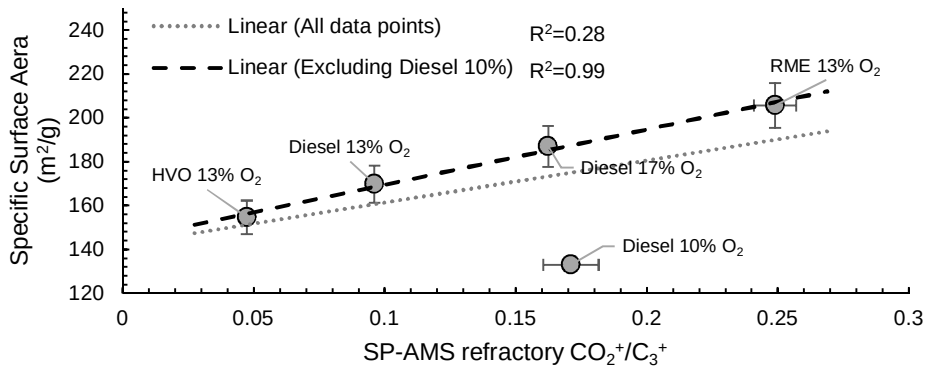

Figure 37. Correlation plot between the estimated particle specific surface area and SP-AMS refractory CO_2^+/C_3^+ (laser on) ratios. The diesel 10% O_2 soot surface area estimation is particularly uncertain due to the inability to identify clear primary particles in HRTEM images.

A number of $C_xO_y^+$ clusters were identified in aerosol mass spectra. Among these, $C_3O_2^+$ clusters were identified as refractory oxygen-containing clusters that only appeared during laser vaporization of the IR-absorbing carbonaceous particles. The signal intensity of these clusters were low, with $C_3O_2^+/C_3^+$ ratios less than 0.01. It is possible that these thermally stable oxygen functional groups also fragment to CO^+ upon

vaporization. For the diesel soot, $C_3O_2^+/C_3^+$ ratios increased with increasing intake O_2 concentration. This links increasing engine O_2 content and higher combustion temperatures to an increasing amount of thermally stable surface oxygen groups.

Increasing $C_3O_2^+/C_3^+$ ratios were linearly correlated (r=0.67) to an increasing ROS forming potential (Figure 38). However, the HVO 13% O_2 sample deviates considerably from the four other samples. The linear regression that excludes the HVO 13% O_2 sample included in Figure 38 suggests that the $C_3O_2^+/C_3^+$ ratio was closely related to the measured ROS forming potential (R^2=0.99). This result strengthens the second hypothesis that engine combustion temperatures and O_2 availability alters the soot's ROS forming potential by increasing the partial oxidation of soot surfaces. Specifically, the results presented in Figure 38 suggest that the diesel soot ROS forming potential was related to an increasing content of surface oxygen groups with high thermal stabilities, for example, carbonyls or quinones [109].

The oxidative potential can be high for the organic soot component [110]. However, in-vivo studies that have used animal models to assess the toxicity of different nanomaterials, including several types of carbon black particles, have linked the insoluble particle material to DNA damage and cancer [69, 111, 112]. Of further toxicological concern, the insoluble refractory soot particle components may reside in the lung for months after the exposure, and may additionally translocate to other organs such as the liver [111, 112]. Utilizing state-of-the-art techniques such as XPS, electron energy loss spectroscopy (EELS), or IR-spectroscopy in future research to determine the type of oxygen surface group may further advance our understanding of the ROS forming properties of soot particles and, additionally, aid in interpreting the oxygenated SP-AMS clusters.

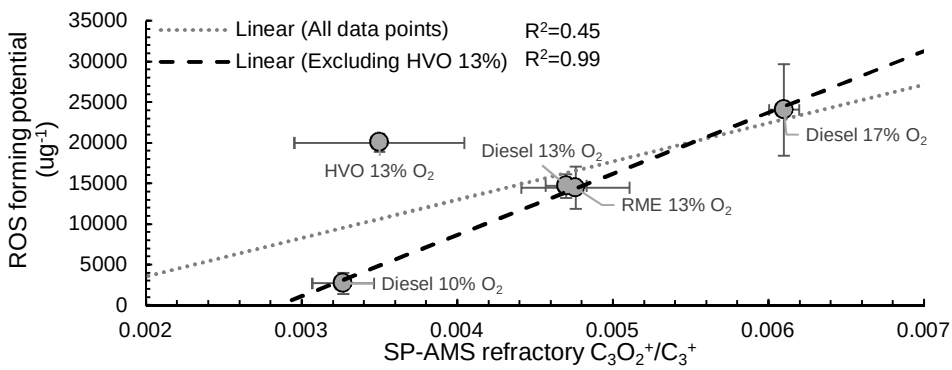

Figure 38. The ROS forming potential versus SP-AMS refractory $C_3O_2^+/C_3^+$ (laser on) ratios. Linear regressions are shown for all engine soot samples (grey dotted line, R^2=0.45) and for the three diesel and one RME samples after excluding and treating the HVO sample as an outlier (R^2=0.99). SP-AMS errorbars represent the standard errors.

5 Conclusions

The main results of the thesis research show that reducing the combustion temperatures alters the physicochemical properties of the emissions and results in less mature soot. The less mature soot was characterized by a higher content of non-refractory polycyclic aromatic hydrocarbons (PAHs) and soot nanostructures with shorter fringe lengths. This implies that the size of refractory aromatic units was reduced. These changes were associated with increased absorption Ångström exponents (AAEs) and a reduced ability of the soot to form reactive oxygen species (ROS) in vitro. The identified relationships connect reduced combustion temperatures to less mature soot, and to variations in climate-relevant optical properties and to properties that relate strongly to the toxicity of the soot.

Renewable HVO and RME showed a moderate potential for reduced engine out BC emissions when compared to combustion with fossil diesel. Combustion with RME also reduced the PAH emissions compared to diesel. The different fuels induced only small changes to the soot composition (non-refractory organics, PAHs, and refractory carbonaceous components). However, because of the reduced BC emissions from HVO and RME, some organic and metal components that originated from the lubrication oil were enriched in the particles with respect to BC (Paper 5). The differences in the ROS forming potential of the soot was low with respect to replacing the fossil diesel fuel with renewable RME or HVO. These results thus indicate that emissions from renewable fuels are of similar toxicological concern as the emissions from fossil diesel. However, lowered BC and PAH emissions from combustion with the renewable fuels can have positive effects on air quality, and may additionally be of interest in order to lessen, for example, the occupational exposure to diesel exhaust from machinery not equipped with diesel particulate filters.

When moderate levels of exhaust gas recirculation (EGR) were applied to the diesel engine, the lowered intake O_2 concentrations and combustion temperatures (indicated by reduced NO_x emissions) were associated with increased BC emissions. For these EGR levels, both the in-cylinder soot formation and soot oxidation were reduced. It was thus concluded that soot oxidation was the main parameter controlling BC emissions. BC emissions were reduced for high EGR levels and very low intake O_2

concentrations (<10%). It was suggested that this resulted from low soot formation rates at low temperature combustion conditions, as has previously been shown in studies on optical engines [113].

The C_{3X}^{+} parameter (Eq. 4) was defined to represent changes in the SP-AMS refractory carbon cluster distribution. C_{3X}^{+} was shown to correlate linearly with the mean fringe lengths derived from the HRTEM analysis of the soot nanostructure, and to the size of sp^2-bonded aromatic clusters derived from the optical band gap analysis. The results thus suggest that aerosol mass spectrometry and the analysis of refractory carbon cluster distributions can be employed as an indirect on-line measure of soot maturity.

The contribution to light absorption by non-refractory components increased with increasing AAE. For the least mature soot particles with the highest AAEs (>4), non-refractory organic aerosol components (e.g., PAHs) that evaporated in a thermodenuder at 250°C were estimated to be responsible for up to 55% of the total particle light absorption at 520 nm (Paper 4).

The immature soot, defined by short fringes and amorphous nanostructures, was characterized by AAEs significantly higher than 1 (BrC characteristics). An increase in soot maturity, defined by increasing fringe lengths, was accompanied by a gradual decrease in AAE and a transition from BrC to BC characteristics of the soot. Fringe lengths are proportional to the sp^2-bonded aromatic cluster size, and these results support a phenomenological model in which absorption by refractory soot components can be predicted by the size of refractory aromatic units.

The evolution in soot properties was similar with increased time in the diesel engine cylinder, a reduced intake O_2 concentration in the diesel engine, and increased N_2 dilution in the miniCAST. This was interpreted as a soot maturation process in which soot properties gradually evolve from immature soot (short fringe lengths and low C_{3X}^{+} values) rich in PAHs and with AAEs significantly higher than 1, to mature soot (longer fringe lengths and higher C_{3X}^{+} values) with low PAH to BC ratios and typical BC absorption (AAE~1). This suggests that higher combustion temperatures, in general, are associated with more mature soot emissions, and that the sources of immature soot emissions may be generalized to low temperature combustion processes. The soot reactivity towards oxidation is higher for less mature than for mature soot [12, 40]. The on-line identification of variations in soot maturity by means of aerosol mass spectrometry may help to identify combustion conditions and soot properties that facilitate the regeneration of diesel particulate filters, for example, and aid in the development of combustion strategies that reduce particle emissions.

The identification of immature soot properties from the analysis of SP-AMS carbon cluster distributions may be applied to source apportionment and can help identify

ambient aerosols with BrC components originating from combustion emissions. This can aid in deciphering the relative contribution from combustion emissions and other (secondary) sources to light absorption by BrC.

The ability of the diesel soot to form ROS (in vitro) was found to be correlated to the engine intake O_2 concentration. This result suggests that the combustion temperature and the in-cylinder soot oxidation are two important combustion parameters that influence particle properties related to its ability to form ROS. These parameters may therefore influence the toxicity and carcinogenicity of diesel soot emissions. The SP-AMS analysis of soot properties indicated that the ROS forming potential may increase in the first step due to more mature soot particles. In the second step, the ROS forming potential may increase due to additional oxygen-containing functional groups on soot surfaces.

6 Outlook

The interpretation of different refractory carbon cluster distributions in aerosol mass spectra from the SP-AMS requires further study. The origin of large carbon clusters and similarities in the seemingly invariant distribution of large carbon clusters is not yet understood. Laser annealing of carbon black particles can result in different nanostructures depending on their initial structure and sp^2/sp^3 ratio [114]. The results presented in this thesis indicate that a similar phenomenon may occur in the SP-AMS process, where laser heating can result in an annealing process followed by sublimation and detection of specific carbon clusters (i.e., fingerprints) in mass spectra. Thus, a hypothesis to address in future experiments is the possibility that laser heating results in an annealing process with predictable but distinctively different final structures and mass spectra for initial variations in the soot maturity.

Since aerosol mass spectrometry is well suited for experimental investigations as well as for long-term environmental monitoring, it is proposed that the methodology be incorporated into future studies to help interpret how different BrC particle sources contribute to the radiative forcing and the climate change.

Combustion emissions have profound implications for human health and climate change. Approximately 90% of the world's total energy supply derives from combustion processes [115]. It is thus likely that combustion will remain an important source of energy in the foreseeable future. Mitigating combustion emissions by exhaust aftertreatment systems or identifying less polluting combustion conditions must remain central to the sustainable development agenda. Identifying low-polluting and renewable fuels that are suitable for use in existing and modified combustion engines can be considered a primary objective for future research needs.

The number of diseases to date that have been linked to air pollution may only represent the top of an iceberg [3]. The identification of exposure-disease associations and the physicochemical particle properties that contribute to adverse health effects and radiative forcing of particulate air pollution is vital not only for an accurate description of these processes; it can also be a key instrument in deciphering the most relevant policy measures and in communicating the necessity to improve air quality. The work presented and described in this thesis can be further developed to aid evidence-based decisions and the development of more sustainable combustion solutions.

7 Acknowledgements

First of all I wish to thank my supervisor, Joakim Pagels, for his warm personality and never failing to give encouraging support. You have inspired me through scientific discussions, in the lab and during experiments when time seems to fly, and your enthusiasm is a constant source of motivation. The social aspects are just as important, and I am very grateful for the activities and non-work related discussions we have had.

Secondly, I wish to thank my co-supervisor Per-Erik Bengtsson who has, from the start, provided brilliant support in all parts related to the PhD studies, and not the least for motivating me to put on my running shoes. I equally wish to thank my co-supervisor Axel Eriksson for providing absolutely outstanding support on every detail regarding the SP-AMS and much more, and my co-supervisor Adam Kristensson for his excellent support and good mood.

The financial support from the Swedish Research Council VR and the Swedish Research Council FORMAS that enabled the research is acknowledged. Additionally, the Royal Physiographic Society of Lund and Carl Tryggers Stiftelse för Vetenskaplig Forskning are acknowledged for their financial contribution to new equipment.

The Volvo Group is acknowledged for supplying the material, and Jan Eismark and Timothy Benham at Chalmers University of Technology are acknowledged for their support with the fast sampling valve. Perstorp AB is acknowledged for supplying the renewable RME fuels.

My heartfelt gratitude to Anders Gudmundsson, Jakob Löndahl, Aneta Wierzbicka, Jenny Rissler, Christina Isaxon, Gerd Johansson, Mats Boghard, Roland Akselsson, and all the colleagues at the div. of Ergonomics and Aerosol Technology for making this into such a nice place, and for all your kind help and support throughout these years.

Thanks to Öivind Andersson, Martin Tunér, and all the support and inspiration from the colleagues at the dept. of energy sciences. Especially thanks to Sam Shamun, Yann Gallo, Menqin Shen and Maja Novakovic, for the great friends and good colleagues that you are.

Thanks to Birgitta Svenningsson, Thomas Kristensen, Johan Friberg, and all colleagues at the division of nuclear physics. I especially wish to thank Erik Swietlicki, it is very clear to me that the morning cup(s) of coffee cannot be overrated!

Thanks to Maria Messing and Calle Preger at the division of solid state physics, I am very happy that I have had a chance to work with you and socialize at conferences and in PhD courses.

The knowledge that is closely tied to the groups doing aerosol research in Lund is a large source of inspiration to me. I will always be grateful for the time spent as a PhD student at the division of Ergonomics and Aerosol Technology, and I can think of few other work places or occupations that are more rewarding.

I wish to acknowledge Christoffer Boman and Robert Lindgren at Umeå University, Tim Onasch and Ed Fortner at Aerodyne research Inc., Panu Karjalainen at Tampere University, Yilong Zhang and Sanghoon Kook at the University of New South Wales, Kirsten Kling at the Technical University of Denmark (DTU), and Ulla Vogel at The National Research Center for the Working Environment (NFA) in Denmark.

I wish to express my sincere gratitude to Eileen Deaner, for correcting so many of my mistakes, and you still show up with a big smile in your face!

I also wish to thank Carl-Erik Magnusson for being a constant source of inspiration during my undergraduate studies, and to thank my high school teachers Ulf Anderberg and Liselotte Andersson for stimulating the curiosity in me as a teenager.

Jonas Jakobsson, Christina Andersen, Stina Ausmeel, Karin Lovén, John Falk, and Yuliya Omelekhina, thank you for being such nice colleagues, the (how many?) coffee breaks, and for making the trips to conferences even more rewarding. Jonas et al., I wonder if you will help me figure out the p-value of this? Johan Martinsson, Moa Sporre, Patrik Nilsson, Erik Nordin, and Pontus Roldin thanks for all inspiring discussions on the work, the children, or the weather. Christian Svensson, you taught me can only be “good enough”, which was brilliant of you! Cerina Wittbom, thanks for being awesome and such a nice friend. Sandra Török thanks for all the good times in the lab, hours of adjusting the nuts to find all leaks in the set-up, having me wear funny colored protective glasses, and an unforgettable memory of a French pink DJ. Malin Alsved, I admire you immensely, you are an amazing person and I’m so glad we shared the same corridor over the past 4 years. The many and often unintentional discussions we’ve had outside your office and with a coffee in one hand are some of my favorite memories. Louise Gren, thanks for all the hard work in the lab, for being an outstanding colleague, and for being one of the nicest persons I have met. How does another 8 weeks in the lab sound?

All my love to Hans Gustavsson and his family, with you the time on the road before surf is just as good as the time in the water! Nothing is more refreshing than a sea at 0°C.

Thanks to my parents for all the support and for helping me develop an interest in the natural and technical sciences, and to my grandmother who at an age of 92 still goes off the beaten track just to climb a hill, you have all three inspired me throughout life. Thanks to Lisa, for the love and support in the very last minutes of writing this thesis. Finally I wish to thank my children, who always seem to find new ways to make life more exciting.

8 References

1. Dockery, D.W., et al., *An Association between Air Pollution and Mortality in Six U.S. Cities.* New England Journal of Medicine, 1993. 329(24): p. 1753-1759.
2. World Health Organization (WHO), *Ambient air pollution: a global assessment of exposure and burden of disease*. 2016, Geneva: WHO.
3. Landrigan, P.J., et al., *The Lancet Commission on pollution and health.* The Lancet, 2018. 391(10119): p. 462-512.
4. Lelieveld, J., et al., *Cardiovascular disease burden from ambient air pollution in Europe reassessed using novel hazard ratio functions.* European Heart Journal, 2019. 40(20): p. 1590-1596.
5. OECD International Energy Agency (IEA), Energy and Air Pollution: World Energy Outlook Special Report 2016. IEA, 2016.
6. Weagle, C.L., et al., *Global Sources of Fine Particulate Matter: Interpretation of PM2.5 Chemical Composition Observed by SPARTAN using a Global Chemical Transport Model.* Environmental Science & Technology, 2018. 52(20): p. 11670-11681.
7. International Agency for Research on Cancer (IARC), *IARC Monographs on the Evaluation of Carcinogenic Risks to Humans. Volume 109: Outdoor Air Pollution*. 2016: IARC Press Lyon, France.
8. Hallquist, M., et al., *The formation, properties and impact of secondary organic aerosol: current and emerging issues.* Atmospheric Chemistry and Physics, 2009. 9(14): p. 5155-5236.
9. European Environment Agency (EEA), *Air quality in Europe – 2018 report*, in *EEA Report No 12/2018*. 2018, European Environment Agency: Luxembourg.
10. Andreae, M.O. and A. Gelencsér, *Black carbon or brown carbon? The nature of light-absorbing carbonaceous aerosols.* Atmospheric Chemistry and Physics, 2006. 6(10): p. 3131-3148.
11. Huang, C.-H. and R.L. Vander Wal, *Partial premixing effects upon soot nanostructure.* Combustion and Flame, 2016. 168: p. 403-408.
12. Al-Qurashi, K. and A.L. Boehman, *Impact of exhaust gas recirculation (EGR) on the oxidative reactivity of diesel engine soot.* Combustion and Flame, 2008. 155(4): p. 675-695.
13. Matti Maricq, M., *Chemical characterization of particulate emissions from diesel engines: A review.* Journal of Aerosol Science, 2007. 38(11): p. 1079-1118.

14. Nel, A., et al., *Toxic Potential of Materials at the Nanolevel.* Science, 2006. 311(5761): p. 622-627.
15. Møller, P., et al., *Role of oxidative damage in toxicity of particulates.* Free Radical Research, 2010. 44(1): p. 1-46.
16. Stoeger, T., et al., *Deducing in Vivo Toxicity of Combustion-Derived Nanoparticles from a Cell-Free Oxidative Potency Assay and Metabolic Activation of Organic Compounds.* Environmental Health Perspectives, 2009. 117(1): p. 54-60.
17. Janssen, N.A.H., et al., *Black Carbon as an Additional Indicator of the Adverse Health Effects of Airborne Particles Compared with PM10 and PM2.5.* Environmental Health Perspectives, 2011. 119(12): p. 1691-1699.
18. Grahame, T.J., R. Klemm, and R.B. Schlesinger, *Public health and components of particulate matter: The changing assessment of black carbon.* Journal of the Air & Waste Management Association, 2014. 64(6): p. 620-660.
19. The Intergovernmental Panel on Climate Change (IPCC), *Climate Change 2013: The Physical Science Basis. Contribution of Working Group I to the Fifth Assessment Report of the Intergovernmental Panel on Climate Change*. 2013, Cambridge, United Kingdom and New York, NY, USA: Cambridge University Press. 1535.
20. Petzold, A., et al., *Recommendations for reporting "black carbon" measurements.* Atmospheric Chemistry and Physics, 2013. 13(16): p. 8365-8379.
21. Bond, T.C., et al., *Bounding the role of black carbon in the climate system: A scientific assessment.* Journal of Geophysical Research: Atmospheres, 2013. 118(11): p. 5380-5552.
22. Cui, X., et al., *Radiative absorption enhancement from coatings on black carbon aerosols.* Science of The Total Environment, 2016. 551-552: p. 51-56.
23. Liu, D., et al., *Black-carbon absorption enhancement in the atmosphere determined by particle mixing state.* Nature Geoscience, 2017. 10: p. 184.
24. Laskin, A., J. Laskin, and S.A. Nizkorodov, *Chemistry of Atmospheric Brown Carbon.* Chemical Reviews, 2015. 115(10): p. 4335-4382.
25. Jacobson, M.Z., *Isolating nitrated and aromatic aerosols and nitrated aromatic gases as sources of ultraviolet light absorption.* Journal of Geophysical Research: Atmospheres, 1999. 104(D3): p. 3527-3542.
26. Bond, T.C., *Spectral dependence of visible light absorption by carbonaceous particles emitted from coal combustion.* Geophysical Research Letters, 2001. 28(21): p. 4075-4078.
27. Alexander, D.T.L., P.A. Crozier, and J.R. Anderson, *Brown Carbon Spheres in East Asian Outflow and Their Optical Properties.* Science, 2008. 321(5890): p. 833-836.
28. Lack, D.A. and C.D. Cappa, *Impact of brown and clear carbon on light absorption enhancement, single scatter albedo and absorption wavelength dependence of black carbon.* Atmospheric Chemistry and Physics, 2010. 10(9): p. 4207-4220.

29. Saleh, R., et al., *Brownness of organics in aerosols from biomass burning linked to their black carbon content.* Nature Geoscience, 2014. 7: p. 647–650.

30. Brown, H., et al., *Radiative effect and climate impacts of brown carbon with the Community Atmosphere Model (CAM5).* Atmospheric Chemistry and Physics, 2018. 18(24): p. 17745-17768.

31. Frenklach, M. and H. Wang, *Detailed modeling of soot particle nucleation and growth.* Symposium (International) on Combustion, 1991. 23(1): p. 1559-1566.

32. Frenklach, M., *Reaction mechanism of soot formation in flames.* Physical chemistry chemical Physics, 2002. 4(11): p. 2028-2037.

33. Parker, D.S.N., et al., *Hydrogen Abstraction/Acetylene Addition Revealed.* Angewandte Chemie International Edition, 2014. 53(30): p. 7740-7744.

34. Johansson, K.O., et al., *Resonance-stabilized hydrocarbon-radical chain reactions may explain soot inception and growth.* Science, 2018. 361(6406): p. 997.

35. Kholghy, M.R., A. Veshkini, and M.J. Thomson, *The core–shell internal nanostructure of soot – A criterion to model soot maturity.* Carbon, 2016. 100: p. 508-536.

36. Hays, M.D. and R.L. Vander Wal, *Heterogeneous Soot Nanostructure in Atmospheric and Combustion Source Aerosols.* Energy & Fuels, 2007. 21(2): p. 801-811.

37. Alfè, M., et al., *Structure–property relationship in nanostructures of young and mature soot in premixed flames.* Proceedings of the Combustion Institute, 2009. 32(1): p. 697-704.

38. Müller, J.O., et al., *Bulk and surface structural investigations of diesel engine soot and carbon black.* Physical Chemistry Chemical Physics, 2007. 9(30): p. 4018-4025.

39. Gaddam, C.K., et al., *Reconciliation of carbon oxidation rates and activation energies based on changing nanostructure.* Carbon, 2016. 98: p. 545-556.

40. Yehliu, K., et al., *Impact of fuel formulation on the nanostructure and reactivity of diesel soot.* Combustion and Flame, 2012. 159(12): p. 3597-3606.

41. Vander Wal, R.L. and A.J. Tomasek, *Soot oxidation: dependence upon initial nanostructure.* Combustion and Flame, 2003. 134(1): p. 1-9.

42. Minutolo, P., G. Gambi, and A. D'Alessio, *The optical band gap model in the interpretation of the UV-visible absorption spectra of rich premixed flames.* Symposium (International) on Combustion, 1996. 26(1): p. 951-957.

43. Singh, M. and L.R. Vander Wal, *Nanostructure Quantification of Carbon Blacks.* C — Journal of Carbon Research, 2018. 5(1).

44. Li, X., et al., *Oxidative Reactivity of Particles Emitted from a Diesel Engine Operating at Light Load with EGR.* Aerosol Science and Technology, 2015. 49(1): p. 1-10.

45. Tree, D.R. and K.I. Svensson, *Soot processes in compression ignition engines.* Progress in Energy and Combustion Science, 2007. 33(3): p. 272-309.

46. Dec, J.E., *A Conceptual Model of DI Diesel Combustion Based on Laser-Sheet Imaging.* SAE Transactions, 1997. 106: p. 1319-1348.

47. Li, Z., et al., *Evolution of the nanostructure, fractal dimension and size of in-cylinder soot during diesel combustion process.* Combustion and Flame, 2011. 158(8): p. 1624-1630.

48. Vander Wal, R.L., V.M. Bryg, and M.D. Hays, *Fingerprinting soot (towards source identification): Physical structure and chemical composition.* Journal of Aerosol Science, 2010. 41(1): p. 108-117.

49. Kirchstetter, T.W., T. Novakov, and P.V. Hobbs, *Evidence that the spectral dependence of light absorption by aerosols is affected by organic carbon.* Journal of Geophysical Research: Atmospheres, 2004. 109(D21).

50. Bond, T.C. and R.W. Bergstrom, *Light Absorption by Carbonaceous Particles: An Investigative Review.* Aerosol Science and Technology, 2006. 40(1): p. 27-67.

51. Jung, Y. and C. Bae, *Immaturity of soot particles in exhaust gas for low temperature diesel combustion in a direct injection compression ignition engine.* Fuel, 2015. 161: p. 312-322.

52. Savic, N., et al., *Influence of biodiesel fuel composition on the morphology and microstructure of particles emitted from diesel engines.* Carbon, 2016. 104: p. 179-189.

53. Canagaratna, M.R., et al., *Chase Studies of Particulate Emissions from in-use New York City Vehicles.* Aerosol Science and Technology, 2004. 38(6): p. 555-573.

54. Liu, W.-J., et al., *Fates of Chemical Elements in Biomass during Its Pyrolysis.* Chemical Reviews, 2017. 117(9): p. 6367-6398.

55. Wang, J., et al., *Observation of Fullerene Soot in Eastern China.* Environmental Science & Technology Letters, 2016. 3(4): p. 121-126.

56. Simonsson, J., et al., *Wavelength dependence of extinction in sooting flat premixed flames in the visible and near-infrared regimes.* Applied Physics B, 2015. 119(4): p. 657-667.

57. López-Yglesias, X., P.E. Schrader, and H.A. Michelsen, *Soot maturity and absorption cross sections.* Journal of Aerosol Science, 2014. 75: p. 43-64.

58. Robertson, J. and E.P. O'Reilly, *Electronic and atomic structure of amorphous carbon.* Physical Review B, 1987. 35(6): p. 2946-2957.

59. Adkins, E.M. and J.H. Miller, *Extinction measurements for optical band gap determination of soot in a series of nitrogen-diluted ethylene/air non-premixed flames.* Physical Chemistry Chemical Physics, 2015. 17(4): p. 2686-2695.

60. Botero, M.L., et al., *PAH structure analysis of soot in a non-premixed flame using high-resolution transmission electron microscopy and optical band gap analysis.* Combustion and Flame, 2016. 164: p. 250-258.

61. Miller, J.H., et al., *Experimental and computational determinations of optical band gaps for PAH and soot in a N2-diluted, ethylene/air non-premixed flame.* Proceedings of the Combustion Institute, 2013. 34(2): p. 3669-3675.

62. Menon, A., et al., *Optical band gap of cross-linked, curved, and radical polyaromatic hydrocarbons.* Physical Chemistry Chemical Physics, 2019. 21(29): p. 16240-16251.

63. Tauc, J., R. Grigorovici, and A. Vancu, *Optical Properties and Electronic Structure of Amorphous Germanium.* physica status solidi (b), 1966. 15(2): p. 627-637.

64. Pöschl, U., *Aerosol particle analysis: challenges and progress.* Analytical and Bioanalytical Chemistry, 2003. 375(1): p. 30-32.

65. Kennedy, I.M., *The health effects of combustion-generated aerosols.* Proceedings of the Combustion Institute, 2007. 31(2): p. 2757-2770.

66. Vogel, C.F.A., et al., *Induction of Proinflammatory Cytokines and C-Reactive Protein in Human Macrophage Cell Line U937 Exposed to Air Pollution Particulates.* Environmental Health Perspectives, 2005. 113(11): p. 1536-1541.

67. Stoeger, T., et al., *Instillation of Six Different Ultrafine Carbon Particles Indicates a Surface Area Threshold Dose for Acute Lung Inflammation in Mice.* Environmental Health Perspectives, 2006. 114(3): p. 328-333.

68. Schmid, O. and T. Stoeger, *Surface area is the biologically most effective dose metric for acute nanoparticle toxicity in the lung.* Journal of Aerosol Science, 2016. 99: p. 133-143.

69. Jacobsen, N.R., et al., *Lung inflammation and genotoxicity following pulmonary exposure to nanoparticles in ApoE-/- mice.* Particle and Fibre Toxicology, 2009. 6(1): p. 2.

70. Antiñolo, M., et al., *Connecting the oxidation of soot to its redox cycling abilities.* Nature Communications, 2015. 6(1): p. 6812.

71. Jaramillo, I.C., et al., *Effect of nanostructure, oxidative pressure and extent of oxidation on model carbon reactivity.* Combustion and Flame, 2015. 162(5): p. 1848-1856.

72. Johansson, K.O., et al., *Evolution of maturity levels of the particle surface and bulk during soot growth and oxidation in a flame.* Aerosol Science and Technology, 2017. 51(12): p. 1333-1344.

73. Shamun, S., et al., *Detailed Characterization of Particulate Matter in Alcohol Exhaust Emissions.* The proceedings of the international symposium on diagnostics and modeling of combustion in internal combustion engines 2017.9 The Japan Society of Mechanical Engineers., 2017: p. B304.

74. Gallo, Y., et al., *A study of in-cylinder soot oxidation by laser extinction measurements during an EGR-sweep in an optical diesel engine.* SAE Technical Paper, 2015: p. 2015–01–0800.

75. Korhonen, K., et al., *Ice nucleating ability of particulate emissions from solid biomass-fired cookstoves: an experimental study.* Atmospheric Chemistry and Physics Discussions, 2019. 2019: p. 1-32.

76. Onasch, T.B., et al., *Soot Particle Aerosol Mass Spectrometer: Development, Validation, and Initial Application.* Aerosol Science and Technology, 2012. 46(7): p. 804-817.

77. Alfarra, M.R., et al., *Characterization of urban and rural organic particulate in the Lower Fraser Valley using two Aerodyne Aerosol Mass Spectrometers.* Atmospheric Environment, 2004. 38(34): p. 5745-5758.

78. DeCarlo, P.F., et al., *Field-Deployable, High-Resolution, Time-of-Flight Aerosol Mass Spectrometer.* Analytical Chemistry, 2006. 78(24): p. 8281-8289.

79. Drewnick, F., et al., *A New Time-of-Flight Aerosol Mass Spectrometer (TOF-AMS)—Instrument Description and First Field Deployment.* Aerosol Science and Technology, 2005. 39(7): p. 637-658.

80. Jimenez, J.L., et al., *Ambient aerosol sampling using the Aerodyne Aerosol Mass Spectrometer.* Journal of Geophysical Research: Atmospheres, 2003. 108(D7).

81. Herring, C.L., et al., *New Methodology for Quantifying Polycyclic Aromatic Hydrocarbons (PAHs) Using High-Resolution Aerosol Mass Spectrometry.* Aerosol Science and Technology, 2015. 49(11): p. 1131-1148.

82. Onasch, T.B., et al., *Investigations of SP-AMS Carbon Ion Distributions as a Function of Refractory Black Carbon Particle Type.* Aerosol Science and Technology, 2015. 49(6): p. 409-422.

83. Liu, P.S.K., et al., *Transmission Efficiency of an Aerodynamic Focusing Lens System: Comparison of Model Calculations and Laboratory Measurements for the Aerodyne Aerosol Mass Spectrometer.* Aerosol Science and Technology, 2007. 41(8): p. 721-733.

84. Drinovec, L., et al., *The "dual-spot" Aethalometer: an improved measurement of aerosol black carbon with real-time loading compensation.* Atmospheric Measurement Techniques, 2015. 8(5): p. 1965-1979.

85. Weingartner, E., et al., *Absorption of light by soot particles: determination of the absorption coefficient by means of aethalometers.* Journal of Aerosol Science, 2003. 34(10): p. 1445-1463.

86. Wang, X., et al., *Deriving brown carbon from multiwavelength absorption measurements: method and application to AERONET and Aethalometer observations.* Atmospheric Chemistry and Physics, 2016. 16(19): p. 12733-12752.

87. Davis, E.A. and N.F. Mott, *Conduction in non-crystalline systems V. Conductivity, optical absorption and photoconductivity in amorphous semiconductors.* The Philosophical Magazine: A Journal of Theoretical Experimental and Applied Physics, 1970. 22(179): p. 0903-0922.

88. Cavalli, F., et al., *Toward a standardised thermal-optical protocol for measuring atmospheric organic and elemental carbon: the EUSAAR protocol.* Atmospheric Measurement Techniques, 2010. 3(1): p. 79-89.

89. Zhang, Y., et al., *The soot particle formation process inside the piston bowl of a small-bore diesel engine.* Combustion and Flame, 2017. 185: p. 278-291.

90. Zhang, Y., R. Zhang, and S. Kook, *Nanostructure analysis of in-flame soot particles under the influence of jet-jet interactions in a light-duty diesel engine.* SAE International Journal of Engines, 2015. 8(2015-24-2444): p. 2213-2226.

91. Zhang, Y., et al., *The influence of a large methyl ester on in-flame soot particle structures in a small-bore diesel engine.* Fuel, 2017. 194: p. 423-435.

92. Zhang, Y., et al., *A Comparison between In-Flame and Exhaust Soot Nanostructures in a Light-Duty Diesel Engine.* SAE Technical Paper, 2017: p. 2017-01-0710.

93. Sakai, M., et al., *Nanostructure analysis of primary soot particles directly sampled in diesel spray flame via HRTEM.* SAE Technical Paper, 2012: p. 2012-01-1722.

94. Yehliu, K., R.L. Vander Wal, and A.L. Boehman, *Development of an HRTEM image analysis method to quantify carbon nanostructure.* Combustion and Flame, 2011. 158(9): p. 1837-1851.

95. Jacobsen, N.R., et al., *Genotoxicity, cytotoxicity, and reactive oxygen species induced by single-walled carbon nanotubes and C60 fullerenes in the FE1-Muta™Mouse lung epithelial cells.* Environmental and Molecular Mutagenesis, 2008. 49(6): p. 476-487.

96. Høgsberg, T., et al., *Black tattoo inks induce reactive oxygen species production correlating with aggregation of pigment nanoparticles and product brand but not with the polycyclic aromatic hydrocarbon content.* Experimental Dermatology, 2013. 22(7): p. 464-469.

97. Halliwell, B. and M. Whiteman, *Measuring reactive species and oxidative damage in vivo and in cell culture: how should you do it and what do the results mean?* British Journal of Pharmacology, 2004. 142(2): p. 231-255.

98. Bates, J.T., et al., *Review of Acellular Assays of Ambient Particulate Matter Oxidative Potential: Methods and Relationships with Composition, Sources, and Health Effects.* Environmental Science & Technology, 2019. 53(8): p. 4003-4019.

99. Corbin, J., et al., *Mass spectrometry of refractory black carbon particles from six sources: carbon-cluster and oxygenated ions.* Atmospheric Chemistry and Physics, 2014. 14(5): p. 2591-2603.

100. Maricq, M.M., *An examination of soot composition in premixed hydrocarbon flames via laser ablation particle mass spectrometry.* Journal of Aerosol Science, 2009. 40(10): p. 844-857.

101. Maricq, M.M., *Examining the Relationship Between Black Carbon and Soot in Flames and Engine Exhaust.* Aerosol Science and Technology, 2014. 48(6): p. 620-629.

102. Lea-Langton, A., H. Li, and G.E. Andrews, *Comparison of Particulate PAH Emissions for Diesel, Biodiesel and Cooking Oil using a Heavy Duty DI Diesel Engine.* SAE Technical Paper, 2008.

103. Saleh, R., Z. Cheng, and K. Atwi, *The Brown–Black Continuum of Light-Absorbing Combustion Aerosols.* Environmental Science & Technology Letters, 2018. 5(8): p. 508-513.

104. Cheng, Z., et al., *Investigating the dependence of light-absorption properties of combustion carbonaceous aerosols on combustion conditions.* Aerosol Science and Technology, 2019. 53(4): p. 419-434.

105. Ferrari, A.C. and J. Robertson, *Interpretation of Raman spectra of disordered and amorphous carbon.* Physical Review B, 2000. 61(20): p. 14095-14107.

106. Corbin, J.C., et al., *Infrared-absorbing carbonaceous tar can dominate light absorption by marine-engine exhaust.* npj Climate and Atmospheric Science, 2019. 2(1): p. 12.

107. International Agency for Research on Cancer (IARC), *IARC Monographs on the Evaluation of Carcinogenic Risks to Humans: Diesel and Gasoline Engine Exhausts and*

Some Nitroarenes Vol. 105. 2013, Lyon, France: IARC; World Health Organization (WHO).

108. Maynard, A.D. and E.D. Kuempel, *Airborne Nanostructured Particles and Occupational Health.* Journal of Nanoparticle Research, 2005. 7(6): p. 587-614.
109. Figueiredo, J.L., et al., *Modification of the surface chemistry of activated carbons.* Carbon, 1999. 37(9): p. 1379-1389.
110. Biswas, S., et al., *Oxidative Potential of Semi-Volatile and Non Volatile Particulate Matter (PM) from Heavy-Duty Vehicles Retrofitted with Emission Control Technologies.* Environmental Science & Technology, 2009. 43(10): p. 3905-3912.
111. Modrzynska, J., et al., *Primary genotoxicity in the liver following pulmonary exposure to carbon black nanoparticles in mice.* Particle and Fibre Toxicology, 2018. 15(1): p. 2.
112. Bourdon, J.A., et al., *Carbon black nanoparticle instillation induces sustained inflammation and genotoxicity in mouse lung and liver.* Particle and fibre toxicology, 2012. 9: p. 5-5.
113. Aronsson, U., et al., *Analysis of EGR Effects on the Soot Distribution in a Heavy Duty Diesel Engine using Time-Resolved Laser Induced Incandescence.* SAE International Journal of Engines, 2010. 3(2): p. 137-155.
114. Singh, M., et al., *Soot differentiation by laser derivatization.* Aerosol Science and Technology, 2019. 53(2): p. 207-229.
115. OECD International Energy Agency (IEA), *IEA World Energy Balances* www.iea.org 2019.

Printed by Media-Tryck, Lund 2020 NORDIC SWAN ECOLABEL 3041 0903

Ergonomics and Aerosol Technology
Department of Design Sciences
Faculty of Engineering, Lund University

ISSN 1650-9773, Publication 64
ISBN 978-91-7895-380-6